Available online at www.sciencedirect.com

jmr&t Journal of Materials Research and Technology

journal homepage: www.elsevier.com/locate/jmrt

Review Article

Advanced manufacturing of high-speed steels: A critical review of the process design, microstructural evolution, and engineering performance

Yujie Wang [a], Bo Mao [a,*], Shuangjie Chu [b], Sai Chen [a], Hui Xing [a], Haiyan Zhao [a,c], Shuyang Wang [b], Yuqian Wang [f], Jiao Zhang [a,d,e,**], Baode Sun [a,d,e]

[a] School of Materials Science and Engineering, Shanghai Jiao Tong University, Shanghai, 200240, China
[b] Baoshan Iron & Steel Cooperation Limited, Shanghai, 201900, China
[c] Baowu Special Metallurgy Cooperation Limited, Shanghai, 201900, China
[d] State Key Lab of Metal Matrix Composites, Shanghai Jiao Tong University, Shanghai, 200240, China
[e] Collaborative Innovation Center for Advanced Ship and Deep-sea Exploration, Shanghai Jiao Tong University, Shanghai, 200240, China
[f] Department of Mechanical Engineering, University of Nevada-Reno, 89557, United States

ARTICLE INFO

Article history:
Received 15 February 2023
Accepted 30 April 2023
Available online 5 May 2023

Keywords:
High-speed steel
Advanced manufacturing
Theoretical modeling
Microstructural evolution
Mechanical properties

ABSTRACT

High-speed steels (HSSs) are frequently utilized as cutting tools and wear-resistant components for a variety of applications because of their exceptional hot hardness and desirable wear resistance. Over the last few decades, numerous strategies for the manufacture of HSS components have been developed. Among these methods, advanced manufacturing (AM) techniques, including powder bed fusion (PBF), direct energy deposition (DED), and material jetting (MJ), have gained great scientific attention because they allow the fabrication of complicated mechanical components with high customization and specialized qualities. However, a comprehensive review of the recent progress of AM of HSSs is still lacking and this paper aims to address this need. This present paper reviews all the significant attributes of the state-of-the-art AM techniques for the fabrication of HSSs. The process designs of AM by means of PBF, DED, and MJ are discussed and compared. Process modeling work, including the microstructure prediction and solidification behavior of AM-fabricated HSS is reviewed. The microstructural evolutions during AM processes in terms of carbide precipitation dynamics, grain growth behavior and defect formation

* Corresponding author.
** Corresponding author.
E-mail addresses: bmao@sjtu.edu.cn (B. Mao), zj119@sjtu.edu.cn (J. Zhang).
https://doi.org/10.1016/j.jmrt.2023.04.269

mechanism of HSSs are discussed. Moreover, the engineering properties of the AMed HSS are summarized, including residual stress, hardness, strength, impact toughness and enhanced wear resistance. Furthermore, the existing difficulties of AM technology and the future research objectives for producing HSS components are offered and explored.

Nomenclature

Symbol	*Description*
r_m	the radius of the molten pool
r_p	the radius of powder flow
r_b	the distance from the beam centerline
l	the laser/powder working distance
N_{max}	the maximum volume concentration
$A(T)$	coefficient of surface coupling for the laser
ε_0	the permissiveness of empty space
ω	the angle of laser radiation's frequency
$\rho_e(T)$	temperature-dependent resistivity
P_l	laser power
v_s	scanning speed
Δy_s	hatch distance
D_s	layer thickness
P	total power of the heat source
f	distribution factor
r_h	the radius of the heat source
r	radial distance
h_c	convective coefficient
ε	radiation emissivity
σ	Stefan-Boltzmann constant
T_∞	ambient temperature
ρ_l	the density of the molten fluid
L_v	latent heat of evaporation
V_{dv}	boundary movement speed
$g(d)$	the mass probability density function
d	particle diameter
d_m	the median particle diameter
σ_g	standard deviation
D	melt delivery nozzle diameter
γ_m	melt surface tension
ξ	the metal-to-gas kinematic viscosity ratio
$\dot{M}$	flow rate
ρ_g	gas density
v_{gi}	initial gas velocity
A	atomizer exit orifice cross-sectional area
K_a	experimental constant
ρ_m	melt density
C_1	experimental constant
C_2	experimental constant
C_3	experimental constant
$\dot{m}$	mass flux
C_M	correlation coefficient
γ	specific heat ratio of atomized gas
P_0	stagnation pressure
P_e	exit gas pressure
f_s	solid fraction
z	axial distance
T_0	stagnation temperature
T_e	the gas temperature at the nozzle exit
P_1	initial conditions of pressure
P_2	final conditions of pressure
g	acceleration
n	molar heat capacity ratio
v_g	gas velocity at the nozzle exit
ρ_d	droplet density
C_D	droplet drag coefficient
v_d	droplet velocity
v_g	gas velocity
Re	Reynolds number
L	latent heat
p	porosity
Φ	porosity coefficient
$\overline{f_s}$	average solid fraction
Γ	particle packing density
β	solidification contraction
SE	sticking efficiency
η_s	solid sticking coefficients
η_L	liquid sticking coefficients
f_L	liquid fraction
ε_∞	vary from 0 to 1
ρ	density
C	specific heat capacity
V	volume
T	temperature
k	thermal conductivity
ΔT_{hom}	homogeneous undercooling
γ	solid/liquid interface energy
Ω	atomic volume
k_B	Boltzmann's constant
h_f	latent heat of fusion
ΔT_{het}	Heterogeneous undercooling
$\dot{T}$	the function of the droplet size
$f(\theta)$	contact angle factor
N_v	number of liquid atoms per unit volume
V_{cr}	critical solidification front velocity

1. Introduction

High-speed steels (HSSs) belong to a special category of tool steels that are currently used for a variety of applications in the industry. Their microstructure is typically characterized by the appreciable amounts of carbides (up to 50 vol.-%) distributed in the tempered martensite matrix [1]. This microstructural feature endows HSS with exceptional surface hardness, wear resistance, and fatigue crack resistance at both room and elevated temperatures [2]. Therefore, HSSs have been widely utilized as wear-resistance parts, such as cutting tools, milling rolls, and bearings, as shown in Fig. 1(a) [3–5]. Meanwhile, searching the Web of Science in steel publications, the proportion of the number of papers and patents on HSSs in all the steels related publications continues to increase from 9.1% in 2014 to 11.9% in 2020 (Fig. 1(b)). The global HSSs production capacity grows from approximately 37.7×10^4 tons in 2014 to approximately 46.8×10^4 tons in 2020, as summarized in Fig. 1(c), indicating a growing research interest and market demand for HSSs in both academia and industry.

The conventional manufacturing processes for fabricating HSSs include conventional casting (CC) [6–8], electroslag remelting (ESR) [9–12] and powder metallurgy (PM) [13–16]. During the CC process, the segregation of large quantities of carbon and alloying elements before crystallization results in an intergranular coarse carbide network due to the slow solidification rate [17]. Therefore, post-forging or rolling processes must be employed to fragmentize the carbide network, resulting in a low final yield [18,19]. ESR process has a relatively faster cooling rate while large amounts of ledeburite structure together with carbide networks are still formed, resulting in poor engineering performances [20,21]. PM process has shown extraordinary advantages for fabricating HSSs with dispersed and fine primary carbides and superior mechanical properties. However, this approach is limited by its high cost and low yield rate because of the complicated heat treatment procedures and precise equipment requirements [13,22].

With the advent of advanced manufacturing (AM), it is now possible to fabricate mechanical components with complicated geometry, great customizability, and specific qualities without being constrained by traditional manufacturing techniques [23]. State-of-the-art AM techniques, such as powder bed fusion (PBF), direct energy deposition (DED), and material jetting (MJ), have been extensively researched as a remarkable paradigm for the fabrication of products that are used in a wide variety of automotive, defense and aerospace applications [24]. For HSSs, AM can also provide an efficient alternative to repair the damaged tools whereby a damaged surface can be cladded with a printed layer. At present, AM methods are being effectively applied in the industry to create high-performance HSS products [25–27]. Moreover, the rapid advancement of AM methods has substantially widened the production route and alloy design spectrum of a variety of grades of HSSs, both of which have been positively impacted.

Extensive research efforts have been paid to the investigation of AM processes of HSS in recent years. For instance, Saewe et al. [28–30] looked into the viability of producing M50 and HS6-5-3-8 HSSs using the selective laser melting (SLM) procedure. It was shown that by using the right process parameters, dense, crack-free HSS components with a high hardness could be produced. Further research was done on

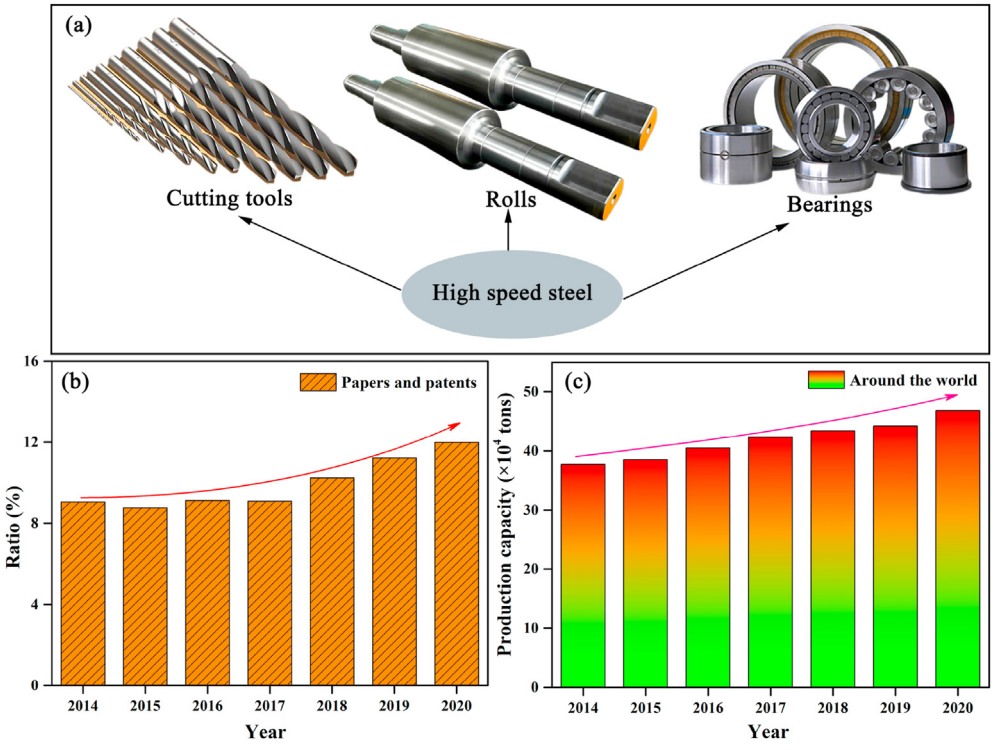

Fig. 1 – (a) Typical applications of HSS. (b) Proportions of papers and patents in the field of HSSs in the steel research community and (c) production output of HSS in the global market from 2014 to 2020.

the impact of carbon content on the processability of HS6-5-3-8 HSS produced using the SLM process [31]. It was discovered that an increase in the carbon content of the alloy results in a totally austenitic matrix as well as an increase in the volume percentage of the carbides. On the other hand, in contrast to the good effect that was expected austenite stabilization would have on the development of cracks, it was shown that cracking became worse as carbon content increased. Jin et al. [32] characterized the solidification microstructure and carbide precipitation behavior of S390 HSS treated by electron beam melting (EBM) with high carbon and alloying element content. By varying the laser scanning speed, Rahman et al. [33] conducted laser metal deposition (LMD) of vanadium-rich HSS to investigate the impact of a rapid cooling rate on the distribution and morphology of carbides. It was discovered that increasing the speed of the laser processing might result in an improvement in the microhardness of vanadium-rich HSS. Similar research results were observed in M2 HSS deposited by laser cladding (LC) by Arias et al. [34,35]. Especially, multilayer LC of accessible M4 and Fe–1.4C–5W–4Mo–3V–4Cr (wt pct) HSSs was studied by Shim et al. [36] and Rahman et al. [37], respectively. These HSSs had varying thicknesses, ranging from moderately thin to quite thick. In addition, the M_2C carbide decomposition and distribution of high cobalt HSS manufactured by SF were studied by Lee et al. [38,39]. It was discovered that a shift in the temperature conditions was responsible for the development of new carbide morphologies as well as their distribution during the SF process. Lu et al. [40] successfully fabricated niobium-added M3:2 HSS by SF, and they found that Nb enhanced the thermal stability of M_2C carbides.

Fayazfar et al. [41], Bajaj et al. [42], Haghdadi et al. [43], and Yin et al. [44] have published some of the most thorough reviews on AM of steels to date. Fayazfar et al. [41] evaluated PBF-based AM steel processes and the impact of crucial process variables on microstructural development and mechanical behavior (hardness, tensile and cyclic/fatigue characteristics). Bajaj et al. [42] summarized the microstructural evolution of different series of AM-produced steels and elucidated the relationship between the microstructure and performance of these steels. Haghdadi et al. [43] mainly investigated the mechanical, corrosion, and wear properties of steel, and briefly discussed the microstructural evolution of AM-fabricated steel to explain the difference in properties. With an emphasis on understanding the connection between processes, microstructure, and mechanical characteristics, Yin et al. [44] gave an overview of AM processes of austenitic, ferritic, and martensitic steels. However, these review efforts

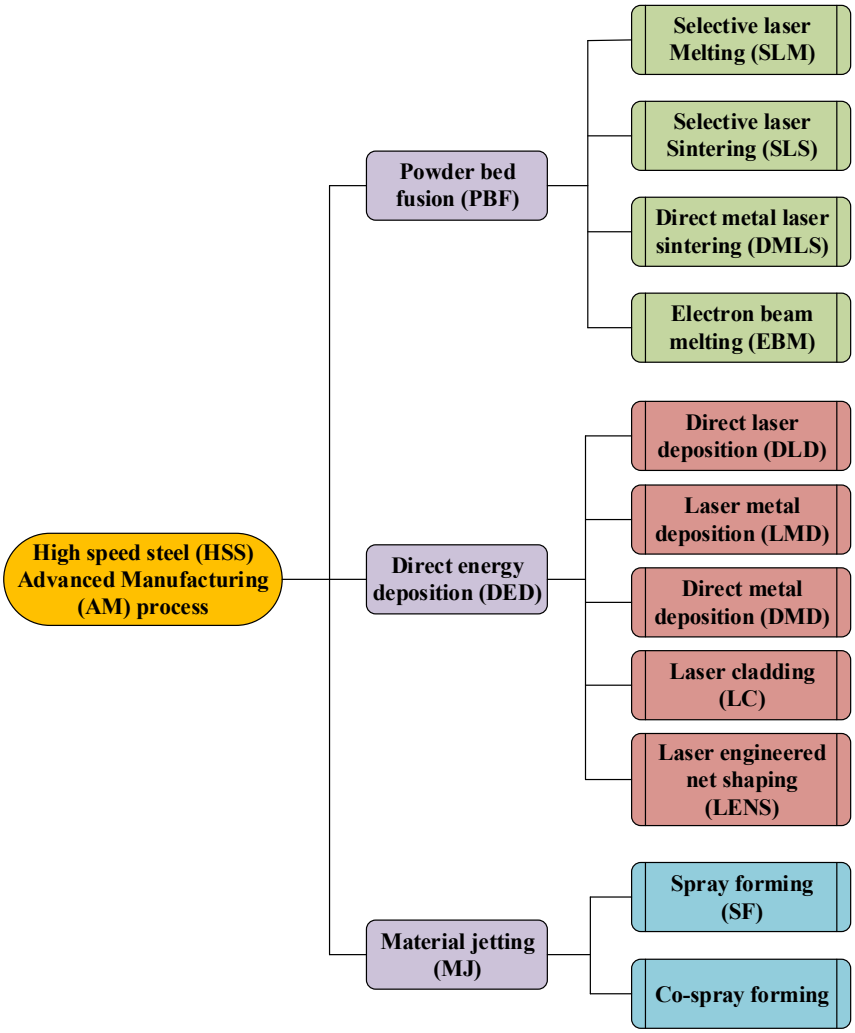

Fig. 2 – Summary of typical AM approaches for fabricating HSS.

emphasized the microstructure and engineering performance of stainless and martensitic steels produced by AM processes, but a complete review of the different aspects of the AM of HSSs is still lacking. Given the rapid development of the research and practice on AM of HSS, we feel that a critical review on summarizing the recent developments will be very timely and significant in this context.

The goal of the work that is being presented here is to provide a thorough analysis of the most recent developments in AM methods for the fabrication of HSS components. The process designs of AM techniques by means of PBF, DED, and MJ are reviewed and compared. The numerical modeling and analysis of different AM processes are summarized. Meanwhile, the influences of AM process variables on the microstructure of HSS components are discussed. The mechanical properties and tribological behavior in terms of hardness, strength, impact toughness, as well as wear resistance of HSS components fabricated by AM processes are discussed. Furthermore, a proposal is made about the existing problems and potential future research paths of AM technology for the fabrication of HSS components.

2. Process design

There are seven categories of AM processes according to the ISO/ASTM 52900 standard, and extensive descriptions of many AM techniques are available in the literature [45,46]. Generally, each AM process is featured to manufacture a specific category of material due to the specific bonding and deposition methods. Among all the commercially available AM processes, HSS parts have been successfully fabricated through PBF, DED and MJ. The detailed classification of the aforementioned AM derivative processes for manufacturing HSS parts is shown in Fig. 2. Particularly, since the SF and Co-spray forming (Co-SF) processes have attracted extensive attention in the manufacturing of HSS, they were identified as materials jetting approaches in this paper to strictly abide by the ISO/ASTM 52900 standard terminology [47]. In this chapter, the research progress of process design of PBF, DED and MJ processes for fabricating HSS is reviewed and discussed.

2.1. *Powder bed fusion-based AM*

Layer-to-layer metallurgical bonding in PBF systems must be accomplished via a laser beam or electron beam in order to get around the metals' relatively high enthalpies of fusion and melting points [48]. It is subdivided into SLM, SLS, DMLS, and EBM according to the way of energy and materials delivery. Fig. 3 depicts a schematic diagram of the PBF-based AM process using a laser beam as an energy source. A homogeneous powder bed is initially applied during this procedure, and then a laser beam is utilized to melt certain areas of the bed in order to create the component in a single layer. Following the completion of the first layer, the height of the powder bed is decreased, a fresh layer is rolled into place, and the procedure is repeated. Excess metal powder is produced as a consequence of this repetitive operation, and it is used to support the item while it is being built. Typically, an enclosed inert gas environment is used during the PBF-laser process to limit the rate of oxidation of the components during the construction stage.

2.1.1. *Selective laser melting*

A high-energy laser beam is used to travel over the powder bed at a high velocity based on a specified shape and melt specific spots to produce the cross-section of the component. This is the most versatile PBF-based AM process. Then, until the finalized result is achieved, another layer of loose powder is continually added to the powder bed and melted [49].

Due to the high flexibility and accessibility of SLM, extensive research efforts have been made on the fabrication of HSS. For instance, Saewe et al. [28–30] conducted a feasibility study on the fabrication of HS6-5-3-8 and M50 HSSs using SLM. The findings showed that, if the right processing parameters were used, crack-free HSS components (as constructed) could be manufactured using the SLM technique. The same research conclusion was obtained in the M3:2 HSS fabricated by Geenen et al. [26] using the SLM process. Consequently, to further explore the connection between process parameters and microstructure evolution, the processability and microstructural homogeneity of HS6-5-3-8 HSS manufactured by the SLM process was investigated, as shown in Fig. 4 [31]. Especially, Fig. 4(a) depicts a schematic depiction of the SLM system. As was indicated earlier, the surface of the pre-spread powder is melted selectively by the focused laser beam as part of the SLM process. As a result, a bed forms, with the molten pool serving as the smallest melting unit. As soon as the first layer has been melted and cooled, the construction platform will begin to gently lower itself. After that, the powder bed is covered with a fresh layer of powder, and the procedure is repeated as many times as necessary until the HS6-5-3-8 HSS component is constructed. Scanning electron microscope (SEM) examination of the solidified structure of HS6-5-3-8 HSS along the building direction is displayed in Fig. 4(b). It has been noted that when the temperature gradient increases, the direction of grain development shifts from the molten pool's edge to its center. It is evident that the

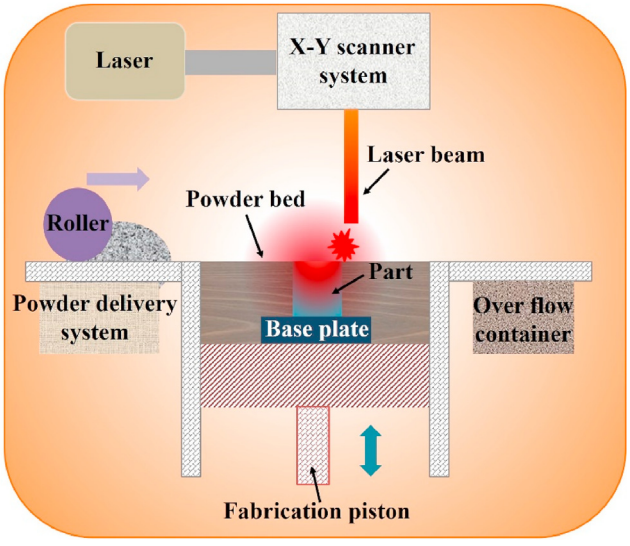

Fig. 3 – A schematic illustration of the PBF-based AM process.

interdendritic zone and molten pool boundaries are where columnar dendrites and equiaxed precipitates are distributed. There is a possibility that the regional decrease in temperature gradient is responsible for the equiaxed solidification structure in the central region of the molten pool. The close-up views are displayed in Fig. 4(c and d), respectively. It demonstrates how extremely tiny dendrites and interdendritic regions make up the sub-grain structure. Meanwhile, to further study the microstructural characteristics of SLM-processed HS6-5-3-8 HSS, the multiphase microstructure can be identified in Fig. 4(e) through electron backscatter diffraction (EBSD). It is plain to observe that the phases are quite finely dispersed and, in some regions, have a structure that is vaguely wave-like. The wave-shaped pattern may suggest a bainite structure and may be generated when austenite grains undergo phase change into ferrite plates. This process can occur in the prior austenite grains [31]. The corresponding inverse pole figure (IPF) maps in the build direction and the normal direction of the cross-section are presented, respectively, as shown in Fig. 4(f and g). It is discovered that the prior austenite grains have a preferential orientation in the <001> direction parallel to the build direction. This preference orientation, which is typically seen in HSSs that are produced via PBF, may be traced back to the favored crystallographic development along the largest temperature gradient as the root reason.

2.1.2. *Selective laser sintering*

SLS is one of the most sophisticated rapid prototyping methods, which uses a laser to scan over a bed of loosely packed powder to sinter the powder into the desired form. The SLS process can be described in detail: the powder layer is distributed on the substrate, and the laser beam scans the powder layer to melt the powder at the desired location. The entire component is built layer by layer from bottom to top. When comparing SLS with SLM, the most notable distinction between the two processes is that the former fuses powders via the process of partial melting, whilst the latter proceeds through the process of complete melting [50].

According to the findings of the research, SLS of M3:2 HSS powders of varying particle sizes had a propensity to form surfaces with low surface density, characterized by large aggregates and inter-aggregate holes [51,52]. However, the gas-atomized M2 HSS powder produced by SLS has developed a uniform microstructure with a very dense surface [51,53]. Dewidar et al. [54] investigated the SLS of Fe–1.39C–14.1 Mo–3.6Cr (wt pct) HSS powders. It was believed that after bronze infiltration, near-net-shape parts with sufficient mechanical properties can be produced for load-bearing applications. The schematic view of the SLS equipment is shown in Fig. 5(a), and the basic principle of manufacturing the target HSS components is described above. The amount of the bronze infiltration and the porosity prior to infiltration are

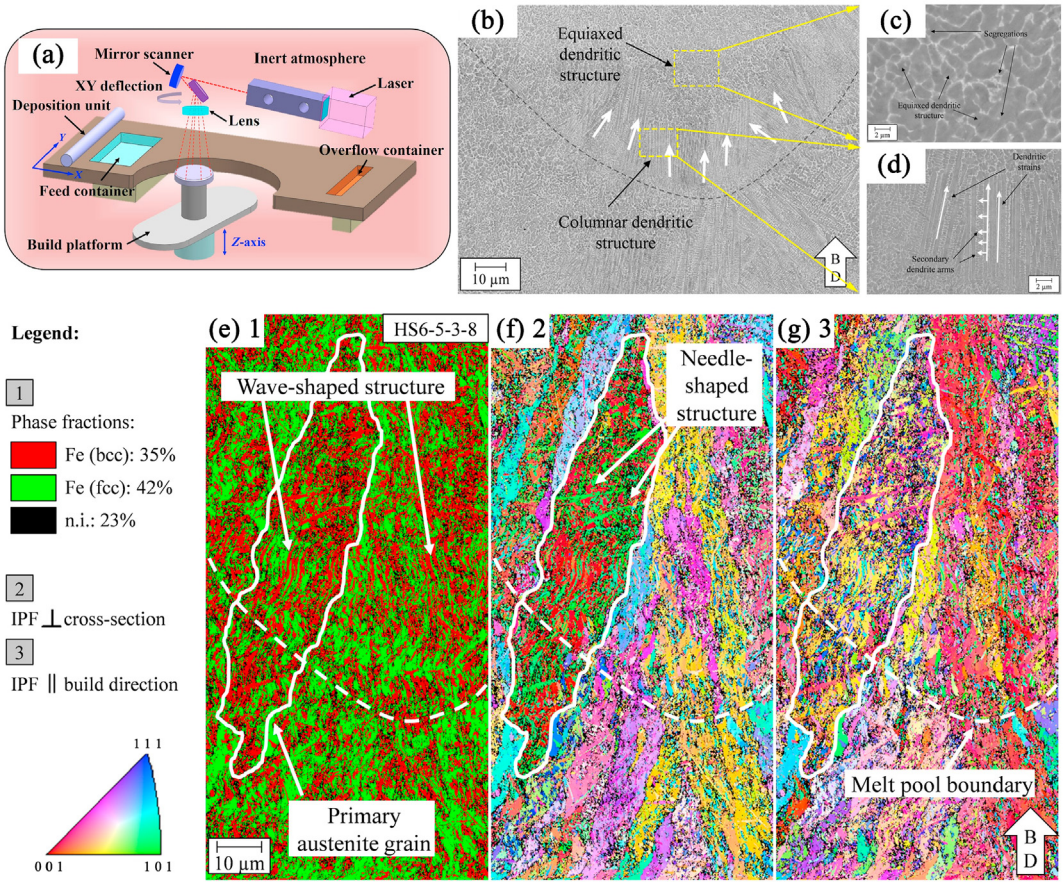

Fig. 4 – (a) Schematic illustration of SLM apparatus. (b) SEM micrograph of the melting pool of HS6-5-3-8 HSS fabricated by SLM. (c) Equiaxed dendritic solidification structure and (d) columnar dendrites in the melting pool in (b). (e) Phase map, (f) and (g) IPF maps of the microstructure of the as-fabricated HS6-5-3-8 HSS [31].

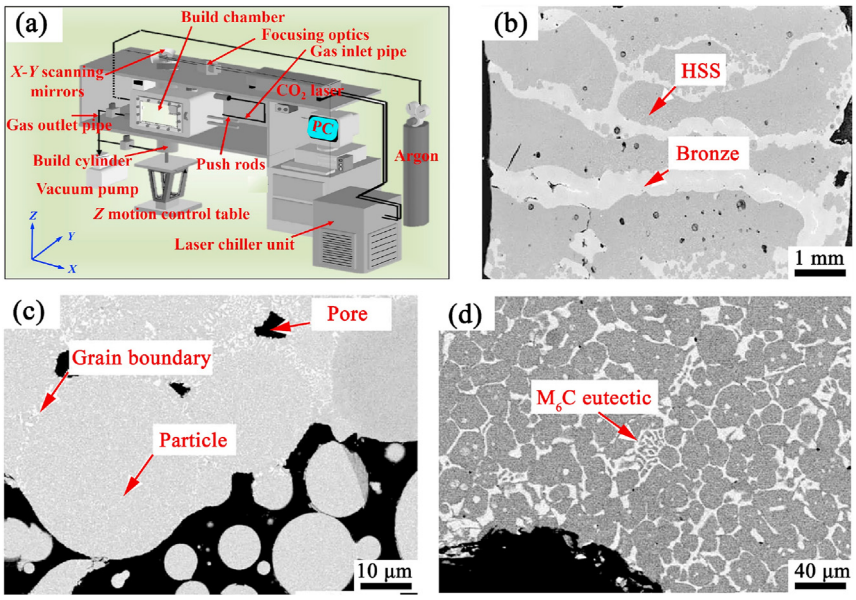

Fig. 5 – (a) Schematic diagram of SLS configuration and (b) microstructure of bronze-infiltrated multilayer Fe–1.39C–14.1Mo–3.6Cr HSS parts. SEM images of the (c) first and (d) final layers of un-infiltrated HSS components [54].

shown in Fig. 5(b), which is a panoramic view of the cross-section of the multilayer portion that has been infiltrated with bronze. Correspondingly, the microstructures of the first and final layers of the un-infiltrated multilayer HSS component are displayed in Fig. 5(c and d). It can be seen that M_6C eutectic carbides are formed during processing. The production of these carbides is evidence that the HSS processing may have exceeded the temperature at which it should have sintered. Especially, Dewidar et al. claimed that M_6C carbides were formed in Fe–1.39C–14.1Mo–3.6Cr (wt pct) HSS, which may be a wrong analysis. Mo forms M_2C-type carbides rather than M_6C-type carbides. M_6C is formed if tungsten is present. Therefore, the results of this research have proved that it is achievable to generate HSS parts using an infiltration process. The modulus of the tested part is 92 GPa and the flexural strength is 460 MPa. Obviously, the mechanical characteristics are more similar to those of aluminum alloys than HSSs.

2.1.3. *Direct metal laser sintering*

The DMLS technique involves the use of a focused laser beam that scans the surface of a loose powder bed. This sinters the powder into complex pieces that cannot be manufactured using traditional manufacturing procedures that are dependent on CAD data. DMLS and SLS are similar in nature. The former is principally used for processing non-metallic powders, while the latter generally processes metal alloy parts. A recent publication provided a summary of the fatigue, tensile strength, and hardness examinations of metallic parts manufactured using the DMLS technique [55]. However, there have only been a relatively small number of publications that report on the

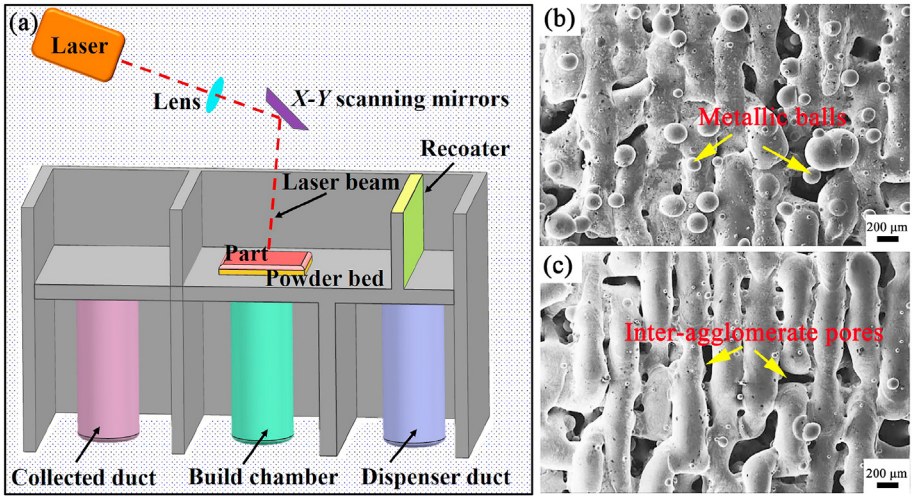

Fig. 6 – (a) Schematic diagram of DMLS equipment. SEM micrographs of HSS fabricated by DMLS: (b) M2 steel and (c) M2 steel with 0.4 wt% graphite [58].

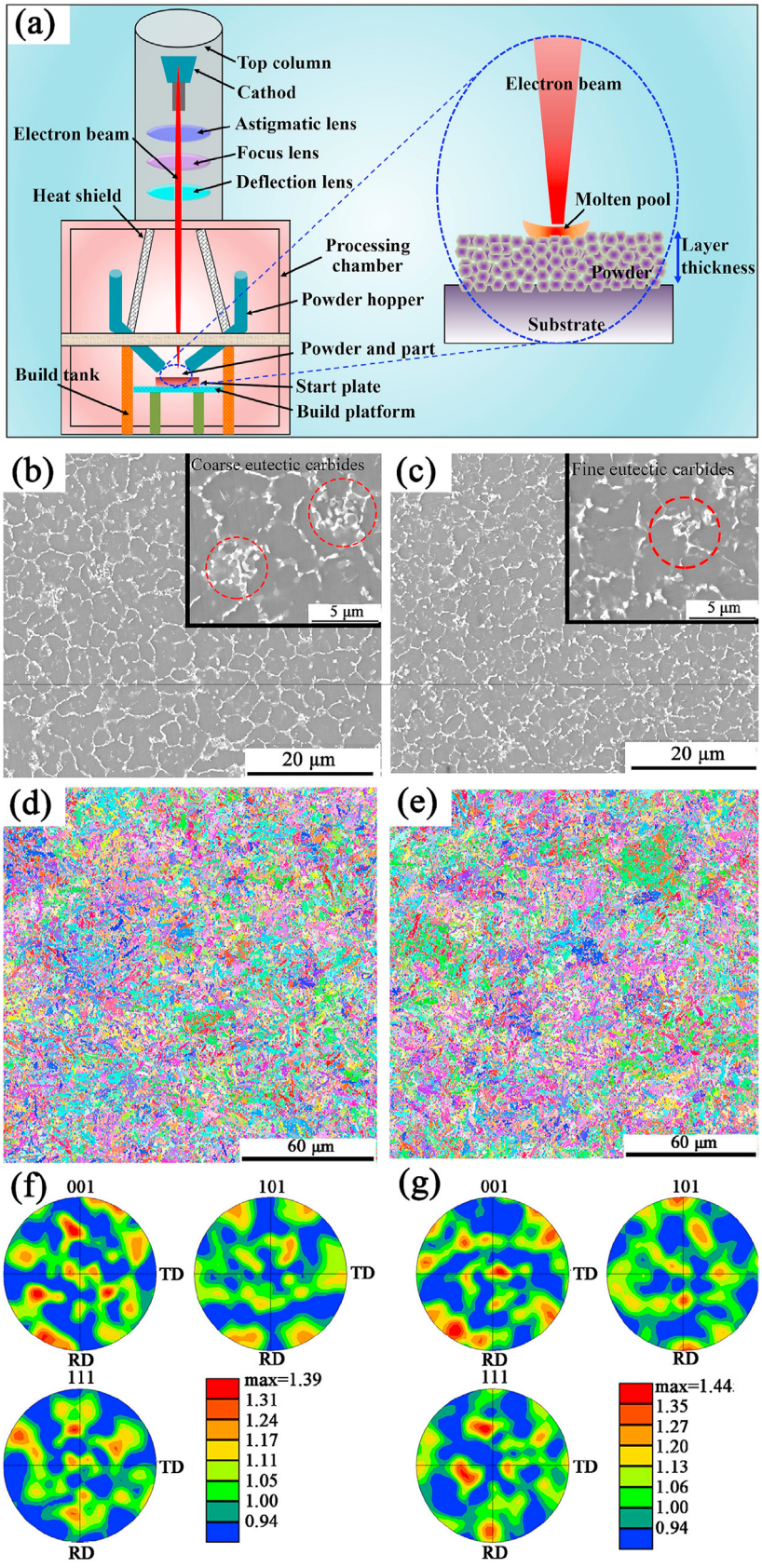

Fig. 7 – (a) Schematic diagram of the EBM system. SEM micrographs of primary carbide distribution of as-EBM S390 HSS at different scanning speeds: (b) $v = 1400$ mm/s, (c) $v = 470$ mm/s. EBSD analysis for (d) S390 HSS fabricated by EBM with a scanning velocity of 1400 mm/s and (e) 470 mm/s (f) and (g) are corresponding pole figures with respect to the IPF in (d) and (e) [32].

manufacture of HSS parts by DMLS. The published documents claimed that HSS powder was not suitable for this process due to the extremely low attainable density (67% of theoretical value) [56]. Nevertheless, Simchi et al. [57] believed that DMLS for manufacturing HSS was difficult but feasible. It was established that the chemical composition and sintering circumstances had a significant impact on the sinterability of HSS as long as the appropriate process parameters were employed.

In this section, therefore, based on the limited available literature, the effects of the sintering atmosphere and carbon content on the quality and microstructure of DMLS M2 HSS components were discussed, as shown in Fig. 6 [58]. Using DMLS, it was discovered that the microstructure of M2 HSS comprises small carbide networks without large primary carbides. The laser scanning speed and sintering atmosphere were predicted to have a significant impact on the densification of the M2 HSS. However, it was discovered that decreasing the laser scan rate ($v < 100$ mm/s) had minimal influence on the densification of the HSS components. Meanwhile, it was found that sintering in an argon environment could obtain a lower porosity. This might be because the laser sintering process causes nitrogen to dissolve into the liquid iron. The schematic diagram of DMLS equipment is displayed in Fig. 6(a). It is emphasized that the basic principle is as mentioned earlier, and the solidification mechanism is the same as that of SLM. The microstructure of M2 HSS parts fabricated by DMLS consists of elongated pores and heterogeneous metal matrix, as seen in Fig. 6(b). It is concluded that the formed inter-agglomerate pores and metal balls are affected by shrinkage and surface tension. Moreover, as displayed in Fig. 6(c), the addition of 0.4 wt% graphite considerably suppresses the formation of metal balls, which may be connected to the increase in sintering kinetics and the reduction in solidus and liquidus temperatures generated by the graphite addition. Dissolved carbon, on the other hand, drastically alters the molten steel's surface tension and viscosity.

2.1.4. *Electron beam melting*

Metal components with complicated geometries may be made using EBM, which melts the metal powder in a vacuum using a high-power electron beam. The basic procedure can be described as preheating the deposited layer before melting. After melting, the starting plate is lowered and fresh powder is supplied from the powder hopper before raking. The procedure is carried out repeatedly up to the point when the component is finished. The electron beam is able to quickly change its position ($\leq$8000 m/s), allowing the powder to be melted at multiple points simultaneously [59]. In contrast to the SLM process, the moving laser beam melts the powder point by point at a lower rate ($\leq$10 m/s) [59].

Only a few publications about EBM of HSSs are available up to now. Ivanov et al. [60] studied the microstructure and phase transformation of HSS S6-5-2 manufactured by EBM. It has been established that as beam energy density increases, the size and quantity of M_6C carbides decrease progressively, followed by the development of martensite and a rise in retained austenite content. Jin et al. [32] characterized the solidification microstructure of S390 HSS processed by EBM. In particular, the architecture of the EBM machine is shown in Fig. 7(a). Fig. 7(b and c) show the typical microstructure of S390 HSS processed by EBM at different scanning speeds. As-EBM microstructures show a distribution of columnar and almost equiaxed grain morphologies, and the discontinuous network of extremely fine primary carbides and retained austenite are spread in the martensite. It can be seen that the close-up views in Fig. 7(b and c) show that S390 HSS fabricated with a higher scanning speed (1400 mm/s) has a larger eutectic carbide area than S390 HSS fabricated with a low scanning speed (470 mm/s). EBSD patterns are provided in Fig. 7(d and e) to demonstrate if various EBM settings result in any preferable textures. The corresponding pole figures are shown in Fig. 7(f and g). As indicated by the relatively low intensity of the pole figure, it can be seen that the EBM S390 HSS specimens with different EBM parameters did not exhibit a strong texture.

In conclusion, it can be found that the microstructure characteristics of HSS parts fabricated by PBF are highly susceptible to process parameters. For this reason, the processing windows of the different PBFs required for the production of HSS are summarized in Table 1.

2.2. *Direct energy deposition-based AM*

Direct energy deposition (DED) is a viable AM process for the manufacture of metallic, functional components [67,68]. The schematic diagram is displayed in Fig. 8. The basic idea is that a powerful laser beam is employed to provide thermal energy during the laser-based DED process. A dynamic molten pool is created when the metal powder that is injected by one or more nozzles melts concurrently with a particular substrate. Afterwards, the increased performance layer is deposited and solidified while the component is constructed layer by layer [46,69]. The DED process is recognized as existing various aliases in available reports, such as laser cladding (LC), direct metal deposition (DMD), direct laser deposition (DLD), and laser metal deposition (LMD) together with laser engineered net shaping (LENS) [70].

DED combines material/energy supply for simultaneous deposition and component formation within a comparable area as opposed to the PBF-based AM technique. Meanwhile, DED offers the advantage of fabricating larger items because of the high deposition rate and large process variable window [71,72]. Additionally, the notable distinctions between PBF and DED may be used to benefit a variety of applications and end-user requirements. For instance, a de-powdering process is necessary, although PBF may provide final components with finer surface quality. DED may be quite effective, although PBF-Laser components' surfaces could be of higher quality [46]. More importantly, because of the combination of material/energy delivery mechanisms, the DED process is easily applicable for fabricating functional graded/composite components with changing material/alloy concentrations. Regardless of PBF or DED, it is necessary to emphasize that grain size and morphology are strongly dependent on thermal history, which directly affects the mechanical and fatigue properties of materials [73]. Large thermal gradients, cyclic heating, and cooling lead to residual stress and anisotropy, which also deteriorate the component's strength and fatigue life.

A series of investigations have been carried out on the microstructural evolution and mechanical characteristics of various grades of HSS. For instance, LMD of vanadium-rich

Table 1 – Processing windows of various HSSs for the PBF process.

Grade	Laser power(W)	Scan speed (mm/s)	Volume energy density (J/mm^3)	Hatch distance (μm)	Layer thickness (μm)	Preheating temperature (°C)	Process	Scan spacing (mm)	Refs
HS6-5-3-8	200	740	90	100	30	350	SLM		[31]
M50	260	1200	/	80	30	500			[61]
M2	130	350–700	87–124	80–120	30	500			[30]
HS6-5-3-8	130/260	670	70/100	80–100	30	200–600			[29]
M50	130/260	400–1800	60–100	60–120	30	500			[28]
M2	100	700	/	/	30	180			[62]
M2	600	350	/	900	/	200			[63]
M2	90–105	100–850	/	/	/	180			[64]
M2	105	250–550	/	128	30	200			[65]
M3:2	100	318	/	20–40	30	200/300			[26]
M2/M3:2	2.5–150	1–20	/	/	/	/	SLS	0.15–0.75	[51–53,66]
HSS	10–150	1–60	/	/	0.4–0.8	/		0.17–0.83	[54]
M2	200	50–175	/	/	0.1	/	DMLS	0.3	[57,58]
	Operate voltage (kV)	Scan speed (mm/s)	Area energy (J/mm2)	Beam current (mA)	Line offset (mm)				
S390	60	470/1400	4.7	5.5	0.05/0.15		EBM		[32]
S6-5-2	15/20	/	3–18	/	/				[60]

HSS [33], T15 HSS [74], DMD of M2 HSS [75], and LC of M2 HSS [34,35,76]. Rahman et al. [27] systematically investigated the microstructural characteristics and mechanical behavior of two high-carbon HSSs fabricated by DED. During the deposition and solidification processes, extra shielding gas nozzles and powder injection nozzles are utilized to protect the molten pool to avoid excessive oxidation of high-carbon HSS. Fig. 9(a) displays the injection and shielding techniques for the DED device. The deposited multilayers of two high-carbon HSSs are displayed in Fig. 9(b and c), respectively. The maximum deposition thickness is about 5 mm in Fig. 9(b). Correspondingly, the SEM micrographs of the two high-carbon HSS specimens are shown in Fig. 9(d and e). It is clear that the microstructure is made up of martensite, retained austenite, and carbide networks. The various morphologies of carbides are presented in detail: blocky, round, rod-like, lamellar and layered shape, as shown in Fig. 9(f–j). To better distinguish the different forms of carbides, phase maps of the two high-carbon HSS samples are presented in Fig. 9(k and l). It is proven that different phases are distributed differently; VC and Mo_2C carbides are mostly found near grain boundaries, while Cr-rich carbides are incorporated into the matrix. Meanwhile, it can be found that the distribution of Mo_2C carbides in high carbon HSS with tungsten element is more than that in high carbon HSS without tungsten element due to the difference in the alloy composition. Variable process parameters, on the other hand, have a considerable impact on the formability of DED-fabricated HSS components. Therefore, Table 2 summarizes the available processing windows for fabricating various grades of HSS parts.

2.3. *Material jetting-based AM*

2.3.1. *Spray forming*

The SF process was first proposed by Professor Singer of Swansea University in 1968 and patented in 1972 [89]. The SF process is schematically depicted in Fig. 10(a), where metal alloys are first melted in an induction furnace before being atomized into small droplets by a high-pressure inert gas. Heat is exchanged between these droplets and the previously deposited layers. During this process, the cold droplets quickly reheat into the mushy state, which promotes the fragmentation of the dendritic arms, and then continuously propel and cool by the high-pressure air flow toward the billet, as depicted in Fig. 10(b). Finally, the dense preforms are collected in multiple layers through the deposition and solidification of droplets. The solidified microstructure can be observed to consist of equiaxed grains, a discontinuous network of lamellar M_2C carbides and MC carbides at grain boundaries and inside the matrix, as seen in Fig. 10(c). It was stated that the rapid cooling rate of atomization was the fundamental factor in the refining of primary carbides in SF-manufactured HSS with M_2C and MC carbides of very small dimensions [17]. Nevertheless, to further increase the degree of densification of the billet, thermomechanical deformation processes are often utilized to obtain a more uniform microstructure. Compared with PBF and DED-based AM processes, HSS fabricated by SF and discovered that the microstructure of the deposited billet was fine equiaxed grains [90], which is the most significant feature of the SF process.

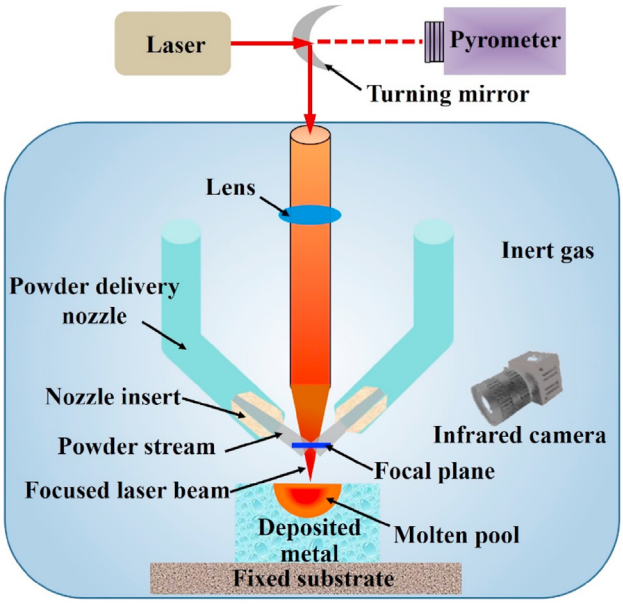

Fig. 8 – Schematic diagram of the DED process.

Compared with ESR and PM, the SF process has shown several advantages in terms of mechanical properties, scalability, process design, efficiency and cost [91–95]. The SF process possesses a higher cooling rate (up to 10^6 K/s) than ESR and PM, resulting in a finer microstructure (as-spray 10–100 μm), higher toughness, and better hot workability of HSS than ESR. Moreover, the manufacturing procedure for the SF process is much less than ESR and PM processes, which is evident by the 5 steps in the SF process, 7 steps in the ESR process, and 12 steps in the PM process, respectively. As a result, the production efficiency of SF is much higher than ESR [96]. More importantly, compared with the PM process, the cost is reduced by 40% [97]. Because of its outstanding near-net-shape ability and great flexibility, SF-made HSS with a fine microstructure has garnered considerable interest from industry and academia, for the reasons described above [98–101]. Similarly, the process parameter variables of the HSS components deposited by SF are shown in Table 3.

2.3.2. *Co-spray forming*

Twin atomizers are used to spray HSS melt concurrently to optimize production efficiency. Therefore, a Co-SF process was proposed, as displayed in Fig. 11(a–b), to combine M3:2 and M2 HSSs to achieve excellent mechanical performance [109,110]. Two different HSSs (alloy 1 and alloy 2) are melted and sprayed on a flat substrate simultaneously. The alloy 1 droplets in the atomization cone are initially deposited on the substrate to create the lowest layer of the deposit as the substrate advances horizontally to the right. The top layer is then formed by the alloy 2 droplets that are later deposited in the atomization cone. A gradient zone is created between the two layers after the two spray cones have been crossed over and mixed in the overlapped region, as illustrated in Fig. 11(c). It is evidenced that the preheated ceramic substrate contributes to reducing the porosity at the bottom of the deposit, and the overlap of the two alloys helps to improve the bonding of the interface layer. Experimental results declared that for the combination of M3:2 and M2 HSSs, the austenitizing temperature was preferably 1180 °C, and the hardness could reach 66 HRC.

Overall, as revealed in Fig. 2, the predominant AM technique for the manufacture of HSS components generally includes three main processes: PBF, DED, and MJ. These processes vary depending on the different metallurgical mechanisms. Their deposition rates, process characteristics, and attendant microstructure/mechanical properties are listed in Table 4.

3. Modeling the AM process of HSS

The predictions of solidified features and microstructural development during AM procedures are important because they would minimize the amount of machining necessary to create the component. For instance, the number of experimental iterations required to get to the final product might be decreased by researching the microstructure morphology and production process. Due to the many common characteristics of PBF and DED processes in the modeling process, for the sake of simplicity, the theoretical modeling and relationships involved in PBF and DED processes will be described in Section 3.1. On the other hand, compared with PBF and DED, the SF process has significant differences during modeling. Therefore, the theoretical modeling and research progress involved in the SF process will be discussed in Section 3.2.

3.1. *Powder bed fusion and direct energy deposition processes*

3.1.1. *Powder delivery*

During the DED process, powder delivery can be quantified by powder efficiency, which depends on the nozzle geometry, angle, and particle size. The powder feeding angle and speed significantly affect the powder flow shape, blown powder temperature distribution and laser intensity distribution [114]. The powder efficiency η_p can be simplified as,

$$\eta_p = 1 - \exp\left(-2r_m^2 / r_p^2\right) \quad (1)$$

where r_m is the radius of the molten pool, r_p is the radius of the powder flow. The powder volume concentration or the number of coaxially blown particles can be expressed [115],

$$N(r_b, l) = N_{max}(l)\exp\left(-2r^2 / r_p^2\right) \quad (2)$$

where r_b denotes the distance from the beam centerline, l represents the working distance between the laser and powder, and N_{max} represents the maximum volume concentration. These expressions contribute to a deeper understanding of how the laser beam interacts with the powder stream before it enters the molten pool.

3.1.2. *Energy input*

To comprehend the development of the temperature field throughout the AM deposition process, the heat energy

absorbed by the feedstock materials must be quantified. In the case of laser beams, the study indicated that laser attenuation results in a 25% loss of power reaching the molten pool's surface [116]. The spectrum and absorption rate of the molten pool and flying particles determine the laser radiation. Solute distribution, evaporation and convection also affect changes in absorption/attenuation. A laser surface coupling coefficient A(T) is provided to simplify complicated laser attenuation and particle absorption in response to the demanding radiation. A temperature-dependent equation may be used to express the coupling coefficient [117],

$$A(T) = \sqrt{8\varepsilon_0 \omega \rho_e(T)} \quad (3)$$

where ε_0 represents the permittivity of free space, ω denotes the angular frequency of laser radiation, and $\rho_e(T)$ denotes the temperature-dependent resistivity. Eq. (3) can be employed to estimate attenuation/absorption effects. Meanwhile, the volume energy density E_v is utilized to estimate the theoretical energy of the laser beam under various process conditions. The laser power P_l, scanning speed v_s, hatch distance Δy_s, and layer thickness D_s are utilized to calculate the laser energy density [118],

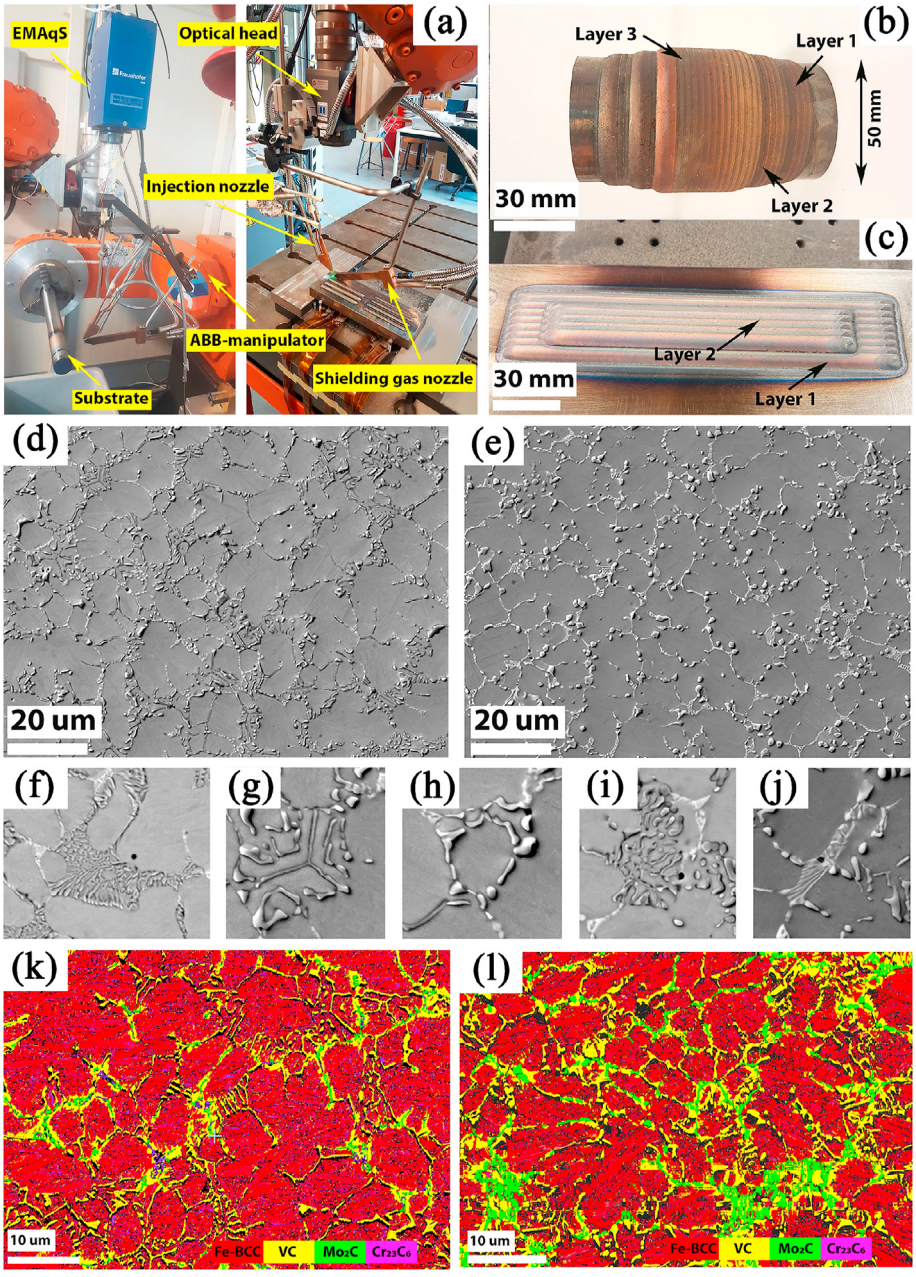

Fig. 9 – (a) High-power DED device. Micrographs of the high-carbon HSS (b) without tungsten element and (c) with tungsten element. (d) SEM micrographs showing the dendritic microstructures of high-carbon HSS without tungsten element and (e) high-carbon HSS with tungsten element. (f–j) SEM images of the high-carbon HSS show the various morphologies of the carbides formed during the AM processes. (k) and (l) Phase map of the HSS (k) without tungsten element and (l) with tungsten element [27].

Table 2 – Processing window of various HSSs for the DED process.

Grade	Laser power(W)	Scanning speed (mm/s)	Powder feed rate (g/min)	Spot diameter (mm)	Layer increment (mm)	Shielding gas (L/min)	Tracks overlap(%)	Refs
M2	850	8.1	60	1.5	0.7			[75]
T15	600	8	3.6			20		[74]
M2	1250	5	15	3				[77]
V-rich HSS	1900–3200	5–15	11–18	5			45	[33]
HC-HSS	2200–2400	5	15	5			45	[27]
HSS	2000–2200	5	13				50	[78]
HSS	2200–2400	5	14–16	5–7				[37]
CPM9V	1700–2700	3.3–13.3	5–15	3		15–25		[79]
M2	400	1–15	1–10	0.3	0.15–0.5			[76]
HSS	800	14.2	5	1		2.5		[80]
HSS	2000			1.4				[81]
M4	900	14	4.5	1	0.25	8	50	[82]
CPM10V	900–1200	15	5–15	2.7			35	[83]
CPM9V	2500	7.6	20	2			30	[84]
CPM10V	2500	7.6	16	2			30	[84]
CPM15V	3000	8.6	11	2			30	[84]
M4	2750	8.6	9	2			50	[84]
CPM10V	2073	3.9	10	1.8–3.4			50	[85]
CPM15V	2400	4.7	15	2.3				[85]
M2	600	6.7	4	1.6		30	30	[86]
D2	2000	14.17		0.56				[87]
M2	2000	60		6			50	[88]

$$E_v = \frac{P_l}{v_s \cdot \Delta y_s \cdot D_s} \tag{4}$$

Low energy density is favorable to forming a thinner layer, but provides dense products with poor surface roughness. The scanning speed in SLM determines the length of the molten pool. Higher scanning speed leads to longer and thinner molten pools, which may break into several smaller molten pools due to Rayleigh instability [119].

For lasers and electron beams, the radius and power density distribution are crucial factors throughout the PBF process. The axisymmetric Gaussian profiles are often followed by the power density distribution of the heat source [120],

$$P_d = \frac{fP}{\pi r_b^2} \exp\left(-f\frac{r^2}{r_b^2}\right) \tag{5}$$

where P denotes the total power of the heat source, f is the distribution factor, r_b is the radius of the heat source and r denotes the radial distance. Eq. (5) represents the surface power density distribution of the heat source. The volumetric heat source with a modified Gaussian distribution may be used to describe the heat source during the DED process [121],

$$P_d = \frac{fP}{\pi r_b^2 t_l}\left[\eta_p + (1-\eta_p)\eta_l\right]\exp\left(-f\frac{r^2}{r_b^2}\right) \tag{6}$$

where η_p stands for the proportion of energy absorbed by the powder during flight, η_l refers to the deposit's absorption coefficient, and t_l is the layer thickness.

3.1.3. *Molten pool behavior*

Dimensional tolerances, microstructural features, and the presence of residual stress in the completed product are mostly determined by the behavior of the molten pool during the DED process. The molten pool shape is attractive as an indicator of process effectiveness, depending on many variables involving powder efficiency, wetting behavior, gas flow rate, heat transfer and traverse speed [46]. Despite the molten

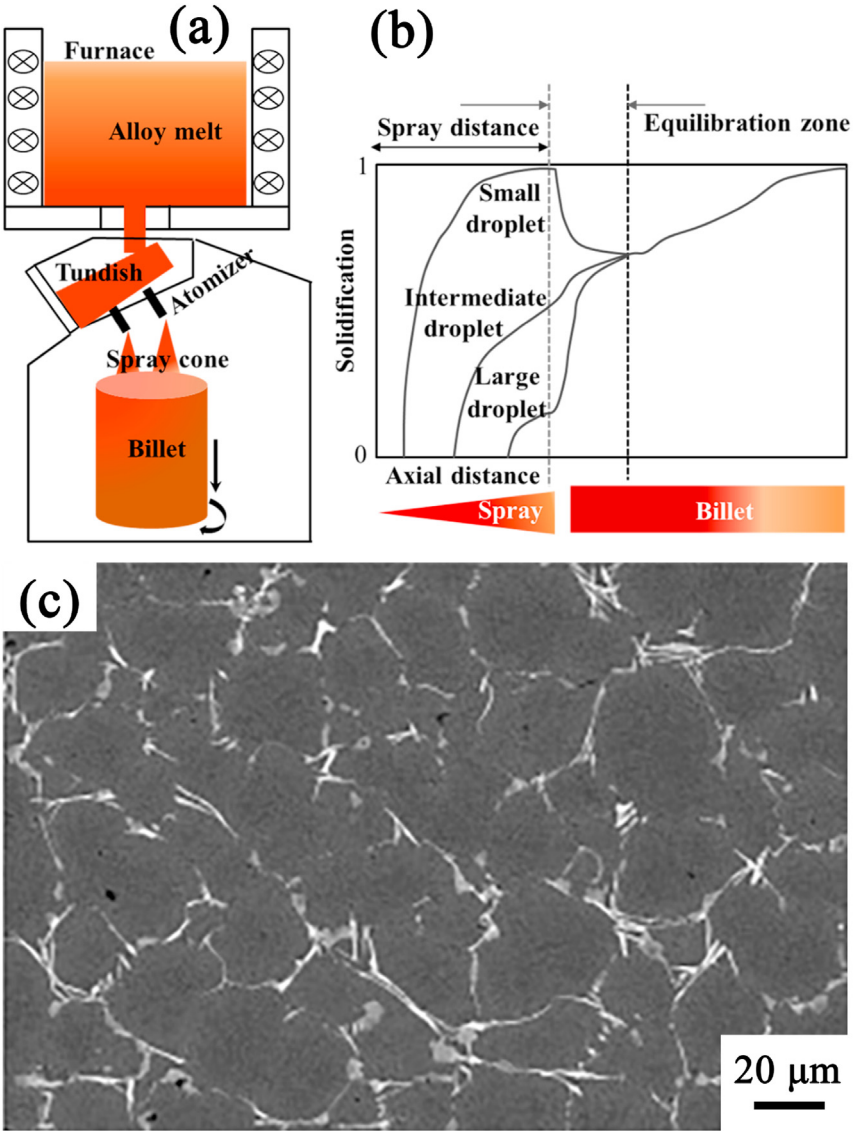

Fig. 10 – (a) A schematic illustration of the SF process, (b) solid fraction change for different sized droplets in the SF process, and (c) microstructure of as-deposited Nb-added M3:2 HSS [40].

Table 3 – Processing windows of various HSSs for SF process.

Grade	Super heat (°C)	Metal flow rate (kg/s)	Atomization pressure (MPa)	Atomization gas	Deposition distance (mm)	Rotation speed (r/min)	Diameter of the delivery tube (mm)	Refs
M3:2	160–180		0.45–0.5	N2	420–450		4	[40,102]
A30		0.5	1.5	N2		90		[103]
T15	~150		0.7–0.8	N2				[104]
M3			0.5	N2	450–500			[105]
M2	~150		0.7	N2				[90]
M2		0.28		N2	500			[106]
ASP30	200		0.6	N2				[38]
HSS	~150	0.42	0.55	N2				[107]
M3:2	~150		0.5	N2	450–500			[108]

pool elongates with increasing traverse speed, the depth of the molten pool becomes shallower [122]. In contrast to single-layer deposition, the molten pool shape becomes more asymmetric for multi-pass deposition. Larger molten pools are favorable to grain evolution since they have more time to develop. Smaller dendritic arm spacing (DAS) and finer microstructural components may be achieved by using the DED technique, which uses low power and a smaller molten pool [123].

The thickness and radius of the molten pool exhibit a temperature gradient that is proportional to power. Between 100 and 1000 K/mm of temperature gradient runs throughout the molten pool's width or radius [124,125]. By speeding up the powder feeding, powder injection impacts the molten pool superheat and lowers the molten pool temperature. As the laser power decreases, the distribution of the molten pool temperature becomes more uniform, and the peak temperature increases with increasing specific energy. The study showed that the local heat loss at the molten pool/vapor interface can be given as [126],

$$q_{\text{loss}} = h_c(T - T_\infty) + \varepsilon\sigma\left(T^4 - T_\infty^4\right) + \rho_l V_{dv} L_v \tag{7}$$

where h_c is the convective coefficient, ε is radiation emissivity, σ is the Stefan-Boltzmann constant, T_∞ is the ambient temperature, ρ_l is the molten fluid density, L_v is the latent heat of evaporation, V_{dv} is the boundary movement speed caused by evaporation. As anticipated, the phase-field model (PFM) in Fig. 12 accurately predicted the shift in a temperature gradient in the molten pool [74]. The highest temperature gradient is concentrated near the bottom of the molten pool, reaching 1.85e+06, as shown in Fig. 12(a). The vector represents the gradient magnitude and direction. The cooling rate ranges between 262 and 5090 K/s, with the lowest rate occurring near the bottom of the molten pool, as seen in Fig. 12(b). When reaching the top layer along with the bottom domain, the cooling rate gradually increases to 3480–5090 K/s. It shows that the model can be utilized to predict temperature development and molten pool distribution.

3.1.4. *Solidification behavior*

Heat transfer governs the molten pool's solidification behavior, which may be separated into three major events: (1) heterogeneous nucleation, (2) heat/mass transfer in the mushy zone, and (3) microstructural evolution. The link between the molten pool temperature gradient G and the solidification rate V for surface laser processing is written as [46],

$$\frac{G^{3.4}}{V_{sol}} \approx 8113\left[\sqrt{3\frac{-4\pi N_0}{3\ln(1-\varphi)}}\right]^{3.4} \tag{8}$$

where N_0 denotes the quantity of nucleation sites, and φ denotes the volume proportion of equiaxed grains. Meanwhile, the study showed that the solidification velocity is pertinent to the laser feed rate and the molten pool shape caused by powder addition and surface wetting [125].

Additionally, several studies have shown that the microstructure is directly affected by a temperature gradient, which in turn impacts the grain orientation and growth patterns [127,128]. To confirm the evolution behavior of HSS grains fabricated by AM process, Jammal et al. [74] established a PFM

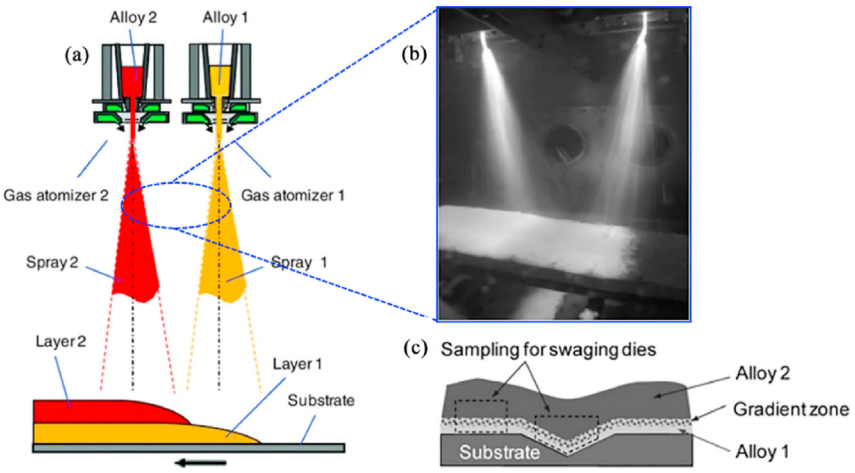

Fig. 11 – (a) Schematic diagram of the co-spraying process using two different HSSs (M2 + M3:2). (b) In-situ co-spray deposition process, (c) illustration of the transverse section of the deposit [109,110].

coupled with nucleation, phase transformation and thermal transfer to simulate the solidification process of single-track T15 HSS manufactured by the DED process. It was discovered that throughout the simulation domain, the microstructural evolution of T15 HSS manifested as cellular and equiaxed zones. Fig. 13 depicts the PF simulation results of the nucleation and growth process of the molten pool at different stages, where the grain ID = 0 represents the liquid phase, and the other grain IDs represent each solid phase grain with different orientations. It can be observed from Fig. 13(a) that cellular microstructure appears during the initial stage of solidification. As the temperature drop rate gradually decreases, new crystal nuclei begin to form, and equiaxed grains gradually grow, as shown in Fig. 13(b). In Fig. 13(c), it can be found that the cellular region stops growing with the formation of equiaxed grains. Fig. 13(d) shows that as the solidification progresses, the nucleation density greatly increases, and the equiaxed grain size gradually increases compared to the early stage of solidification. The final solidification is completed at t = 1000 μs during the simulation domain, as shown in Fig. 13(e). Correspondingly, the experimental SEM image is displayed in Fig. 13(f). It can be seen similar patterns are observed and the SEM image shows the cellular and equiaxed microstructure. Even though the grain size progression patterns shown by PFM and SEM images are comparable, there are variances in the average grain sizes. Meanwhile, PFM incorporates liquid-solid phase change, with no consideration given to solid-solid phase transformation. Moreover, it is a challenge to in-situ observe the solidification process of HSS due to the poor imaging contrast caused by a wealth of high-density alloying elements. Therefore, Jammal et al. argued that it was difficult to accurately compare the modeling results with experimental data even though the simulation analysis showed similar trends to the experimental results.

3.2. *Spray forming process*

In this section, various well-known analytical models proposed during the development of the SF are summarized. The previous research progress can be roughly divided into four key regimes in terms of atomization, droplet flying, deposition and solidification of preforms.

3.2.1. *Atomization regime*

The kinetic energy of the impinging high-speed gas jet disintegrates the continuous metal flow into droplets in the gas atomization. Generally, the metal flow is considered to have been torn, secondary atomized and spheroidized. The study found that various alloy melts have different susceptibilities in terms of atomization. Therefore, the mass distribution and average size of droplets are significant parameters for evaluating the atomization ability, which directly determines the cooling rate of the jet stream, and then affects the solidification microstructure of the deposited billet. The mass probability density function $g(d)$ of the droplet size distribution has been proposed by many scholars and can be expressed [129,130],

$$g(d) = \frac{1}{\ln \sigma_g \sqrt{2\pi}} \left(\frac{1}{d}\right) \exp\left[\frac{(\ln d - \ln d_m)^2}{2 \ln^2 \sigma_g}\right] \tag{9}$$

where σ_g is geometric standard deviation, d is particle diameter, d_m is mass median particle diameter. In particular, it is difficult to accurately calculate the particle size distribution in the atomization cone because of the complexity of the atomization process. Based on various assumptions, numerous investigations have been used to predict the mass mean diameter of droplets [131–134]. Among these, a semi-empirical equation derived by Lubanska et al. was widely employed to predict the droplet size [135]:

$$d_m = DK_a \left[\xi \left(1 + \frac{\dot{M}}{\rho_g v_{gi} A}\right) \left(\frac{\gamma_m}{\rho_m v_{gi}^2 D}\right)\right]^n \tag{10}$$

where D represents the diameter of the melt delivery nozzle, ξ is metal-to-gas kinematic viscosity ratio, γ_m is melt surface tension, $\dot{M}$ is metal mass flow rate, ρ_g is gas density, v_{gi} is initial gas velocity, A is atomizer exit orifice cross-sectional area, ρ_m is metal density and K_a is experimental constant. In

Table 4 – Comparisons of representative AM processes.

Process	Layer thickness (μm)	Deposition rate	Dimensional accuracy (mm)	Surface roughness (μm)	Advantages	Disadvantages	Refs
SLM	20–100	Depending on the laser spot size, scan speed, number and complexity of parts	High ±0.04	6–10	High forming precision, shape/size flexibility, no post-processing	ineffective deposition and small ingot size	[111]
SLS		Depending on the laser spot size, scan speed, number and complexity of parts	High ±0.1		Self-supporting properties, complex shapes and high flexibility	Low density, rough surface, needs post-processing	[51]
DMLS	20–100	Depending on the laser spot size, scan speed, quantity and complexity of parts	High ±0.05	14–16	No pre- or post-processing, quick manufacturing cycle, cheap cost	Spheroidization effect, sintering deformation, loose density	[112]
EBM		Depending on beam spot size, scan speed, component number, and complexity	High ±0.4	20–50	High energy density, a tiny heat-affected zone, little deformation, and a high level of production	Low ingot size, poor forming precision, and excessive cost	[32]
DED	254	0.1–4.1 cm^3/min		~40	Fabrication of gradient materials, sophisticated surface repair, cost savings and a rapid production cycle	poor accuracy, easy to break, and low material usage	[113]
SF	/	Depending on the nozzle's shape, quantity, atomization, and deposition distance	Low	/	High deposition efficiency and large ingot size	intrinsic porosity that needs further processing	[98]
Co-SF		Depending on the shape, quantity, and atomization performance of the nozzles as well as the deposition distance	Low		Higher deposition efficiency and large ingot size	intrinsic porosity, requiring further processing	[110]

Eq. (10), the change in droplet size distribution with melt temperature is ignored. Therefore, droplet size distributions can be calculated.

3.2.2. *Droplet flying regime*

Metal droplets are rapidly cooled under the protection of inert gas, taking away a large amount of latent heat during the flying regime, while the remaining latent heat is taken away through the substrate cooling medium (water-cooling) or lost by the surface of the deposited billet. The gas flow field is the medium in which the droplets move. It is determined by the atomization pressure, the shape of the atomization cavity and the interaction between the gas and droplet, which affects the flying trajectory and mass flow rate distribution of the metal droplet. The gas velocity v_g could be derived as follows [98,136,137],

$$v_g = \left[2g\left(\frac{n}{n-1}\right)P_1V\left(1-\frac{P_2}{P_1}\right)^{\frac{n-1}{n}}\right]^{1/2} \tag{11}$$

where P_1 is initial conditions of pressure, P_2 is final conditions of pressure, n is molar heat capacity ratio, V is volume, and g is acceleration. The gas temperature (T_e) at the nozzle exit could be expressed as [136,138],

$$\frac{T_0}{T_e} = 1+\frac{\gamma-1}{2}\left\{C_M\left[\frac{2}{\gamma-1}\left[\left(\frac{P_0}{P_e}\right)^{\frac{\gamma-1}{\gamma}}-1\right]\right]^{1/2}\right\}^2 \tag{12}$$

where T_0 is stagnation temperature, C_M is correlation coefficient, γ is specific heat ratio of atomized gas, P_0 is stagnation pressure, and P_e is exit gas pressure.

The mass flow rate distribution of droplets affects the formation and yield of the deposited billet, many scholars have carried out large quantities of experimental studies [133,139,140]. The findings showed that the correlation had been responsible for the change in mass flow as a function of axial distance [98],

$$\frac{\dot{m}D_g^{\,3}}{\dot{M}D} = C_1\left(\frac{z}{D_g}\right)^{C_2}\left(\frac{\rho d^2 v_g}{18\mu_g D_g}\right)^{-C_3} \tag{13}$$

where $\dot{m}$ is mass flux, $\dot{M}$ is metal mass flow rate, C_1-C_3 are experimental constants and z is axial distance. The atomization gas not only delivers the energy required for the dispersion of the melt flow, but also interacts with the droplets during their flight. Ignoring the influence of gravity, as discussed in Refs. [139,141,142], the equation of droplet motion can be described as follows,

$$\frac{dv_d}{dt} = \frac{3}{4}\frac{C_D\rho_g}{d\rho_d}(v_g - v_d)|v_g - v_d| + g\left(1-\frac{\rho_g}{\rho_d}\right) \tag{14}$$

$$C_D = \begin{cases} 24/R_e & 0 < R_e < 1 \\ 24/R_e^{0.646} & 1 \le R_e < 400 \\ 0.5 & 400 \le R_e < 3\times10^5 \end{cases} \tag{15}$$

where v_d is droplet velocity, v_g is gas velocity, ρ_d is droplet density, ρ_g is gas density, C_D is droplet drag coefficient, and Re is Reynolds number.

Pi et al. [143] proposed a computational model to predict the motion and thermal behaviors of individual droplets of spray-formed W18Cr4V HSS according to Newton's laws of motion and the convection heat transfer mechanism. The developed model predicted the velocity, temperature, heat transfer coefficient, and solid fraction of individual droplets, and the results are presented in Fig. 14. The model's settings were as follows: the starting gas velocity was set to 300 m/s for droplet sizes between 20 and 200 μm; the deposition distance was 0.5 m; the superheat degree was 100 K, and the ratio of the gas-to-metal mass flow rate was 0.55. As observed in Fig. 14(a), the velocities of droplets of various sizes quickly climbed to a maximum value and then progressively dropped. This observation demonstrated that the droplet diameter had a significant impact on the droplet velocity. The velocity of the smaller-diameter droplets showed a sharp rise and fall, while the velocity change of the larger-diameter droplets was relatively gentle. The corresponding contour of the velocity distribution was presented in Fig. 14(b). Meanwhile, the thermal behavior and temperature distribution of droplets with different diameters were presented in Fig. 14(c and d), respectively. As expected, it can be observed that smaller diameter droplets nucleated at shorter distances due to higher cooling rates, resulting in lower temperatures upon reaching the deposition surface. This means that smaller diameter droplets had higher initial heat transfer coefficients, as displayed in Fig. 14(e). The gas accelerated the droplet sharply, reducing the relative velocity. As a result, the heat transfer coefficient dropped dramatically. Subsequently, the heat transfer coefficient increased again. It was hypothesized that the decrease in gas velocity increased the relative velocity

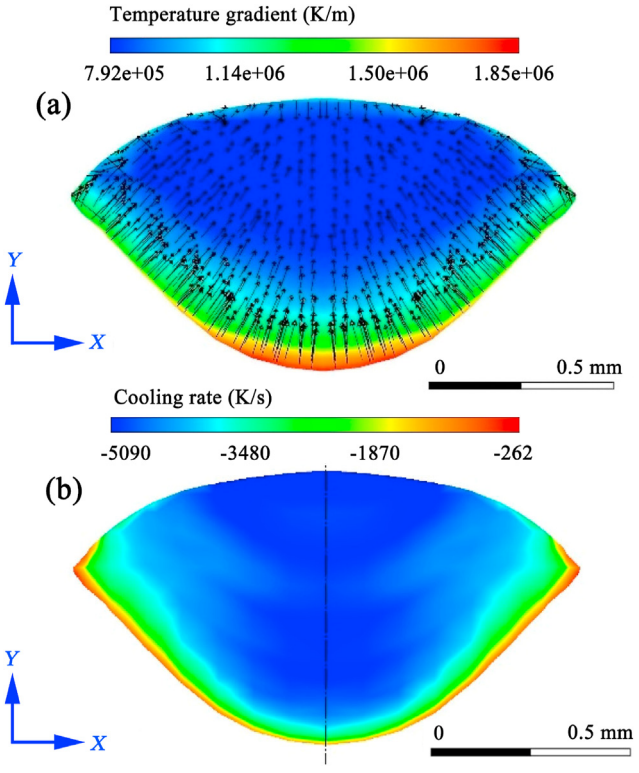

Fig. 12 – (a) Temperature gradient and (b) cooling rate magnitude distribution in the molten pool during powder bed fusion and direct energy deposition processes [74].

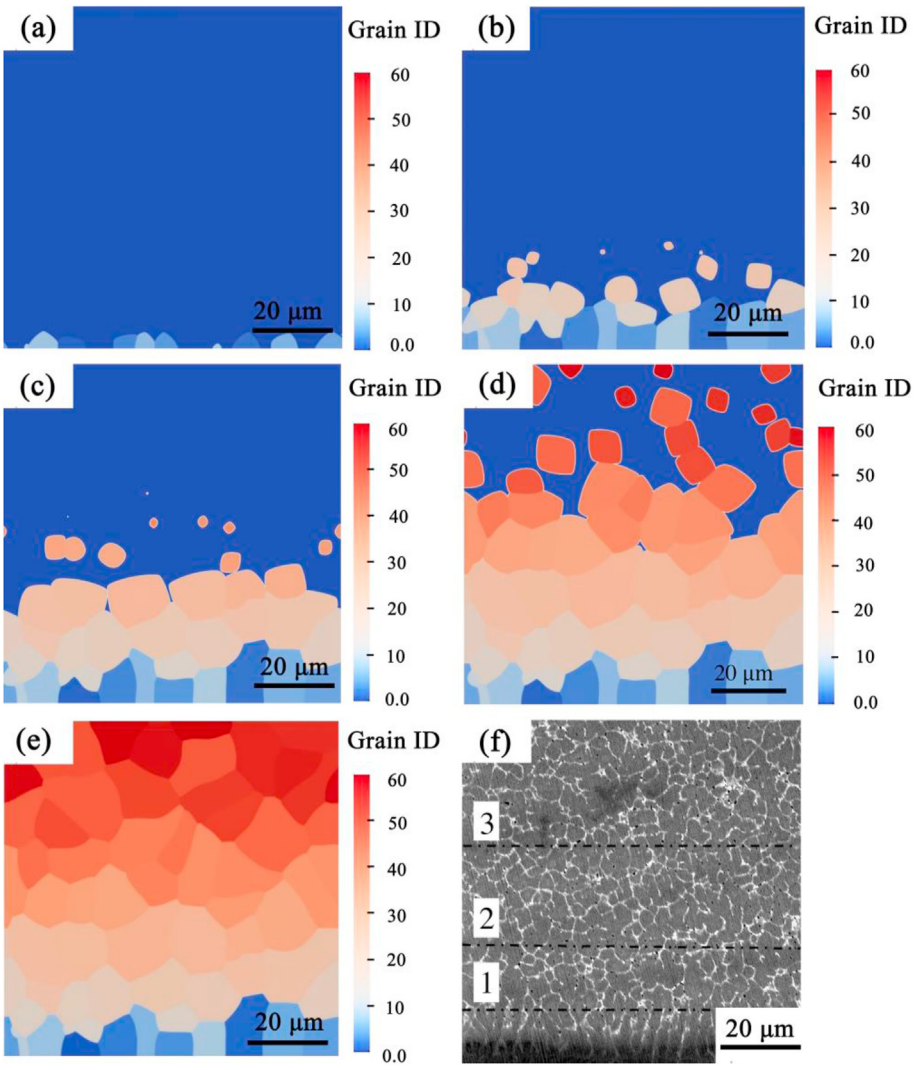

Fig. 13 – Simulation results of the nucleation and grain growth process during the solidification process T15 HSS at different stages: (a) 100 μs, (b) 300 μs, (c) 500 μs, (d) 800 μs, (e) 1000 μs, and (f) SEM microstructure profile distribution [74].

between droplets and gas molecules. Moreover, the temperature history of the droplet influenced its solidification behavior, as shown in Fig. 14(f), which demonstrates that the solid portion of the droplet reduced as its diameter increased. Since the model could accurately anticipate the motion and cooling of individual droplets, it was utilized in conjunction with numerical simulations to verify its correctness.

3.2.3. *Deposition regime*

Most metal droplets are semi-solid and have large kinetic energy when they reach the deposition surface. The droplets undergo complex physical and chemical changes due to violent collisions and bounce off. At present, despite numerous research efforts that have been reported to reveal and analyze the deposition mechanisms, there is a lack of accurate and clear understanding of this process. Among these, the deposition rate as the basis of preform forming and quality is proved to be Gaussian distribution [98,140]. Trapaga et al. [144] studied the droplet's extension on the substrate, the interaction of adjacent droplets, and the splashing behavior of droplets impinging on free liquid surfaces. The results indicated that viscosity plays a dominant role in droplet expansion. Thus, the sticking efficiency *SE* (shape and yield of deposited billet are affected) was used to describe the relationship between surface solid fraction and droplet sticking or bounce-off, which was expressed as follows [133],

$$SE = SE(\theta) + (\eta_s f_s + \eta_L f_L)\varepsilon_\infty \tag{16}$$

where *SE* is sticking efficiency, η_s is solid sticking coefficients, η_L is liquid sticking coefficients, f_s is solid fraction, f_L is liquid fraction, and ε_∞ varies from 0 to 1. Moreover, Cai et al. [136] developed a model for estimating porosity based on particle packing theory. They hypothesized that: (1) The porosity in the deposited billet could only be packing structure or solidification shrinkage (represented only by volumetric shrinkage). (2) The droplets were divided into two types during the

atomization cone: fully liquid and completely solid. Accordingly, a porosity coefficient Φ was described as,

$$\Phi = \left(\frac{1-\Gamma}{\Gamma}\right) - \left(\frac{1-\overline{f_s}}{\overline{f_s}}\right)(1-\beta) \tag{17}$$

where $\beta = 1 - \rho_m/\rho_s$ is the solidification contraction, $\overline{f_s}$ is the average solid fraction, and Γ is particle packing density. Based on the aforementioned basic assumptions, the porosity p can be evaluated as,

$$p = \begin{cases} \Phi\Gamma & \Phi \geq 0 \\ \dfrac{\Phi\Gamma\beta}{\Phi\Gamma - (1-\beta)} & \Phi < 0 \end{cases} \tag{18}$$

3.2.4. *Solidification regime*

The solidification regime is mainly reflected in the heat transfer and cooling process of the deposited billet, and heat dissipation is generally carried out in three approaches: namely convection heat dissipation of the deposited billet, radiative heat dissipation and heat transfer. Because of the temperature differential between the surface and inside of the deposited billet, some scholars have developed more accurate numerical models [140,145–148], as follows,

$$\rho C V \frac{dT}{dt} = -kA\frac{d^2T}{dz^2} + \rho L V \frac{df}{dt} \tag{19}$$

where ρ is density, C is specific heat capacity, V is volume, T is temperature, f is solid fraction, k denotes thermal conductivity, and A denotes the cross-sectional area. For undercooling analysis, homogeneous and heterogeneous undercooling models were discussed in detail [149–152], respectively. The expressions are as follows,

$$\Delta T_{hom}^2 = \frac{16\pi\gamma_{sl}{}^3\Omega^2 T_l^2}{3k_B(T_l - \Delta T_{hom})h_f^2 \ln\left(0.01 N_v V_d \Delta T_{hom}/\dot{T}\right)} \tag{20}$$

$$\Delta T_{het}^2 = \frac{16\pi\gamma_{sl}{}^3\Omega^2 T_l^2 f(\theta)}{3k_B(T_l - \Delta T_{het})h_f^2 \ln\left(0.01 N_v V_d \Delta T_{het}/\dot{T}\right)} \tag{21}$$

where ΔT_{hom} and ΔT_{het} represent the degree of homogeneous and heterogeneous undercooling, respectively. γ_{sl} is solid/liquid interface energy, Ω is atomic volume, T_l is liquidus temperature,

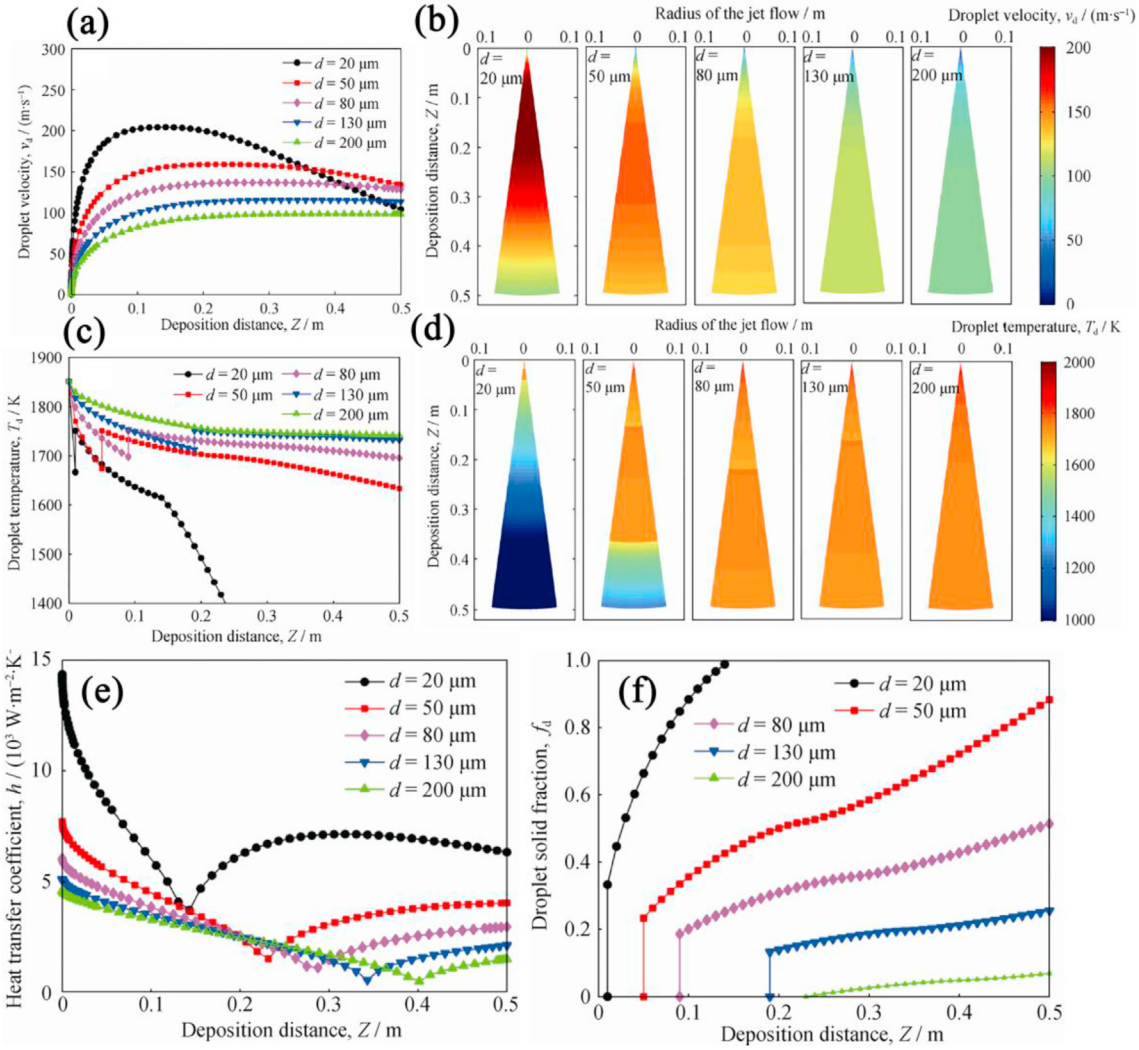

Fig. 14 – Modeling results of the deposition behavior of individual droplet of W18Cr4V HSS during SF process [143]: (a) velocity, (b) velocity distribution, (c) temperature, (d) temperature distribution, (e) heat transfer coefficient, and (f) solid fraction.

Table 5 – Summary of particle engulfment models for critical solidification velocity.

Model	Prediction	Equations	Refs
Kinetic/thermal/thermodynamic	engulfment	$V_{cr} = \frac{0.14\beta}{\eta r}\left(\frac{\alpha}{\beta r}\right)^{1/3}$	[155]
Kinetic model	engulfment	$V_{cr} = \left[\frac{4\psi(\alpha)K_B T_d \sigma_{SL} a_0}{9\pi\eta^2 r^3}\right]^{1/2}$	[153]
Thermal/kinetic model	engulfment	$V_{cr} = \frac{\Delta\sigma_0 a_0}{6(n-1)\eta r}\left(2 - \frac{K_p}{K_L}\right)$	[154]

h_f is the latent heat of fusion, $\dot{T}$ is the function of the droplet size, V_d is droplet volume, $f(\theta)$ is contact angle factor, N_v is the number of liquid atoms per unit volume, and k_B is Boltzmann's constant. Three typical kinetic/thermal/thermodynamic models were proposed to evaluate the criteria for particle entrapment or rejection [153–155]. The critical solidification front velocity V_{cr} is provided for each model. The details are summarized in Table 5.

In summary, SF is a complex process involving heat transfer, mass transfer, metallurgy, chemistry and fluid mechanics. This process principally includes droplet atomization, rapid solidification during flight and final solidification that occurs when high-velocity droplets impinge on the cooling substrate and bounce off.

4. Microstructural evolution of AM-fabricated HSS

The microstructural characteristics (e.g., grain size, carbide morphology and distribution) of AM-manufactured HSS components are very susceptible to the thermal history during manufacturing, which includes cooling rates, large temperature gradients, and other factors [156]. Compared with the conventional solidification process, despite the cooling rate of the AM process (10^3–10^7 K/s) is higher than the normal cooling rate (10^{-3} to 10^2 K/s), the resultant microstructure of AM-fabricated HSS still maintains its basic characteristics, that is, dendrites are encircled by an interdendritic network of eutectic carbides that is more or less continuous [157]. The fabricated microstructure has a matrix of austenitic decomposition products (usually martensite, or bainite with a small amount of retained austenite), spherical secondary carbides, and eutectic carbides that are distributed both in the interdendritic or intercellular regions (M_2C, M_7C_3, and MC) as well as inside the eutectic cells (MC). Post-heat treatment, which modifies the microstructural evolution of AM-fabricated HSS, is an effective way to improve mechanical properties and tribological behavior. Its typical microstructure is characterized by eutectic carbides and dispersed precipitation of secondary carbides distributed in tempered martensite. It can be seen that carbides play a critical role in prolonging the service life of HSS. For AM-processed HSS, the size, morphology, and distribution of eutectic carbides change significantly with higher cooling rates. However, the overall volume percentage of eutectic carbides and the volume fraction of each eutectic carbide are mostly determined by the chemical composition, with little impact from the cooling rate [158–161]. Therefore, given the specific alloy composition, the solidification process determines the size, shape, and spatial distribution of the microstructure. In this chapter, the microstructural evolution of HSS components manufactured by AM is reviewed.

4.1. Carbide precipitation behavior

4.1.1. Precipitation dynamics

The composition of the most widely used AISI M2 HSS is the foundation of the HSS alloy design. The obvious variation of different grades of HSS is the modification of carbon and vanadium content. Therefore, the chemical composition of various grades of HSS principally falls into the following ranges: 0.9–2.5% C, ~10% W, ~7% Mo, 3–7% Cr, 2–10% V, ~12% Co and Fe balance. Fig. 15 shows the precipitation sequence of the microstructure of HSS with different carbon content under equilibrium regimes. For carbon content between 0.8% and 1.2% (wt), the pseudobinary section of Fig. 15(a) shows that the

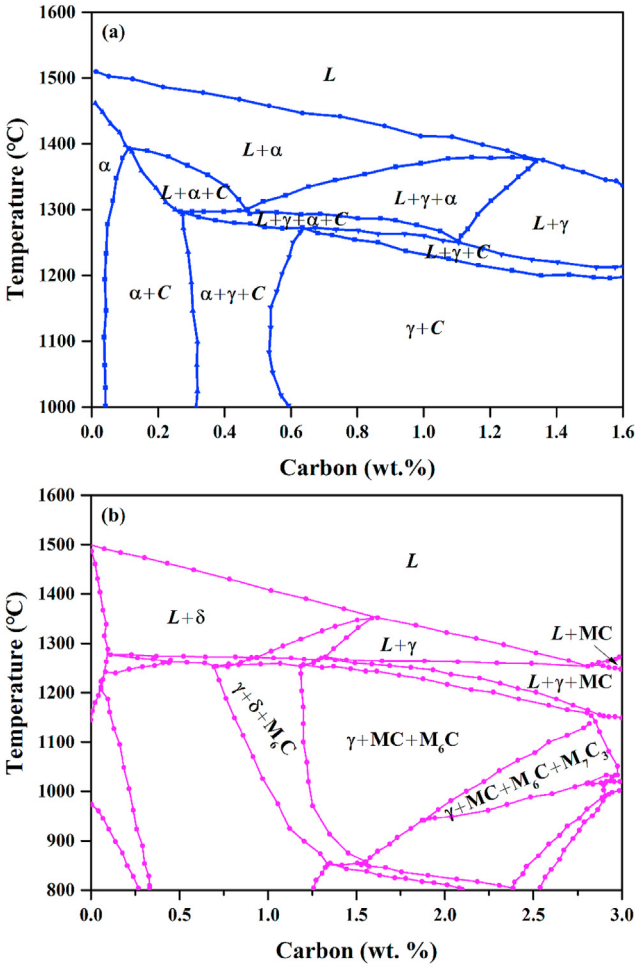

Fig. 15 – (a) Pseudobinary section for Fe–6W–5Mo–4Cr–2V–C HSS using Thermo-Calc software [2] and (b) Fe–5W–5Mo–5Cr–5V–C was predicted using Thermo-Calc software [157].

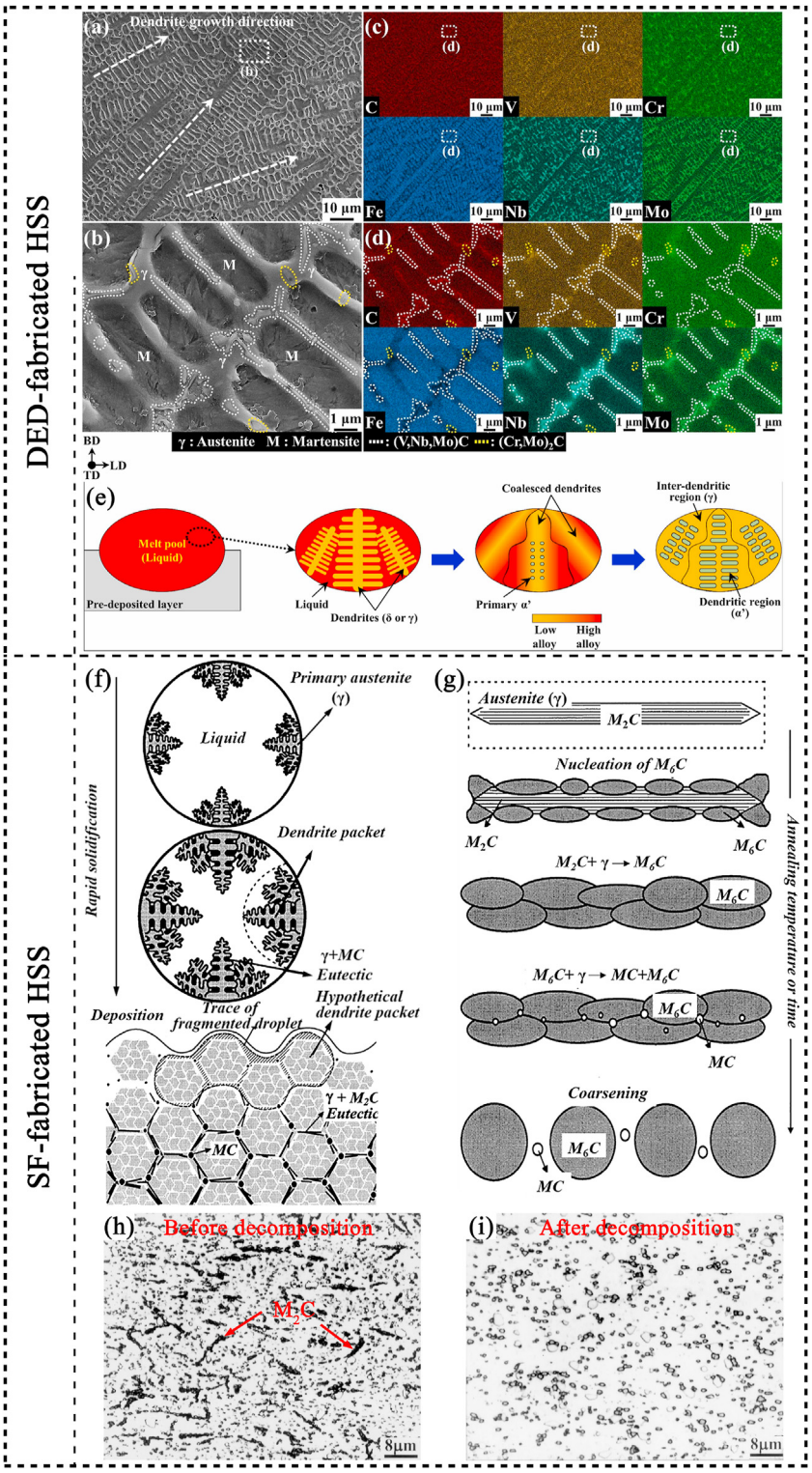

Fig. 16 – Microstructure of the deposited layer of DED-fabricated (Fe–1C–2.6Mo–W–V) HSS [167]: (a) panoramic view and (b) close-up view. EDS map showing the alloying element distributions of (c) panoramic views and (d) close-up views. (e) schematic diagram of solidification during DED, (f) a schematic solidification process during SF, which includes the quick cooling of flying droplets and the comparatively slow solidification on the deposited layer, (g) a schematic explanation of the decomposition behavior of M_2C carbide as a function of temperature or time, (h) M_2C carbide without decomposition, and (i) decomposed at $T = 1200\ ^{\circ}C$ [38].

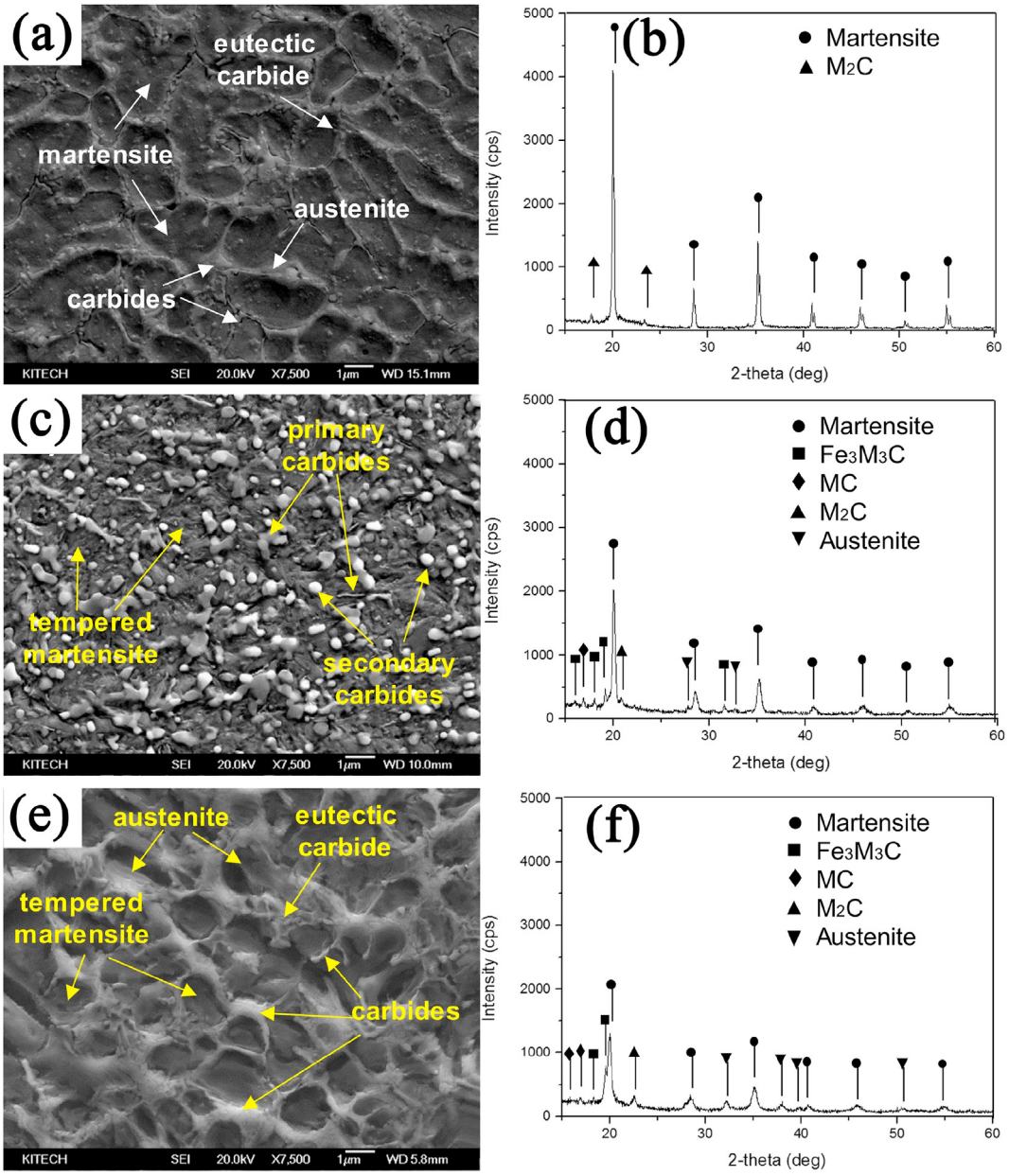

Fig. 17 – Microstructure and XRD analysis results of the DED-fabricated M4 HSS [82]: (a) SEM image without heat treatment, (b) XRD profile, (c) post-deposition quenched-tempered, (d) XRD profile after quenching-tempering, (e) post-deposition tempered, and (f) XRD pattern after post-deposition tempering.

primary crystallization of δ ferrite is completed with the decrease of temperature [2]. As demonstrated in Fig. 15(b), austenite instead of ferrite is the predominant solidification phase for carbon contents more than 1.5% (wt) [157]. Although the prediction in Fig. 15 indicates the formation of austenite and various carbides in terms of MC, M_2C, M_6C, and M_7C_3, it is necessary to emphasize the gap between the prediction and the experimental results needs to be considered because the solidification process usually occurs under non-equilibrium regimes. For instance, If the residual delta ferrite is not completely consumed by the peritectic reaction (depending on the cooling rate and carbon content), it will decompose into a mixture of austenite and carbide, i.e. delta eutectoid [6,162]. The significance of delta eutectoid is that it can affect the mechanical properties of HSS [163]. In fact, there are many controversies with respect to the carbides in the delta eutectoid of HSS, with M_6C [164], which contrasts with $M_{23}C_6$ in another study [165]. Chaus et al. [163] systematically investigated the morphology and origin of the carbide in the delta eutectoid of M2 HSS and indicated that both M_2C and M_6C carbides could simultaneously form delta eutectoid. Meanwhile, in-situ EBSD studies confirmed that delta eutectoid was based on M_2C [166]. Moreover, M2 HSS produced by the LC process results in an incomplete peritectic reaction, δ ferrite and austenite remained to room temperature due to the high cooling rate [76]. It was discovered that the microstructure progressively changed from cellular or dendritic δ ferrite and austenite to martensite and retained austenite as the cladding layer thickness rose.

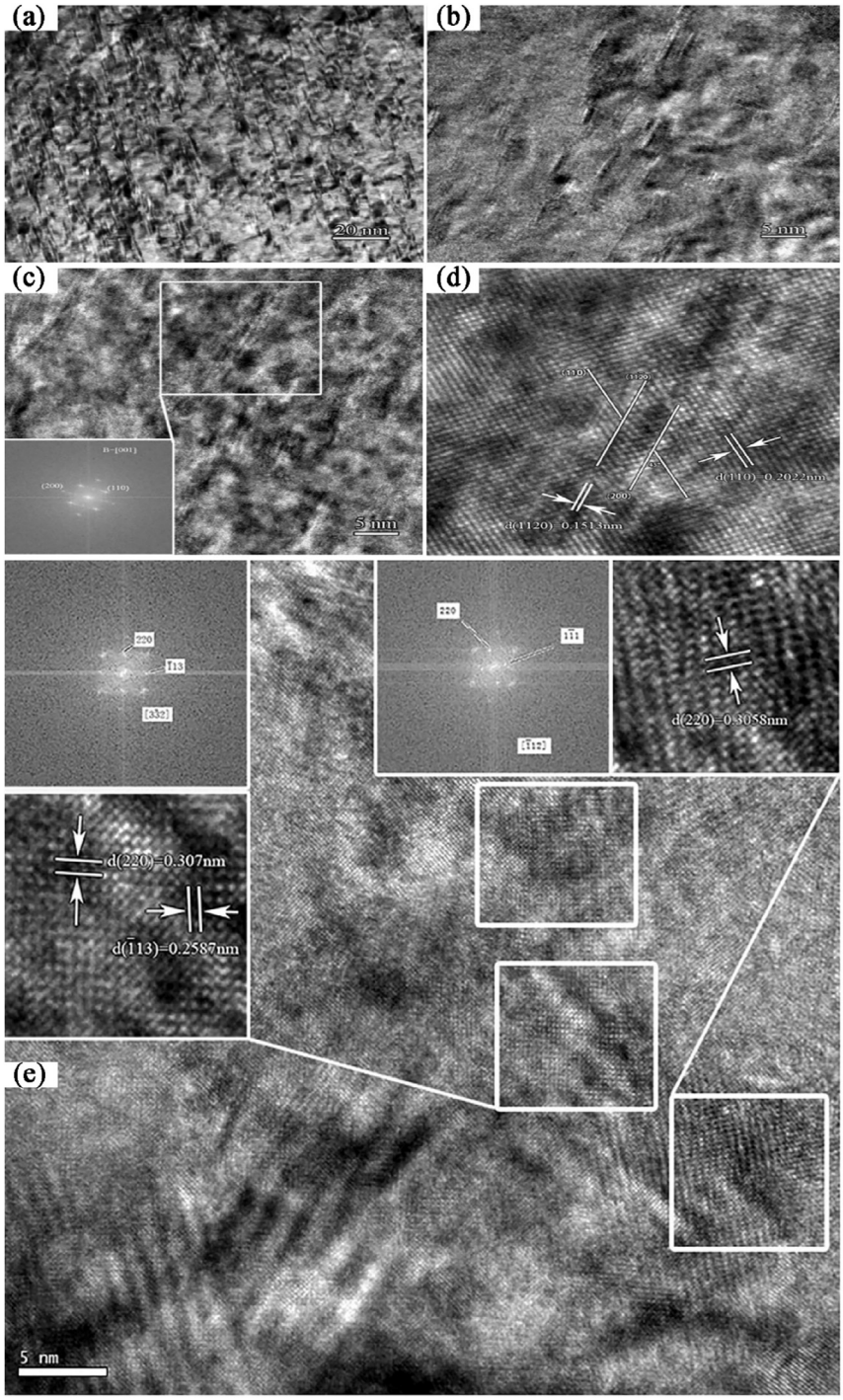

Fig. 18 – (a) Secondary M_2C precipitates in the M3:2 matrix, and (b) M3:2 (2% Nb) HSS, (c) HRTEM image of M_2C carbides in M3:2 (2% Nb) HSS, with the accompanying FFT image inset in (c), (d) IFFT image of rectangle marked in c, (e) HRTEM image of MC carbides precipitated at the matrix in M3:2 (2% Nb) HSS, the insets are the matching FFT and IFFT images of MC indicated by a rectangle [108].

Especially, Fig. 16 comparatively presents the microstructural evolution and carbide decomposition behavior of DED-fabricated Fe–1C-2.6Mo–W–V HSS [167] and SF-deposited high cobalt HSS [38] during rapid solidification. It can be observed that columnar dendrites grow towards the heat source in the deposited layer of HSS manufactured by DED. Fig. 16(a and b) illustrate the formation of fine dendritic arms with secondary dendrite arm spacing (SDAS) of around 1.47–2.51 μm. This fact suggests that fast cooling during DED reduces the solute components' diffusion time and might result in a smaller SDAS. As can be observed in Fig. 16(c and d), carbides often develop in the interdendritic zone and take the shape of plates or rods with lengths ranging from 0.5 to 2 μm. Meanwhile, the alloying elements exhibited obvious

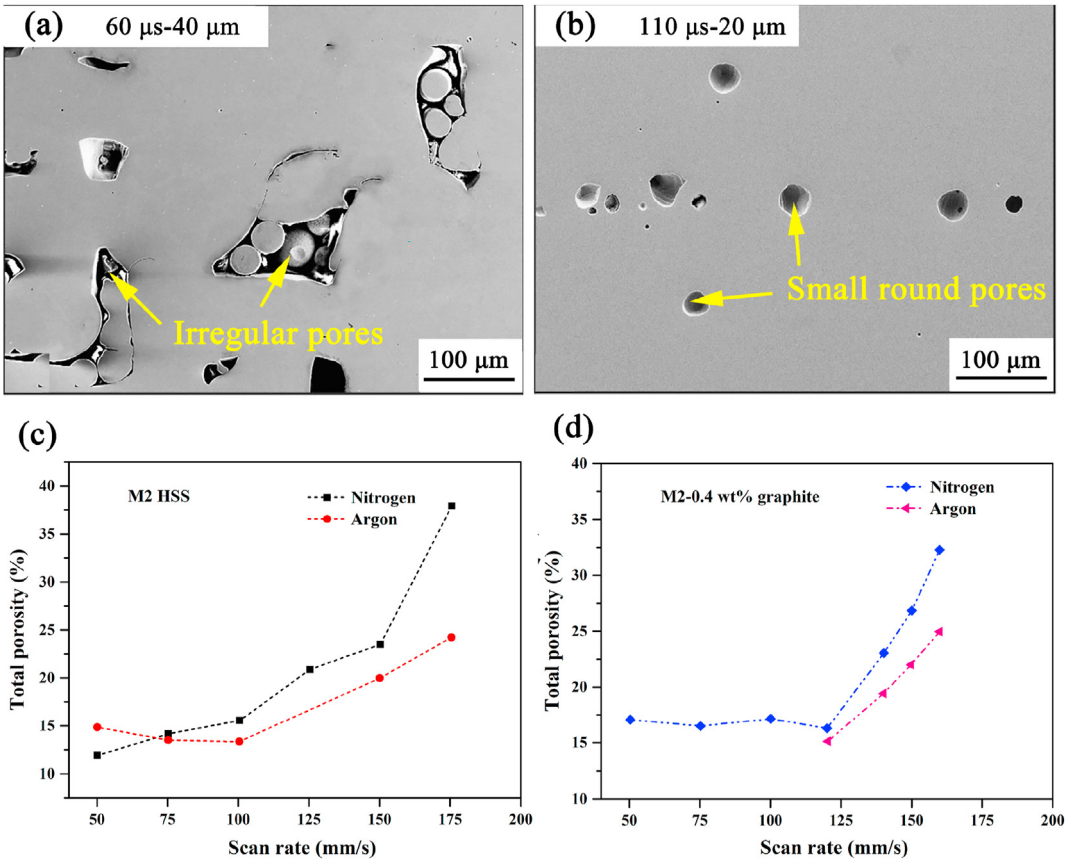

Fig. 19 – Defect morphologies of M3:2 HSS fabricated by the SLM (a) irregular pores and (b) regular small round pores [26]. Influence of process variables on the porosity of M2 HSS processed by DMLS: (c) without and (d) with graphite addition [58].

interdendritic segregation, enriched in C–V–Nb–Mo or C–V–Cr–Mo, as shown in Fig. 16(d). As a consequence of the relative scarcity of solute elements in the dendritic area, the austenite stability of the dendritic region is lower than that of the interdendritic region, as illustrated in Fig. 16(e). By contrast, spray-formed HSS often has spherical MC carbides that are finely and evenly dispersed among discontinuous M_2C carbide networks, as shown in Fig. 16(f). As expected, the production of primary austenite dendrites dominates the initial solidification, and MC carbides form around the dendrites. The droplets split into austenite dendritic packets during deposition, and the liquid that is left fills the voids left by the dendrite packets. As illustrated in Fig. 16(g), metastable M_2C carbides have completely decomposed into MC and M_6C carbides after annealing at elevated temperatures. Comparatively, Fig. 16(h) exhibits the morphology of the M_2C eutectic carbide before decomposition, which still maintains the plate-like shape. After the decomposition treatment by holding at 1200 °C for 1 h, it can be observed that the original M_2C carbides are completely destroyed and the distribution of carbides with the size of 1–2 μm is more uniform, as shown in Fig. 16(i). It should be noted that despite the similar changes in microstructure and phase composition of wrought and cast HSS, the evolution of wrought HSS is not evident after the heat treatment regime. In comparison with cast HSS, MC carbides precipitate from M_6C carbides instead of M_2C at high austenitizing temperatures due to decomposition of M_2C carbides [168]. This mechanism may be defined as M_6C carbides nucleating at the interface between M_2C and austenite and expanding. MC carbides are subsequently generated inside M_6C carbides or in contact with M_6C carbides. However, Chaus et al. [169] concluded that during decomposition, MC carbides mainly precipitated at the interface between the lamellar M_2C carbides and the matrix. It was emphasized that the dimension of MC carbides formed at the interface between the lamellar M_2C carbides and the matrix was significantly larger than the MC nucleated inside the M_6C carbides, which implies that significant coarsening of the decomposed carbides occurred. Nevertheless, these different phenomena suggest that the more fully the M_2C carbides are decomposed, the more uniform the carbides are distributed after thermal-mechanical processing (mainly involving hot forging and hot rolling), resulting in a substantial improvement in bending strength and impact toughness [38].

4.1.2. *Morphologies and distribution of carbides*

Generally, the resultant microstructure is distinctive of HSS parts manufactured by different AM processes. For instance, it is found that the microstructure of the HSS parts fabricated by PBF and DED processes is made of equiaxed crystal and columnar dendritic structure, while the microstructure of HSS parts manufactured through the SF method is mainly

equiaxed grain. Although there are remarkable differences in dendrite arm spacing or cell size compared with conventional processes, it is noteworthy that the interdendritic (or intercellular) network of eutectic carbides, which is more or less continuous, is still a significant feature of the HSS microstructure. This phenomenon reveals the considerable effect of eutectic carbide shape and distribution on the microstructure of HSS produced by AM. Especially, the most prevailing eutectic carbides are MC, M_2C and M_6C. MC eutectic carbide in HSS is rich in vanadium element, and the higher the content of vanadium and carbon, MC is favored to M_2C or M_6C. MC carbide has an isolated massive or petallike shape with an FCC structure, and its microhardness is about 3000 HV [157]. Several variables impact the shape of M_2C eutectic carbide, including chemical composition, cooling rate, and modest addition of particular components [170–173]. Eutectic morphology is classified into two types: irregular and complicated regular. For irregularity, many researchers describe its shape as feathery, fanlike, lamellar and platelike [170,172,174]. For complex regular, it appears as lamellar and rod-like [172,173]. M_2C carbide has a hexagonal crystalline structure with a microhardness of 2000 HV [157]. As a metastable phase, it decomposes into MC and M_6C carbides during the subsequent high-temperature annealing process [175,176]. M_2C eutectic is favored to M_6C eutectic by increasing the Mo/W ratio. M_6C eutectic carbide is generally fishbone shaped with a ridgeline, which is significantly different from M_2C eutectic carbide. It has a complex FCC crystalline structure with a microhardness of 1500 HV [157]. In addition, the Cr element is easily enriched to form M_7C_3 and $M_{23}C_6$ carbides distributed in the martensite matrix, which resist oxidation under high-temperature wear conditions [177]. Because of the incorporation of Co, the matrix retains its strength even when subjected to high temperatures [178]. Therefore, in this section, the carbide characteristics of HSS parts fabricated by AM process are reviewed.

Extensive work has been carried out on the research of carbides in HSSs fabricated by AM. For instance, Mu et al. [179] investigated the microstructure characteristics of S390 HSS produced by SF. The results revealed the presence of two carbides, MC and M_6C, which are uniformly dispersed at the grain boundaries and inside the grains. By contrast, the carbide precipitation behavior of S390 HSS processed by EBM was characterized [32]. It was found that eutectic carbide types are MC and M_2C, and the regional energy input affected their relative proportions in the as-EBM microstructure. According to Xu et al. [180], the composite carbides of MC and Mo were distributed within the grains whereas the MC carbides of CPM9V HSS deposited by SF were mostly distributed at the grain boundaries. Especially, as the most prevailing M2 HSS, the microstructures fabricated by AM processes such as SLM [62,63,181], SLS [53], DMD [75], and LC [34,35,88] are discussed. As expected, the carbide types include MC, M_2C, and M_6C, which is compatible with the discovery of A30 HSS deposited by SF [103]. Meanwhile, as mentioned earlier, a uniform carbide dendritic network was still observed, and different carbide morphologies were pertinent to the solidification cooling rate. Moreover, Yu et al. [90] studied M3 HSS billets produced by SF with the addition of niobium content. It was found that the carbides in M3 HSS were composed of MC and M_2C, while M_6C appeared in M3 HSS with niobium. Niobium was thought to have the capacity to alter the principal carbide type and enhance the thermal stability of the microstructure of M3 HSS following heat treatment. Shim et al. [82] comparatively analyzed the evolution of carbides in the microstructure of DED-fabricated M4 HSS before and after heat treatment. It can be observed in the as-deposited layer composed of cellular dendrites, retained austenite and martensite, as shown in Fig. 17(a). As evidenced in Fig. 17(b), the XRD pattern showed that the as-deposited layer included a significant amount of martensite and M_2C carbides. Afterwards, the microstructure of the quenched and tempered M4 HSS was shown in Fig. 17(c). It has been shown that the deposition zone results in the development of tempered martensite, which contains tiny spherical carbide particles. As indicated in Fig. 17(d), the volume percentage of martensite in the deposited zone was much lower than that of the unheated M4 HSS, and more carbides developed in relation to MC and M_6C as a result of the decomposition of M_2C. By contrast, the microstructure of deposited M4 HSS after direct tempering was characterized, as shown in Fig. 17(e). As can be observed, the equiaxed dendritic structures were maintained even though more residual austenite was dispersed along the grain boundaries in comparison to the untreated M4 HSS specimen. The types of carbides remained the same as in Fig. 17(d), as displayed in Fig. 17(f). Carbides precipitated at grain boundaries were bigger in size than those seen in Fig. 17(a and c), and the undissolved particles typically had sizes on the order of a few microns. The primary source of strength and hardness came from the carbides that were generated during tempering.

To further elucidate the precipitation characteristics of secondary carbides, Wang et al. [102,105,108,182] discussed the precipitation behavior of secondary carbides in M3:2 and M3 HSSs manufactured by SF with 2% Nb. The secondary carbides were identified in detail using a high-resolution transmission electron microscope (HRTEM), as illustrated in Fig. 18. Needle-like secondary M_2C are shown in Fig. 18(a). These secondary M_2C carbides also appeared in M3:2 HSS with 2% Nb, with a diameter of about 1.5 nm (Fig. 18(b)). By contrast, there is no significant difference in size due to the strong thermal stability of secondary carbides. To further discuss the orientation relationship between the secondary carbide and M3:2 HSS with a 2% Nb matrix, the fast Fourier transformation (FFT) image of M_2C carbide marked with a rectangle is shown in Fig. 18(c). Correspondingly, the inverse fast Fourier transformation (IFFT) image (Fig. 18(d)) displays that the interplanar spacing of $(110)_\alpha$ is 0.2022 nm. While inserted FFT and IFFT images in Fig. 18(e) are characterized by the secondary MC carbides in the M3:2 HSS with 2% Nb matrix with a size of 7–8 nm. The results declared that the addition of 2% Nb reduces the primary austenite grain size. While Nb appears in MC carbides, contributes less to eutectic M_6C carbides. The coordinated precipitation of MC and M_2C carbides is responsible for the peak strengthening. Under the same tempering conditions, 2% Nb HSS has excellent tempering performance due to the presence of high-density nano-scale M_2C precipitates. It was claimed that niobium substitution could provide good solid solubility of vanadium and molybdenum

and that considerable amounts of nano-scale MC and M_2C secondary carbides predominate in 2% Nb HSS for achieving better hardness and outstanding strength.

In summary, carbide type and shape are mostly determined by the chemical composition of HSS and the rate of cooling during the manufacturing process [162]. However, it is not universal for specific carbides, such as M_6C. The chemical composition and cooling rate have little effect on the morphology of M_6C eutectic carbide, however higher cooling rates minimize the distance between platelets [172].

4.2. *Defect formation mechanism*

4.2.1. *Porosity*

Depending on the process settings and alloy types, porosity is a relatively prevalent defect in HSSs manufactured by AM [26,183], which is particularly harmful to the mechanical characteristics of HSSs [184]. Three possible porosity formation mechanisms were proposed: gas porosity, interstitial porosity, and solidification shrinkage [140]. For example, porosity appears in DED components, which may be ascribed to inadequate solidification processes or the existence of entrapped gas and debris. Porosity is caused by inadequate efficient fusion between succeeding layers, which is promoted by insufficient laser power [185]. Un-melted particles also affect porosity, which may occur in the first/second deposited layer next to the substrate owing to a considerable quantity of heat transmitted to the substrate during the early stage of DED. Moreover, it has been observed that the porosity of SF-deposited HSS in the bottom and top surface regions could reach 20% [136,183,186,187].

During PBF processing, complex interactions between the particles in the powder bed and the energy beam occur, resulting in microstructural defects such as pores, spheroidization and vaporization effects during the accumulation process [188,189]. Geenen et al. [26] studied the density of M3:2 HSS processed by SLM at a preheating temperature of 300 °C. The results showed that irregular pores occupied a larger area of the SLM sample due to insufficient melting at a spot distance of 40 μm and an exposure time of 60 μs, as shown in Fig. 19(a). In contrast, at the spot distance of 20 μm combined with an exposure time of 110 μs, small, regular round pores were observed in Fig. 19(b). These pores, with a diameter of about 35 μm, are concentrated due to the reduced solubility of argon and other gases in the molten metal during the solidification process. It can be found that as the exposure time increases, the porosity can be minimized. When high melt viscosity and melt-bath dynamics are combined, gas cannot escape because of a high solidification rate, which leads to the formation of pores [190]. Especially, as described in 2.1.3, the porosity of HSSs fabricated by DMLS is the most extraordinary among the processes listed. Since the sinterability of HSS is greatly affected by the sintering atmosphere, Simchi et al. [58] studied the effect of the total porosity of M2 HSS manufactured by DMLS under argon and nitrogen atmospheres, as seen in Fig. 19(c and d). It was discovered that the laser scanning speed and the amount of graphite addition had an impact on the sintering atmosphere. After sintering in a nitrogen atmosphere, the overall porosity of M2 HSS steadily increased. In contrast, after sintering under argon, the porosity decreased slightly at the scan rate $v < 100$ mm/s while it increased at higher scan rates. Similarly, the porosity of M2 HSS with 0.4 wt% graphite exhibited a rapid increase at scan rate $v > 100$ mm/s regardless of atmospheres. According to Fig. 19(c and d), the M2 HSS produced by the DMLS process appears to be denser in argon than in a nitrogen environment. Furthermore, even though porosity is decreased at a lower scan rate, healthy parts cannot be made owing to sintered layer delamination and component breaking. The higher porosity produced by DMLS in a nitrogen environment might be ascribed to nitrogen dissolving in the melt during the DMLS process. Meanwhile, the dissolution of nitrogen content affects the surface tension of the melt, and variations in the melt's surface tension and viscosity may dominate Marangoni convection and further impact the attainable density [191]. Therefore, it can be found that the porosity of HSS components is related to the protective medium and process parameters. Generally, for the HSS parts manufactured by PBF and DED processes, the subsequent thermo-mechanical deformation process is rarely carried out due to the size limitation and the complexity of the shape. To manufacture HSS components with a high density, the process parameters must be optimized. Regarding the HSS manufactured by SF process, a small amount of porosity is allowed, and a completely dense part can be obtained due to thermo-mechanical deformation. In terms of reducing porosity, HSS parts fabricated by SF process have higher flexibility compared to HSS manufactured by PBF and DED processes.

4.2.2. *Cracks and delamination*

HSSs with high carbon content (>1.3 mass-%) have a considerable impact on the formability of AM and alloy weldability regardless of PBF or DED-based AM process, particularly the presence of hard and brittle martensite and carbides linked to internal stress in the component, which causes cracks to form [31]. There are two sorts of cracks: hot cracks and cold cracks [192]. Hot cracking encompasses the solidification as well as the liquification of the material to be fractured. Thermal strain caused by solid shrinkage breaks the liquid layer at the interdendritic region (or grain boundary), resulting in solidification fractures. Liquefaction cracking develops when thermal stresses are applied to the liquid layer created by the remelting of low melting point materials. Solute segregation creates the liquid film at the interdendritic area (also known as the grain boundary). When DED is rapidly cooled, non-equilibrium solidification takes place, and more alloy is present in the liquid phase. As a result, solute segregation occurs at the grain boundary, or interdendritic region, and the development of eutectic carbides makes materials more susceptible to heat cracking [193]. The driving force for the formation of cold cracks may be related to the residual stress generated during the deposition process. From a macroscopic perspective, residual stress might be created by the restricted shrinking of the liquid molten pool induced by the substrate's restraining effect during solidification [167]. At the microscopic level, residual stress may be the result of local internal strain brought about during solidification by variations in the atomic packing density and thermal expansion coefficient between martensite and austenite [194–196]. As a consequence, a heated crack's tip may geometrically concentrate

the accumulated residual stress with a high-stress concentration factor. Cold cracks may develop as a result of stress concentration once the brittle martensite phase is present close to the fracture tip [197]. Therefore, residual stress has to be released and reduced in order to prevent cold cracking.

In their investigation of the (Fe–1C–2.6Mo–W–V) HSS fabricated by the DED process, Park et al. [167] argued that eutectic carbides enhanced the sensitivity to thermal cracking and induced solidification cracking and liquation cracking in the interdendritic area. There is a possibility that the deposited layer will experience cold cracking of the α′-martensite at the hot crack tip as a result of the tensional residual stress in the layer. As shown in Fig. 20(a), many cracks appeared in the deposited layers parallel to the build direction, extending from the bottom to the top layer or becoming entrapped between layers. Many cracks in the cross-sectional were subjected to an EBSD analysis, which revealed certain cracks propagating along high-angle grain boundaries, as shown in Fig. 20(b–e), which were recognized as hot cracks with yellow pathways. However, as displayed in Fig. 20(c),

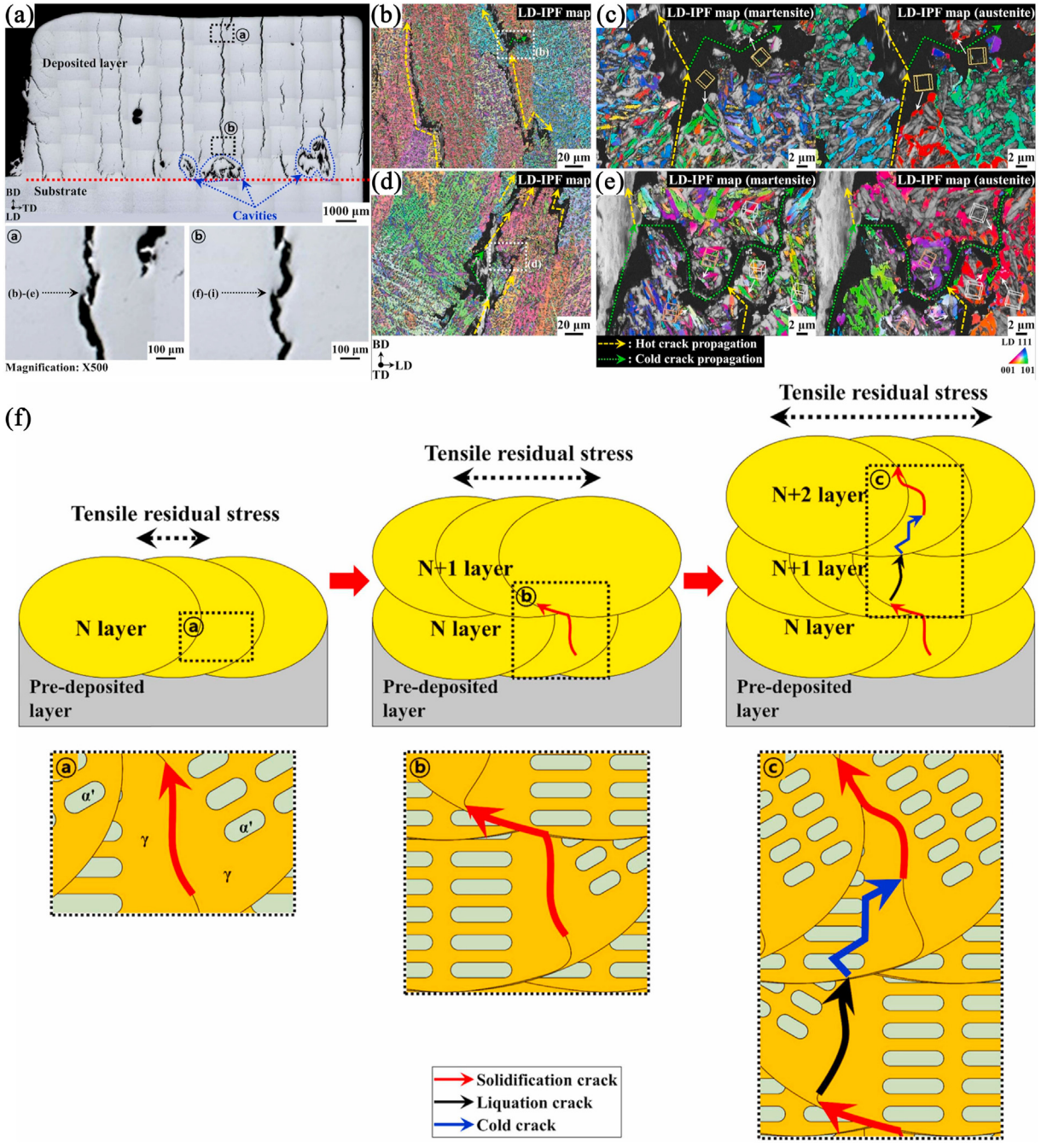

Fig. 20 – Microstructure and proposed mechanism of the crack initiation and propagation process in the deposited layers of DED fabricated (Fe–1C–2.6Mo–W–V) HSS: (a) optical microscopy images of the crack distribution and (b–e) cross-sectional image of crack propagation routes in (b and c), and (d)–(e). (f) proposed mechanism showing the schematic diagram of crack initiation and growth [167].

certain cracks propagated into the interior of grains with comparable crystallographic orientations and were referred to as green routes. These transgranular fractures are indicative of cold cracks. As a result, cold cracks are formed and propagated by residual stress concentration at the hot crack tip, and macroscopic crack propagation may be launched by joining the separated hot cracks, as seen in Fig. 20(f). This may be accomplished effectively by heating the baseplate to reduce macroscopic residual stresses, by modifying process variables, or by appropriately optimizing the alloy design. Meanwhile, PBF processing in the austenitic regime would result in a reduction of residual stress in the material [198]. During M4 HSS manufacturing, Shim et al. [36] found that a slower cooling rate decreased thermal stress generated at the deposited layer-substrate interface, resulting in less crack formation. The effect of varying the preheating temperature on the density and crack tendency of PBF-fabricated M2 HSS parts was investigated [65]. It was found that a preheat temperature of 200 °C enabled the fabrication of crack-free dense components (99.8%). Therefore, a lower tendency to crack is shown by applying the preheating temperature. Since a preheating system may minimize cracking, it is reasonable to assume that martensite formation can be prevented by preheating above the martensite initiation temperature [43].

Moreover, Saewe et al. [31] discussed the effect of optimizing alloy compositions on the processability of HS6-5-3-8 HSS produced by the SLM. Although the additional carbon boosted the retained austenite in the microstructure, it was thought to accelerate the development of embrittlement fractures and lower the processability of HS6-5-3-8. This phenomenon indicates that increasing the carbon content leads to an obvious cracking trend in HSS components, which may be explained by the higher carbide precipitation caused by the higher carbon content. These carbides are significant to promote crack initiation, resulting in stress concentration at the incoherent precipitation. This research lays the foundation for the alloy design of AM-processed HSS parts. In addition to carbon, further attempts should be made to add other austenite-stabilizing alloying elements to HSS without embrittlement due to carbide formation in the future.

Delamination, on the other hand, refers to the separation of two or more adjacent layers within a component as a result of incomplete melting between layers [199]. This macroscopic defect cannot be remedied by post-processing. High thermal gradients and different cooling rates generate different shrinkage and internal tension between the melting zone. When these tensions exceed the cohesion limit of the layer, the layer splits and forms gaps. Severe delamination and bending of the component boundary are caused by the existence of residual stress [200]. In addition, due to low scan speed and without preheating the baseplate, M2 HSS parts manufactured by SLM exhibited warpage, delamination, and baseplate separation [65], which is in accord with the research conclusions of Liu et al. [64]. In summary, the delamination phenomenon is common in HSS parts fabricated by AM process. Small changes in the temperature field and stress field may lead to this defect. It is extremely effective to avoid the formation of delamination by optimizing the AM process parameters and strengthening the numerical simulation analysis.

5. Engineering performance of AM-fabricated HSS

5.1. *Residual stress*

It is common knowledge that residual stress may have a substantial effect on engineering materials, particularly in the fields of fatigue, fracture, corrosion, friction and wear [201]. The existence of residual stress in AM-processed components is principally caused by uneven temperature field distribution along the building direction of the component and thermal history [202,203]. During the AM process, the residual stress at the starting position of scanning is relatively small. As the height of deposited layers increases, the compressive residual stress adjacent to the substrate is relatively large [204] and gradually transforms into tensile residual stress [205]. Rahman et al. [37] introduced strain gauges to measure the residual stress of the LC-deposited HSS, and the results

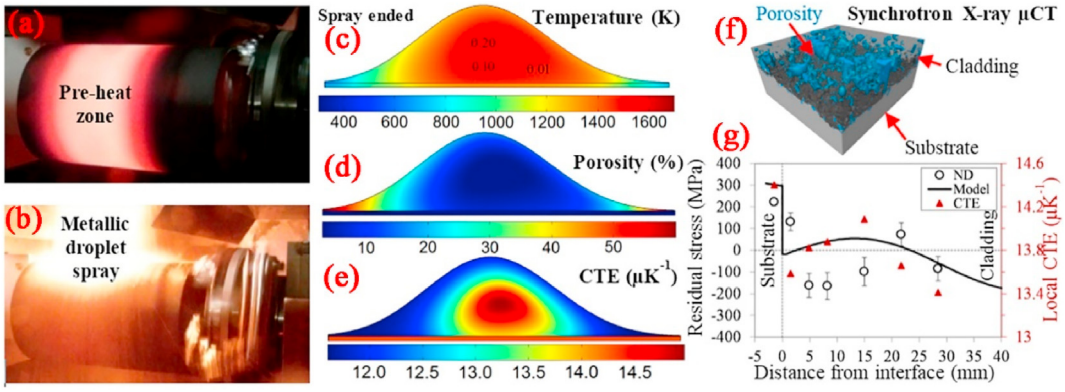

Fig. 21 – Photos of the (a) substrate preheated zone before spraying and (b) the metallic droplet spraying process. Simulated results of the (c) temperature distribution, (d) porosity distribution, and (e) thermal expansion coefficient distribution in the preheated clad pipe. (f) 3D rendering of the porosity (blue) and (g) residual hoop stress distribution and local thermal expansion coefficient along with the cladding-substrate interface of the clad tube [208,209].

demonstrated that there are compressive residual stresses from the top layer to the substrate. The reason for the compressive stress in the cladding is that during re-solidification, the cladding close to the interface shrinks significantly due to contact with the colder substrate, which encourages conduction. Moreover, it was reported that significant compressive stresses exist in the LC of HSS as a result of volume expansion caused by martensitic transformation [79,206].

By decreasing the local heat gradient, residual stress and distortion may be reduced as much as feasible for AM processes. This may be performed by optimizing and managing the process parameters, maintaining ideal molten pool morphology and size, pre-heating the substrate, and choosing an acceptable laser scanning pattern [202]. However, it is emphasizing the presence of residual stress is a double-edged sword for the fabrication and application of components. Generally speaking, residual stresses associated with the cooling of deposited parts can be a principal cause of premature failure of HSS made by AM [207]. By using finite element modeling, it can be seen, for instance, that the porosity of as-sprayed HSS has an impact on the magnitude of the residual stress, particularly when the critical threshold is surpassed

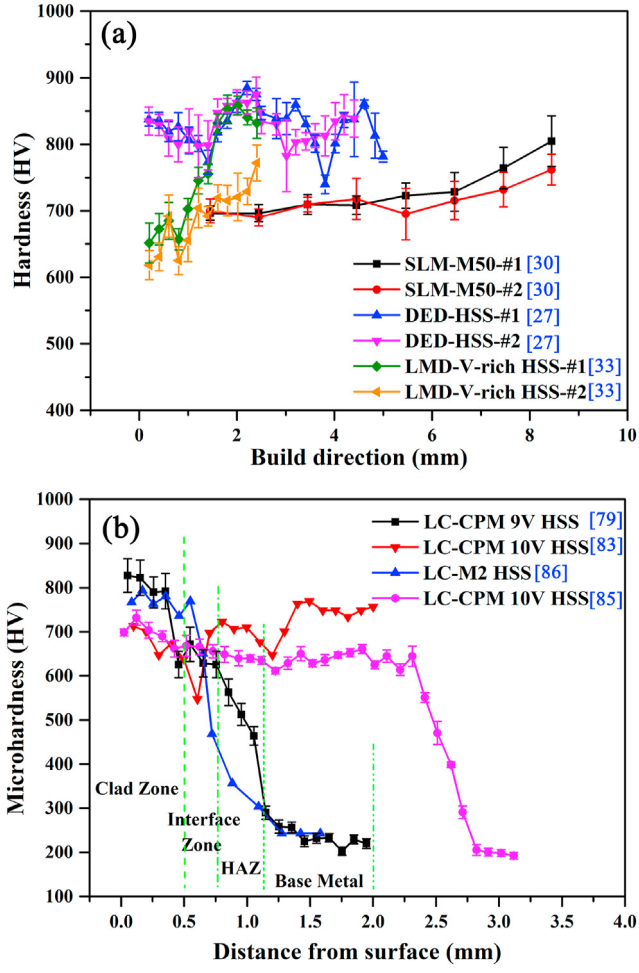

Fig. 22 – (a) Microhardness of different grades of HSS multilayer samples in the building direction and (b) cross-section microhardness profile for HSS coating.

[208]. To explore the link between porosity and residual stress distribution, Lee et al. [209] successfully utilized ASP30 and M2 HSSs to deposit composite pipes on mild steel utilizing the SF process, and systematically studied the evolution of microstructure and residual stress. To obtain a good bonding strength of the entire interface, the mild carbon steel substrate was immediately preheated before spraying, as seen in Fig. 21(a). Afterwards, the atomized metal droplets deposited in the spray cone were monitored in-situ in the preheating zone, see Fig. 21(b). Especially, the inherent relationship among the simulated average droplet deposition temperature, porosity and coefficient of thermal expansion (CTE) was established to improve the bonding stability of dissimilar steels, as shown in Fig. 21(c–e). Meanwhile, the experimental data on the porosity was obtained by synchrotron X-ray computed tomography, and the 3D rendering of the porosity (blue) is shown in Fig. 21(f). Moreover, simulation and neutron diffraction (ND) measurements of the residual hoop stress distribution on the cladding-substrate interface of the cladding tube were obtained, as displayed in Fig. 21(g). It can be seen that as the substrate preheating and spraying temperature increased, it was favorable to increase the cladding temperature to promote interface diffusion, reduce porosity and increase the proportion of retained austenite in the cladding. A larger temperature difference between adjacent deposited layers, which is known to increase porosity, was frequently the source of compressive stress in the porous zone. For the first time, the researchers discovered a link between porosity distribution and residual stress in a spray-formed preform. On the other side, the experimental results of LC-deposited CPM9V HSS on H13 tool steel revealed that normal compressive residual stress was formed in the cladding, which was desirable for repair applications due to hindering crack propagation [79].

5.2. *Hardness, strength, and impact toughness*

It is common knowledge that the mechanical performance of HSS strongly depends on chemical compositions, microstructure, process conditions and heat treatment procedures [161,210]. Generally, the mechanical properties of AM-processed HSS components with different compositions are unique. For a specific alloy composition, the evaluation of mechanical properties is particularly significant. To explore the relationship between alloy composition and mechanical properties, this section reviews the research progress of AM technology for fabricating HSS components in terms of hardness, strength and impact toughness.

Generally, the mechanical properties of the parts fabricated by AM process in terms of hardness and strength are higher than forged and CC materials due to the high dislocation density present in AM-processed materials. Large amounts of experimental data reveal that the mechanical characteristics of SF-deposited HSS components in terms of hardness, bending strength, and impact toughness are superior or equivalent to those of PM and ESR-processed HSSs of the same composition. The mechanical properties of M2 HSS components fabricated by three manufacturing processes were investigated [211]. The findings showed that under the same heat treatment procedure, the tempered hardness of SF

deposited M2 HSS was equivalent to that of M2 HSS fabricated by the ESR process, and bending strength was similar to that of M2 HSS processed by the PM process. A similar investigation was also conducted by Ernst et al. [212]. Compared with ESR-processed HSS, the bending strength and impact toughness of 6W–5Mo–4V–4Cr HSS produced by SF were increased by 40% and 18% after the identical hot forging and heat treatment procedures, respectively. Rickinson et al. [213] investigated the mechanical properties of M2 and M15 HSSs fabricated by SF under various deformation and heat treatment conditions. It was concluded that the hardness of SF-processed M2 and M15 HSSs was always higher than that of CC-processed HSSs. Meanwhile, Mesquita et al. [17,25] systematically discussed the effects of SF, CC and PM processes on the mechanical properties of M3:2 HSS. Experimental results showed that the transverse toughness was larger than that of CC-processed M3:2 HSS, and its isotropy was 87%. Compared with the M3:2 HSS fabricated by PM, the size of the carbides in M3:2 HSS fabricated by SF was larger and the distribution was relatively uneven, resulting in lower bending strength and isotropy.

As mentioned earlier, as a special category of tool steel, the significance of alloy composition is self-evident. For instance, carbon and vanadium are two essential constituents in HSS that have a substantial impact on the material's properties and the product's service life. To further improve overall performance, high-carbon and high-vanadium (HCHV) HSSs are designed and developed by modifying the carbon and vanadium content [214–218]. CPM 9V, CPM 10V, CPM 15V and M4 HSSs were deposited on carbon steel substrates utilizing the LC process, respectively [84]. It was found that as-clad CPM 15V HSS exhibited the highest hardness of about 66 HRC, and the lower hardness of CPM 9V HSS was about 48 HRC due to the lower volume fraction of the hard phase. As a result, it can be inferred that the difference in vanadium content directly determines the volume fraction of hard MC carbide generated in the martensite. However, Tekumalla et al. [219] characterized two high vanadium HSSs (10V and 15V) fabricated using DED, exhibiting the excellent hardness of 950 HV and 850 HV. The increased hardness of 10V HSS is due to the presence of more martensite, which is aided by the lower carbon content compared to 15V HSS, where they discovered a larger percentage of softer and more stable austenite in the matrix. Kattire et al. [79] investigated the microhardness evolution of CPM 9V HSS manufactured by LC. It was found that the top layer of the cladding reached the maximum hardness, with an average value of 800 HV. Leunda et al. [83] characterized the average microhardness of CPM 10V HSS manufactured by the LC process was 700 HV, showing that changes in carbide distribution in the remelting zone led to uneven hardness along with the cladding layer, as displayed in Fig. 22. Meanwhile, the impact of variable process factors on the mechanical qualities should not be underestimated. DED fabrication of vanadium-rich HSS [33], HC-HSSs [27] and (W–Mo–Cr–V–Co) HSS [37] was studied under different process parameters by Rahman et al.. As evidenced in Fig. 22, increasing laser scanning speed resulted in an increase in microhardness from 760 HV to 835 HV. However, sequential laser deposition could also result in a reduction in the microhardness of the pre-deposited layer due to the formation of softer martensite and coarse carbide precipitation [220]. After several cladding passes, it was found that the microhardness gradually decreased from 795 HV to 570 HV. The reduction in hardness could be ascribed to martensite tempering during continuous cladding [37]. In terms of strength-toughness, the tensile strength of (W–Mo–Cr–V–Co) HSS could reach 889 ± 20 MPa, but the

Table 6 – Research results on the mechanical properties of HSSs fabricated by AM processes.

Grade	Fabrication process	Hardness	Bending strength (MPa)	Impact toughness (J)	Refs
M2 (Fe-0.91C-4.36Cr-5.7W-5.27Mo-2.12V)	SF	65.8 HRC			[208]
M2 (Fe-0.9C–4Cr-6.4W–5Mo-1.9V)	SF	60.8–65.4 HRC			[109]
M2 (Fe-0.86C-1.25Cr-6.32W-5.23Mo-1.97V)	DMLS	420-1020 HV			[58]
M2 (Fe-0.99C-3.93Cr-6.32W-5.03Mo-1.78V)	LC	~830 HV			[76]
M3:2 (Fe-1.3C-4.6Cr-6.2W-5.1Mo-2.8V)	SF	65-66 HRC	3163–3514	21–25	[40]
M3:2 (Fe-1.3C-4.2Cr-6.3W–5Mo–3V)	SF	62.1–66 HRC			[109]
M3:2 (Fe-1.29C-3.9Cr-6.2W-4.8Mo–3V)	SLM	940 HV			[26]
M3:2 (Fe-1.14C-4.04Cr-5.86W-4.91Mo-2.94V)	SF	63.4–65 HRC	2133–2385		[25]
M3:2 (Fe-1.14C-4.04Cr-5.86W-4.91Mo-2.94V)	SF		2150–2471		[17]
M42 (Fe-1.15C-4.1Cr-1.6W-9.6Mo-1.16V-8.1Co)	SF	65.1–68.8 HRC			[225]
HS6-5-3-8 (Fe-1.23C-3.8Cr-5.9W-4.7Mo-2.7V–8Co)	SLM	650 ± 37 HV			[31]
S390 (Fe-1.64C–4Cr-10.12W–2Mo-4.97V-7.86Co)	EBM	73.1 HRC	3012 ± 34		[32]
T15 (Fe-1.6C-4.11Cr-12.1W-0.12Mo–5V-4.62Co)	SF		4675	26.86	[104]
HC-HSS (Fe–2C–5Cr–6W–6Mo–5V)	DED	800-900 HV			[27]
V-rich HSS (Fe–2C-5.2Cr-0.3W-1.2Mo–10V)	LMD	760-835 HV			[33]
HSS-L1 (Fe-1.4C-4.3Cr–5W–5Mo–4V)	LC	570-795 HV			[37]
HSS (Fe-1.35C-4.3Cr-5.6W-4.64Mo-4.1V)	LC	741-761 HV			[81]
ESP4 (Fe-1.29C-3.97Cr-5.93W-5.06Mo-4.23V)	SF	62.2–64.2 HRC	4962	48.9	[212]
HS6-5-2C (Fe-0.92C-3.77Cr-6.07W-4.78Mo-1.74V)	SF	64.7 HRC		11.8–16.7	[106]
X153CrMoV12 (Fe-1.54C-11.7Cr-0.15W-0.75Mo-0.94V)	SF	62.8 HRC		11.3–21	[106]

plastic strain was only 2.5%, which indicated that the fracture mode was brittle due to the presence of martensite and hard carbides.

Moreover, the effects of heat treatment procedures on the mechanical behaviors in terms of hardness, strength and toughness of HSS fabricated by AM have been extensively investigated. A series of studies have been carried out on SF deposition of M42 HSS [221], M3:2 HSS [40] and T15 HSS [104,222], DED fabrication of M4 HSS [223,224], D2 HSS [87] and HVHSS [85], SLM fabrication of M2 HSS [63] and M50 HSS [61], as well as EBM deposition of S390 HSS [32]. As expected, appropriate heat treatment procedures have significantly improved the mechanical properties of AM-processed HSSs. The detailed research results on the mechanical properties of HSSs made by AM processes are listed in Table 6. However, the experimental findings of M4 HSS manufactured by the DED process revealed that the heat treatment procedure decreased microhardness, which was ascribed to the alleviated residual stress and the reduction in carbon concentration in the martensite after tempering [82].

In conclusion, because of the many variables involved, it is difficult to directly compare and assess the mechanical characteristics of HSS made using AM techniques. Taking the PBF process to fabricate HSS as an example, the thermal history, structure, and properties of the HSS will vary depending on the laser power, scanning speed, laser spot size, and hatch spacing. Even if these values stay constant across builds, the laser scanning approach will impact the thermal history. The scanning strategy is determined by the positioning of the components on the substrate and the other components constructed during the same PBF build [120]. Therefore, even if the processing parameters remain unchanged during the study, the thermal history within the HSS component will be determined by the geometry of the component and the geometry of the test sample. This indicates that the temperature history, microstructure, and mechanical characteristics of the components will vary when specimens are collected from various locations. Lastly, the dimension and shape of the specimens may be the primary determinants of the mechanical characteristics, since the grain size of PBF-produced components varies substantially. Similarly, the mechanical characteristics of HSSs made by DED and MJ processes are influenced by a multitude of process factors. Therefore, to deepen the comprehensive understanding of AM processing, microstructure and mechanical properties, future research must describe the processing parameters and AM geometry, and extract the specimen geometry when reporting mechanical properties.

5.3. *Tribological behaviors*

HSSs are widely employed in harsh working conditions due to their unique microstructure endowed with excellent mechanical properties and enhanced tribological behavior [7,226]. However, with the development of complex application conditions, HSS as a wear-resistant component also faces many challenges. For example, the development of wear-induced defects on the surface of milling rolls made of HSS has been a great concern in the steel rolling process and affects their service lives [227–229]. These defects may act as the crack-initiation sites during the cyclic thermal shock and rolling process, leading to the failure of the roller products.

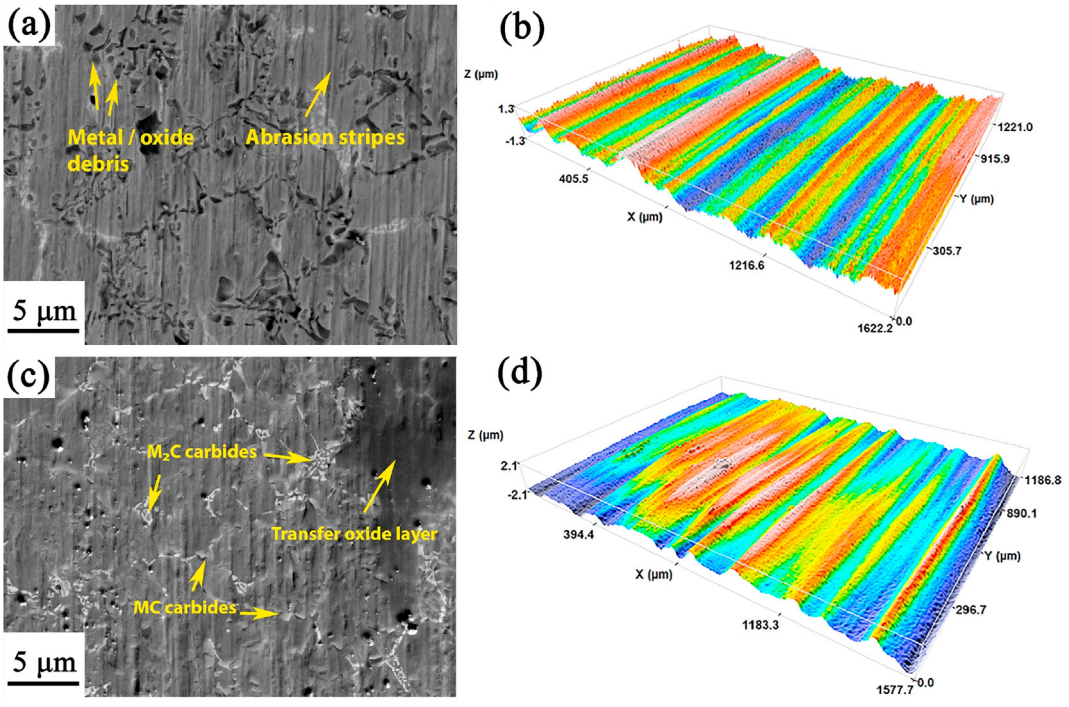

Fig. 23 – (a) SEM image of the worn surface of high-carbon HSSs, (a) high-carbon HSS without tungsten element. (b) Surface morphology profile of high-carbon HSS without tungsten element. (c) SEM images of the worn surface of high-carbon HSS with high tungsten content. (d) Surface morphology profile of the worn surface of high-carbon HSS with high tungsten content [27].

Considering the unique microstructure of metals fabricated by different AM processes, it is significant to understand the tribological behavior, as well as the associated failure mechanism of AM-manufactured HSSs [230].

Wang et al. [84] characterized the tribological behavior of CPM 9V, CPM 10V, CPM 15V and M4 HSSs fabricated by the LC process. It was suggested that hardness cannot directly assess the wear resistance of HSSs, but depends on the matrix microstructure and the characteristics of dispersed carbides. The tribological behaviors of three LC-processed HSSs were compared and discussed in detail by Hashemi et al. [81]. The results showed that, compared with softer M_2C carbides, the harder vanadium-rich MC carbides have better wear resistance. In terms of shape differences, clover-shaped primary carbides were more wear-resistant than angular primary carbides because of better geometric anchoring. In summary, hard phases are effective against abrasive wear if the size, morphology, hardness, and embedding of the hard phases into the metal matrix are sufficient. The LC-deposited M2 HSS was used to improve the wear resistance of parts due to the abundant carbides network effectively supporting the applied load [86]. The previous studies showed that the type and shape of carbides are critical to the wear resistance of HSS. Meanwhile, it was reported that compressive stress significantly improved wear resistance [231]. Afterwards, Rahman et al. [27,33,78] carried out a series of high-temperature (T = 500 °C) friction investigations through pin-on-disc experiments on LMD-processed vanadium-rich HSS and LC-processed HSS. Experimental results suggested that MC carbides provided load-bearing capacity during wear. In the case of extensive support, an in-situ oxide layer is formed, which can support mechanical loads other than carbides [232]. Nevertheless, when in contact with the tough oxide layer on the countertop, it is challenging to keep the fine carbides stable at high temperatures. At T = 500 °C, angular MC carbides and discontinuous M_2C carbide networks were readily peeled off due to weak anchoring and became wear debris entrenched in the matrix surface. The SEM images and surface roughness plots of the worn surface of two high-carbon HSSs after the friction test at T = 500 °C were presented in Fig. 23. Abrasive stripes can be discovered on the worn surface of high-carbon HSS without tungsten elements, and metal oxide debris was incorporated into the matrix, as shown in Fig. 23(a). The estimated surface roughness was about 0.35–0.45 μm from Fig. 23(b). The worn surface of high-carbon HSS with a high tungsten concentration indicated the existence of an all-over thin oxide layer. Compared with M_2C carbides, it was found that MC carbides at the grain boundary were partially oxidized, as shown in Fig. 23(c). The corresponding surface roughness was also approximately 0.35–0.45 μm in Fig. 23(d). It can be concluded that the wear of both HSSs at 500 °C demonstrates inhomogeneous oxidation, where the oxidation rate is determined by the carbide distribution [233]. As mentioned earlier, MC carbides are strongly susceptible to oxidation, but M_2C and $M_7C_3/M_{23}C_6$ carbides are resistant to oxidation [177]. Nielsen et al. [234] claimed that the oxide layer acts as a protective layer to a certain extent, reducing the strength of contact stress and surface wear. It

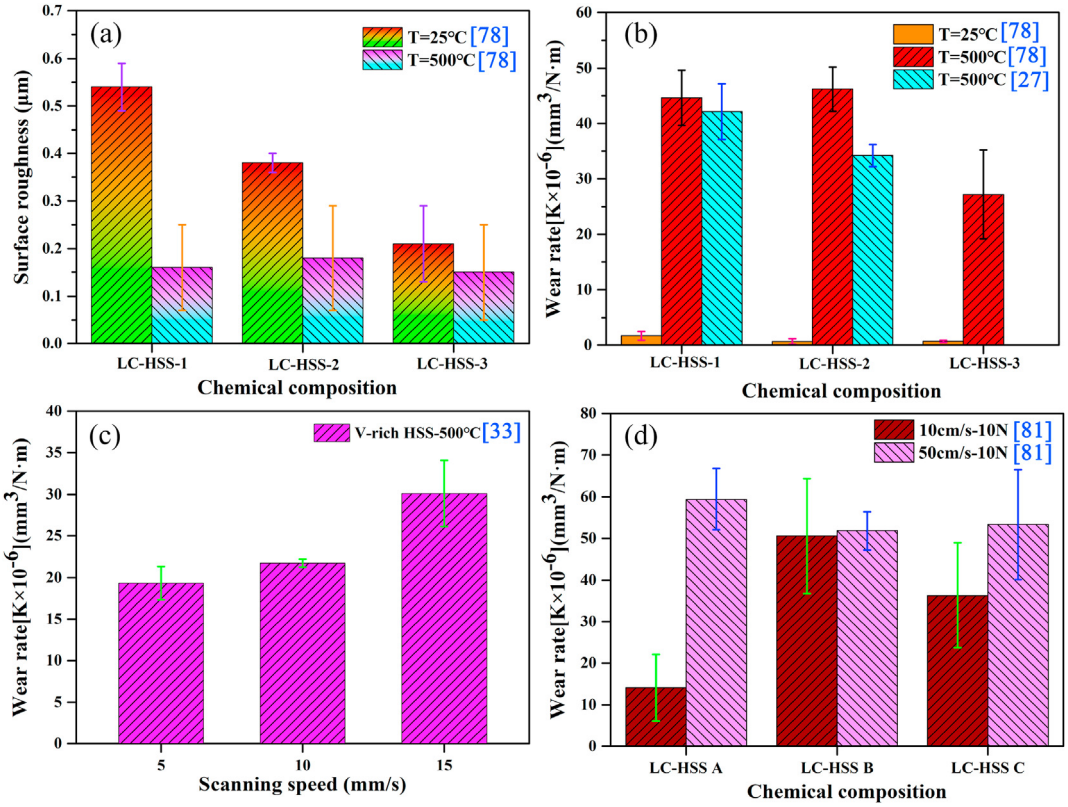

Fig. 24 – (a) Surface roughness of the HSS samples at T = 25 °C and 500 °C, (b) wear rates of HSS after wear test at T = 25 °C and 500 °C, (c) wear rate evolution of vanadium-rich HSS at T = 500 °C with laser scanning speed, and (d) variation of wear rates of high-carbon HSS at T = 25 °C with different sliding speeds.

was evidenced that high-temperature wear mechanisms include abrasive, adhesion and oxidative wear, with the latter dominating.

To further estimate the tribological behavior of HSS after wear testing, the surface roughness and wear rate were characterized by different grades of HSS, as depicted in Fig. 23. Interestingly, as shown in Fig. 24(a), a higher surface roughness (≈0.21–0.54 μm) is observed after room temperature wear tests compared to after high-temperature wear tests to form stable contacts and oxide films, resulting in low surface roughness (≈0.15–0.18 μm). However, in contrast, it is found that the wear rate after the high-temperature test is much higher than that after the room-temperature friction test, as displayed in Fig. 24(b). It is worth emphasizing that the wear rate at $T = 500$ °C cannot be correlated with the wear rate at $T = 25$ °C. Due to material thermal softening at high temperatures and the oxidation of worn surfaces, high-temperature tribological examinations are very complicated [232]. The results from Fig. 24(a and b) indicate that temperature significantly affects the evolution of surface roughness and wear rate of HSS after friction testing. On the other side, the process parameters and the experimental conditions of the friction test also have obvious effects on the wear rate of HSS, as depicted in Fig. 24(c and d). For the LMD-processed V-rich HSS, the cooling capacity is reduced and the carbide refinement in the matrix is suppressed, resulting in increased wear rates, as seen in Fig. 24(c). MC carbides, on the other hand, altered their morphology from square and round to angular and rod-like at a faster scan speed of 15 mm/s, which was observed to be less efficient against abrasive wear [81]. Fig. 24(d) shows that at higher sliding speeds, the wear rate of HSS increases. Wear testing revealed oxide formation at both sliding speeds. The oxide layer's thickness is steadily grown until it reaches a critical amount where internal stress may cause the oxide layer to fragmentize [235]. Therefore, the tribological behaviors of HSS are affected by the synergy of various factors.

Moreover, Xiao et al. [77] studied the tribological behaviors of H13/W–Mo–V HSS composites fabricated by LMD at various temperatures. It was found that the increase of W–Mo–V HSS content exhibited strong wear resistance at $T = 25$ °C, while the oxide film formed at $T = 450$ °C weakened the wear. Tarasov et al. [236] established the relationship between the wear behavior and microstructure of M2 HSS deposited by EBM on different friction pairs. The results indicated that the impact of friction pair on wear was pertinent to the formation of a mechanically mixed layer consisting of iron tungstate, carbide fragments and transferred metal.

Especially, among the HSS manufactured by AM, the HSS fabricated by the SF has realized industrial application due to its satisfactory performance in terms of wear resistance. Hanlon et al. [235,237] characterized the tribological behavior of high chromium HSS produced by SF. It was found that the wear volume at 20–650 °C was significantly smaller than the wear volume produced by the CC process. It was assumed that the shift in the distribution of eutectic carbides and the removal of macro-segregation contributed to the improvement in wear resistance. IKawa et al. [238] investigated the wear resistance of SF-deposited ultra-high-carbon HSS rolls, indicating that the service life was 2–3 times longer than that of CC rolls. Meanwhile, the high-temperature wear resistance of M3:2 HSS deposited by SF and PM processes was discussed

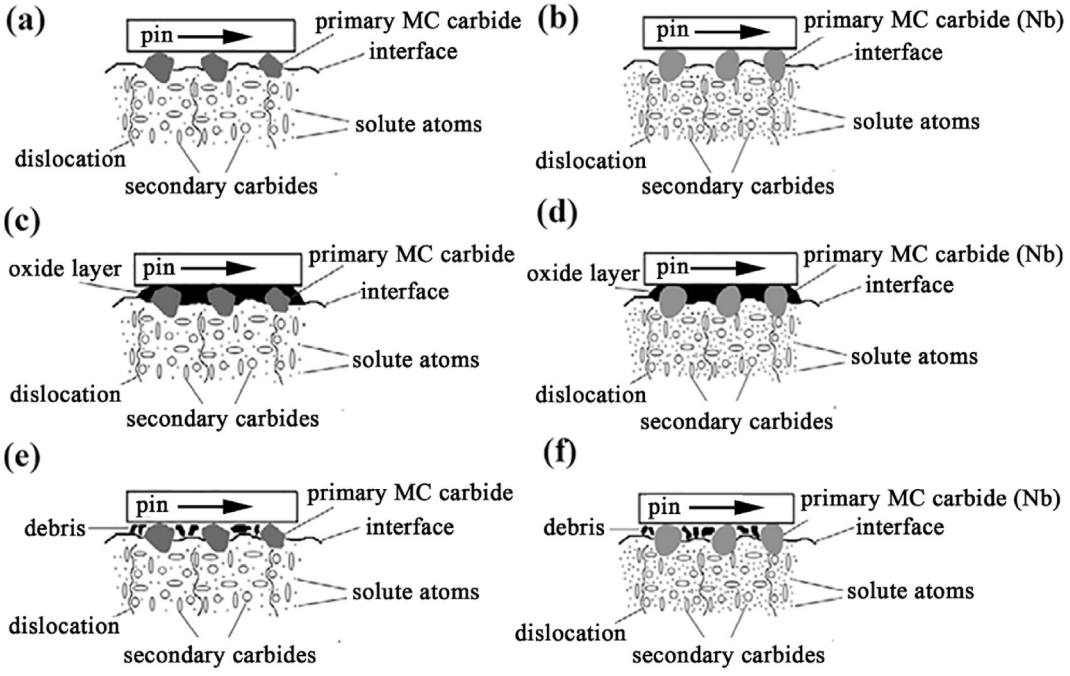

Fig. 25 – The wear mechanism of M3 and M3 with 2% Nb HSSs at elevated temperatures and different loads: (a) M3 HSS evaluated at lower temperatures and loads, (b) M3 (2% Nb) HSS, (c) oxide formation at high temperatures and loads, (d) oxide development in M3 (2% Nb) HSS, (e) MC carbides remain in the matrix, (f) Nb-containing MC carbides persist in the matrix [105].

[239]. At $T < 600$ °C, the specific wear rates of the HSS manufactured using SF and PM processes were hardly different from one another, while at $T = 600$ °C, SF-deposited HSS had a much lower specific wear rate than the PM process. It was found at each test temperature, M3:2 HSS fabricated by SF is unique, suggesting that the manufacturing route has a significant impact on wear performance due to the influence of carbide size distribution. Moreover, the effects of niobium addition on the microstructure and tribological behavior of SF-deposited M3:2 and M3 HSSs at various temperatures were discussed [105]. According to the research, the addition of niobium caused primary MC carbide to have a finer size and more uniform distribution, which significantly enhanced the tribological characteristics of M3:2 and M3 HSSs.

To further clarify the evolution of the tribological behavior of HSS, the wear mechanisms of spray-formed M3 HSS under different temperatures and applied loads were revealed, as shown in Fig. 25. At $T = 20$ °C, the presence of harder MC carbides leads to a reduced wear rate for HSS containing 2% Nb, as displayed in Fig. 25(a and b). As the temperature and applied load increase, the oxide layer gradually developed until it exceeds the critical oxide thickness, see Fig. 25(c and d). The wear mechanism preferred adhesive wear, with increased oxidative wear at $T = 300$ °C. A minor number of primary carbides may be extracted with the debris, while the majority of the carbides in Fig. 25(e and f) remained in the matrix and protruded from the interface. It can be found that the oxidative wear was most favorably formed at $T = 500$ °C. Therefore, the investigation of the wear mechanism of HSS is advantageous to give relevant information for extending the life of HSS applications owing to the severe cycle temperatures and loads under harsh working situations.

6. Challenges and future directions

6.1. *Current challenges*

Over the last several decades, significant development has been achieved in many aspects of state-of-the-art AM techniques. The next generation of AM facilities and processes is being driven by advancements in AM technology, characterization, and modeling. However, as the AM field develops, the use of AM for producing various classes of high-quality HSS components will rely heavily on solving several key obstacles. The following are some of the key obstacles that AM faces while manufacturing HSS.

(1) AM control: The time-invariant operating parameters will produce HSS components that are anisotropic or that fail during the manufacturing process. Real-time AM control must be devised and implemented to enable adaptive, time-varying operational parameters based on on-site monitoring feedback.
(2) AM efficiency: Most AM processes, such as PBF and DED processes are not highly efficient in fabricating HSS. Although the waste powder can be recycled, the deposition and energy efficiency should be improved to reduce the cost of the process.
(3) Defect formation and optimized process parameter determination: To get near-net form and totally dense components, it is essential to comprehend the ideal process parameters for a particular AM machine. Prior to building components, the appropriate process parameters should ideally be defined. The parameters are usually determined based on trial and error, even if the determined parameters may not be the optimal solution, resulting in increased time and manufacturing costs.
(4) Industry application: The dimension limitations of the manufactured parts weaken the broad applications. The challenge is to accomplish "laboratory to factory" and deliver AM procedures with high precision and repeatability that are suited for low- or large-volume manufacturing.
(5) Numerical modeling: Due to present limits in computing software and technology, it is difficult to correctly simulate all associated AM phenomena. The model should provide precise modeling of complicated forms, time-varying process parameters, molten pool morphology, and fluid dynamics/wetting behavior of molten pool fluids.
(6) Standards and regulations: As the AM process evolves, standards and regulations are absent to ensure AM components compliance. Certification must take into account post-AM processing such as heat treatment, as well as fault tolerance such as porosity. Once the certification of the parts produced by the AM process is completed, the standard for mechanical characterization is imminent.
(7) Development of new HSS alloys for AM processes: An essential concern is the development of corresponding HSS alloys for corresponding AM processes. Therefore, the formation process of the microstructure must be understood in detail. It is also necessary to determine to what degree these alloys can be heat treated to get the optimal qualities, resulting in the development of tailor-made HSS alloys for AM operations.

6.2. *Future directions outlook*

Due to the aforementioned obstacles, there is still a large knowledge gap in the literature regarding the relationship between process parameters, solidification behavior, microstructural development, and mechanical characteristics of AM-produced HSS. Only a greater knowledge of the underlying processing-structure-property linkages available with new AM technologies may close these gaps. An approach has been presented to handle the multitude of challenges using integrated computational materials and engineering [240], as illustrated in Fig. 26. This approach involves numerical modeling/microstructure regulation/processing control and monitoring strategies to enhance the understanding of different AM processes-structure-performance. Therefore, the authors believe that some potential research directions for AM fabricating HSSs include the following aspects in the future.

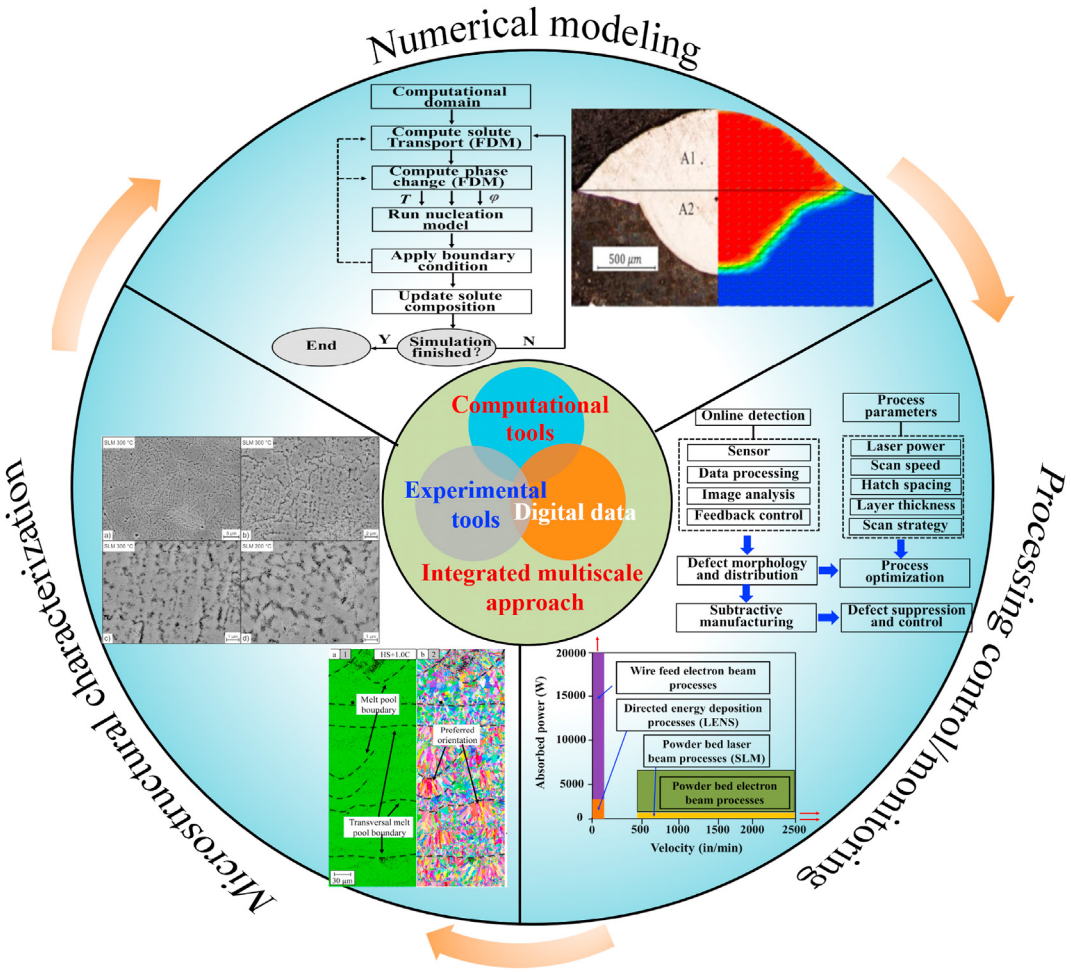

Fig. 26 – Integrated multiscale approach for the development of AM-processed HSSs for a wide range of applications [26,31,74,240].

(1) For AM control and efficiency areas, new innovative techniques of control should be created to accomplish the management of thermal history, allowing end-users to manage microstructures and the resulting homogeneity in real-time. In addition, it is worthwhile to investigate more suitable energy/deposition techniques to increase overall efficiency.

(2) It is necessary to replace the identification of the ideal AM process variables for the various grades of HSS materials with adaptive learning processes coupled with numerical simulation. To hasten AM machine/process learning, the material and procedure "genome" must be enabled.

(3) More study is needed to identify how the AM process parameters should vary as the number of parts or part dimensions rises to optimize the utilization of the substrate.

(4) More realistic/complex structures are being simulated and modeled using AM with the use of supercomputing capabilities or innovative new techniques. Modern solidification simulation methods must be used to represent the AM process.

(5) The microstructure and mechanical characteristics of AM-fabricated HSS components should be thoroughly investigated. With the help of advanced characterization approaches, such as synchrotron radiation small-angle scattering, X-ray imaging, X-ray micro-focused beam, and neutron diffraction techniques, to investigate the nano-precipitates, three-dimensional morphology, element distribution, and residual stress of HSS parts. Through the link between microstructure and mechanical properties, it is anticipated that a database of AM-processed HSSs' chemical compositions, fabrication processes, and performance characteristics may be established.

(6) Regarding the wear resistance of HSS components, it is not only pertinent to the microstructure characteristics, but also the oxide film plays a decisive role. It is necessary to strengthen the investigation of the formation mechanism and thickness control of the oxide film of AM-fabricated HSSs.

7. Summary and conclusions

Advanced manufacturing process demonstrates great potential and advantages in the fabrication of HSSs. However, it is still constrained by current issues such as part size,

formability quality, and optimized solutions. To better investigate the process, numerical modeling and in-situ monitoring are necessary to deepen the process understanding and optimization. The development and combination of these methods represent the current challenge to eradicate building errors, improve component quality, and accelerate material assessment and part testing. This work provides a complete overview of the recent advances and progress in state-of-the-art AM technology for fabricating different grades of HSS. Especially, the difficulties facing AM technology now and potential research routes for producing HSS components are presented. This review is expected to provide recommendations and insights for future AM process designs that will result in HSS components with outstanding mechanical characteristics and improved tribological performance for a wide range of applications.

Declaration of competing interest

The authors declare that they have no known competing financial interests or personal relationships that could have appeared to influence the work reported in this paper.

Acknowledgments

Bo Mao acknowledgments the funding support from the National Natural Science Foundation of China (Nos. 52101046) and Baowu Special Metallurgy Cooperation Limited. Jiao Zhang appreciates the funding support from the National Key Research and Development Program of China (No. 2020YFB0311200). Baode Sun thanks the funding support from the National Science Foundation of China (Nos. 51627802 and 51821001).

REFERENCES

[1] Fischmeister HF, Ozerskii AD, Olsson L. Solidification structure of gas-atomized high-speed steel powders. Powder Metall 1982;25:1–9.
[2] Fischmeister HF, Riedl R. Solidification of high-speed tool steels. Metall Mater Trans 1989;20:2133–48.
[3] Meurling F, Melander A, Tidesten M, Westin L. Influence of carbide and inclusion contents on the fatigue properties of high speed steels and tool steels. Int J Fatig 2001;23:215–24.
[4] Park JW, Lee HC, Lee S. Composition, microstructure, hardness, and wear properties of high-speed steel rolls. Metall Mater Trans 1999;30:399–409.
[5] Badisch E, Mitterer C. Abrasive wear of high speed steels: influence of abrasive particles and primary carbides on wear resistance. Tribol Int 2003;36:765–70.
[6] A SC, Dománková M. Microstructure and properties of M2 high-speed steel cast by the gravity and vacuum investment casting. Vacuum 2019;162:183–98.
[7] Fu H, Xiao Q, Xing JD. A study on the crack control of a high-speed steel roll fabricated by a centrifugal casting technique. Mater Sci Eng, A 2008;474:82–7.
[8] Zhou X, Fang F, Jiang JQ. A study on the microstructure of AISI M2 high speed steel manufactured by continuous casting. Trans Tech Publications; 2010. p. 1211–5.
[9] Halfa Hossam. Characterization of electroslag remelted super hard high speed tool steel containing niobium. Steel Res Int 2013;84:495–510.
[10] Ximin Z, Xin D, Zhouhua J, Tianyu Q, Chunxu L. New manufacture of high speed steel 90 mm billets by electroslag remelting withdrawing process. Iron Steel 2016;1:39–45.
[11] Luo YW, Guo HJ, Sun XL, Guo J, Wang F. Influence of tempering time on the microstructure and mechanical properties of AISI M42 high-speed steel. Metall Mater Trans 2018;49A:5976–86.
[12] Moon YH, Kim JW, Lee DW. Machining characteristics of electroslag cast steel for hot-working tools. J Mater Process Technol 2004;153–154:654–9.
[13] Peng H, Hu L, Li L, Zhang L, Zhang X. Evolution of the microstructure and mechanical properties of powder metallurgical high-speed steel S390 after heat treatment. J Alloys Compd 2018;740:766–73.
[14] Shen W, Yu L, Liu H. Diffusion welding of powder metallurgy high speed steel by spark plasma sintering. J Mater Process Technol 2020;275:1–9.
[15] Peng H, Hu L, Zhang X, Wei X, Li L, Zhou J. Microstructural evolution, behavior of precipitates, and mechanical properties of powder metallurgical high-speed steel S390 during tempering. Metall Mater Trans 2018;50:874–83.
[16] Liu Y, Ning Y, Yao Z, Fu MW. Hot deformation behavior of the 1.15C-4.00Cr-3.00V-6.00W-5.00Mo powder metallurgy high speed steel. Mater Des 2014;54:854–63.
[17] Mesquita RA, Barbosa CA. High-speed steels produced by conventional casting, spray forming and powder metallurgy. Mater Sci Forum 2005;498–499:244–50.
[18] Chaus AS, Chovanec J, Legerská M. Development of high-speed steels for cast metal-cutting tools. Solid State Phenom 2006;113:559–64.
[19] Ding P, Zhou S, Pan F, Liu J. Ecotechnology for high-speed tool steels. Mater Des 2001;22:137–42.
[20] Fyab C, Lu WA, Zxab C, C JF, Lin ZD. Effect of titanium and rare earth microalloying on microsegregation, eutectic carbides of M2 high speed steel during ESR process. J Rare Earths 2020;38:1030–8.
[21] Li Q, Xia Z, Guo Y, Shen Z, Zheng T, Ding B, et al. Carbides modification and mechanical properties enhancement of Cr12MoV die steel by magnetically controlled electroslag remelting. Metall Mater Trans B 2021;52:1495–507.
[22] Wan S, Li H, Tieu K, Xue Q, Zhu H. Mechanical and tribological assessments of high-vanadium high-speed steel by the conventional powder metallurgy process. Int J Adv Manuf Technol 2019;103:943–55.
[23] Edgar J, Tint S. Additive manufacturing technologies: 3D printing, rapid prototyping, and direct digital manufacturing. Johnson Matthey Technol Rev 2015;vol. 59:193–8. second ed.
[24] Murr LE, Gaytan SM, Ramirez DA, Martinez E, Hernandez J, Amato KN, et al. Metal fabrication by additive manufacturing using laser and electron beam melting technologies. J Mater Sci Technol 2012;28:1–14.
[25] Mesquita RA, Barbosa CA. Spray forming high-speed steel properties and processing. Mater Sci Eng, A 2004;383:87–95.
[26] Kg A, Ar A, Ffa B, Wt A. Microstructure, mechanical, and tribological properties of M3:2 high-speed steel processed by selective laser melting, hot-isostatic pressing, and casting. Addit Manuf 2019;28:585–99.
[27] Rahman NU, Capuano L, Cabeza S, Feinaeugle M. Directed energy deposition and characterization of high-carbon high speed steels. Addit Manuf 2019;30:100838–48.
[28] Saewe J, Gayer C, Jauer L, Kunz J. Feasibility investigation for laser powder bed fusion of high-speed steel. HS 6-5-3-8. In: EuroPM 2018; 2018.

[29] Saewe J, Wilms MB, Jauer L, Schleifenbaum JH. Influence of preheating temperature on hardness and microstructure of high-speed steel HS6-5-3-8 manufactured by laser powder bed fusion. In: Metal additive manufacturing conference; 2019.
[30] Saewe J, Gayer C, Vogelpoth A, Schleifenbaum JH. Feasability investigation for laser powder bed fusion of high-speed steel AISI M50 with base preheating system. BHM Berg-und Hüttenmännische Monatsh 2019;164:101–7.
[31] Saewe J, Carstensen N, Kürnsteiner P, Jgle EA, Schleifenbaum JH. Influence of increased carbon content on the processability of high-speed steel HS6-5-3-8 by laser powder bed fusion. Addit Manuf 2021;46:102125.
[32] Jin J, Gao R, Peng H, Guo H, Chen B. Rapid solidification microstructure and carbide precipitation behavior in electron beam melted high-speed steel. Metall Mater Trans 2020;51:2411–29.
[33] Rahman NU, Capuano L, Rooij M, Matthews D. Laser metal deposition of vanadium-rich high speed steel: microstructural and high temperature wear characterization. Surf Coat Technol 2019;364:115–26.
[34] Arias J, Cabeza M, Castro G, Feijoo I, Merino P, Pena G. Modification of AISI M2 high-speed tool steels after laser-surface melting under different operating conditions. Weld Int 2013;27:1–9.
[35] Arias J, Cabeza M, Castro G, Feijoo I, Merino P, Pena G. Microstructural characterization of laser surface melted AISI M2 tool steel. J Microsc 2010;239:184–93.
[36] Shim DS, Baek GY, Lee EM. Effect of substrate preheating by induction heater on direct energy deposition of AISI M4 powder. Mater Sci Eng, A 2017;682:550–62.
[37] Rahmana NU, Capuanoa L, Meera Avd, Rooijb MBd. Development and characterization of multilayer laser cladded high speed steels. Addit Manuf 2018;24:76–85.
[38] Lee ES, Park WJ, Jung JY, Ahn S. Solidification microstructure and M_2C carbide decomposition in a spray-formed high-speed steel. Metall Mater Trans 1998;29:1395–404.
[39] Lee ES, Park WJ, Baik KH, Ahn S. Different carbide types and their effect on bend properties of a spray-formed high speed steel. Scripta Mater 1998;39:1133–8.
[40] Lu L, Hou LG, Zhang JX, Wang HB, Cui H, Huang JF, et al. Improved the microstructures and properties of M3:2 high-speed steel by spray forming and niobium alloying. Mater Char 2016;117:1–8.
[41] Fayazfar H, Salarian M, Rogalsky A, Sarker D, Russo P, Paserin V, et al. A critical review of powder-based additive manufacturing of ferrous alloys: process parameters, microstructure and mechanical properties. Mater Des 2018;144:98–128.
[42] Bajaj P, Hariharan A, Kini A, Kürnsteiner P, Jägle E. Steels in additive manufacturing: a review of their microstructure and properties. Mater Sci Eng, A 2020;772:138633.
[43] Haghdadi N, Laleh M, Moyle M, Primig S. Additive manufacturing of steels: a review of achievements and challenges. J Mater Sci 2021;56:64–107.
[44] Yin Y, Tan Q, Bermingham M, Mo N, Zhang J. Laser additive manufacturing of steels. Int Mater Rev 2021:1–87.
[45] Gu DD, Meiners W, Wissenbach K, Poprawe R. Laser additive manufacturing of metallic components: materials, processes and mechanisms. Int Mater Rev 2012;57:133–64.
[46] Thompson SM, Bian L, Shamsaei N, Yadollahi A. An overview of direct laser deposition for additive manufacturing; part I: transport phenomena, modeling and diagnostics. Addit Manuf 2015;8:36–62.
[47] Martínez-García A, Monzón M, Paz R. Chapter 12 - standards for additive manufacturing technologies: structure and impact. In: Pou J, Riveiro A, Davim JP, editors. Additive Manufacturing. Elsevier; 2021. p. 395–408.
[48] Oliveira JP, LaLonde AD, Ma J. Processing parameters in laser powder bed fusion metal additive manufacturing. Mater Des 2020;193:108762.
[49] Zhang X, Mao B, Mushongera L, Kundin J, Liao Y. Laser powder bed fusion of titanium aluminides: an investigation on site-specific microstructure evolution mechanism. Mater Des 2021:109501.
[50] Kumar S. Selective laser sintering: a qualitative and objective approach. JOM 2003;55:43–7.
[51] Niu HJ, Chang I. Selective laser sintering of gas and water atomized high speed steel powders. Scripta Mater 1999;41:25–30.
[52] Niu HJ, Chang I. Liquid phase sintering of M3/2 high speed steel by selective laser sintering. Scripta Mater 1998;39:67–72.
[53] Niu HJ, Chang I. Selective laser sintering of gas atomized M2 high speed steel powder. J Mater Sci 2000;35:31–8.
[54] Dewidar MM, Dalgarno KW, Wright CS. Processing conditions and mechanical properties of high speed steel parts fabricated using direct selective laser sintering. Proc IME B J Eng Manufact 2003;217:1651–63.
[55] Maurya NK, Sharma R, Kumar N, Kumar A, Anand P, Rai P, et al. An overview of investigation of Fatigue, tensile strength and hardness of the components fabricated through direct metal laser sintering (DMLS) process. Mater Today Proc 2021;47:3979–84.
[56] Akhtar S, Wright CS, Youseffi M, Hauser C, Childs THC. Selective laser melting of prealloyed high alloy steel powder beds. In: Proceedings of the European powder metallurgy conference, 3; 2003. p. 379–84.
[57] Simchi A, Asgharzadeh H. Densification and microstructural evaluation during laser sintering of M2 high speed steel powder. Mater Sci Technol 2004;20:1462–8.
[58] Asgharz Ad Eh H, Simchi A. Effect of sintering atmosphere and carbon content on the densification and microstructure of laser-sintered M2 high-speed steel powder. Mater Sci Eng, A 2005;403:290–8.
[59] Xu W. Direct additive manufacturing techniques for metal parts: SLM, EBM, laser metal deposition. In: Caballero FG, editor. Encyclopedia of materials: metals and allloys. Oxford: Elsevier; 2022. p. 290–318.
[60] Ivanov Y, Matz W, Rotshtein V, Günzel R, Shevchenko N. Pulsed electron-beam melting of high-speed steel: structural phase transformations and wear resistance. Surf Coat Technol 2002;150:188–98.
[61] Kunz J, Saewe J, Herzog S, Kaletsch A, Schleifenbaum JH, Broeckmann C. Mechanical properties of high-speed steel AISI M50 produced by laser powder bed fusion. Steel Res Int 2020;91:1–9.
[62] Liu ZH, Zhang DQ, Chua CK, Leong KF. Crystal structure analysis of M2 high speed steel parts produced by selective laser melting. Mater Char 2013;84:72–80.
[63] Min Z, Changjun C, Lanlan Q, Kai Y, Guangping C. Laser additive manufacturing of M2 high-speed steel. Mater Sci Technol 2018;34:69–78.
[64] Liu Z, Chua C, Leong K, Kempen K, Kruth J. A preliminary investigation on selective laser melting of M2 high speed steel, innovative developments in virtual and physical prototyping. 2011.
[65] Kempen K, Vrancken B, Buls S, Thijs L, Kruth JP. Selective laser melting of crack-free high density M2 high speed steel parts by baseplate preheating. J Manuf Sci Eng 2014;136:061026.
[66] Niu HJ, Chang I. Instability of scan tracks of selective laser sintering of high speed steel powder. Scripta Mater 1999;41:1229–34.
[67] Rodrigues TA, Escobar JD, Shen J, Duarte VR, Ribamar GG, Avila JA, et al. Effect of heat treatments on 316 stainless

steel parts fabricated by wire and arc additive manufacturing : microstructure and synchrotron X-ray diffraction analysis. Addit Manuf 2021;48:102428.
[68] Rodrigues TA, Bairrão N, Farias FWC, Shamsolhodaei A, Shen J, Zhou N, et al. Steel-copper functionally graded material produced by twin-wire and arc additive manufacturing (T-WAAM). Mater Des 2022;213:110270.
[69] Ocelík V, Eekma M, Hemmati I, De Hosson JTM. Elimination of start/stop defects in laser cladding. Surf Coat Technol 2012;206:2403–9.
[70] Wirth F, Wegener K. A physical modeling and predictive simulation of the laser cladding process. Addit Manuf 2018;22:307–19.
[71] Herzog D, Seyda V, Wycisk E, Emmelmann C. Additive manufacturing of metals. Acta Mater 2016;117:371–92.
[72] Lopes JG, Machado CM, Duarte VR, Rodrigues TA, Santos TG, Oliveira JP. Effect of milling parameters on HSLA steel parts produced by Wire and Arc Additive Manufacturing (WAAM). J Manuf Process 2020;59:739–49.
[73] Shamsaei N, Yadollahi A, Bian L, Thompson SM. An overview of direct laser deposition for additive manufacturing; part II: mechanical behavior, process parameter optimization and control. Addit Manuf 2015;8:12–35.
[74] Aja B, Gang WA, Zhao J, Hy A, Sy C, Yu ZC, et al. Multi-scale modelling of solidification and microstructure evolution in laser-deposition of T15 high speed steel. J Manuf Process 2020;50:24–33.
[75] Yang Y, Jiang S, Xiang Z. Microstructure evolution of laser direct metal deposition of M2 high speed steel. Mater Sci Forum 2017;879:2198–203.
[76] Niu HJ, Chang I. Microstructural evolution during laser cladding of M2 high-speed steel. Metall Mater Trans 2000;31:2615–25.
[77] Xiao H, Chen C, Zhang M. Microstructure and mechanical properties of H13 steel/high-speed steel composites prepared by laser metal deposition. J Mater Eng Perform 2019;29:66–77.
[78] Nur A, Mbdr B, Dtam C, Gw D, Ms E, Grber A. Wear characterization of multilayer laser cladded high speed steels. Tribol Int 2019;130:52–62.
[79] Kattire P, Paul S, Singh R, Yan W. Experimental characterization of laser cladding of CPM 9V on H13 tool steel for die repair applications. J Manuf Process 2015;20:492–9.
[80] Ye EJ, Lee JY, Lee EK, Shim DS. Microstructures and mechanical properties of deposited Fe-8Cr-3V-2Mo-2W on SCM420 substrate using directed energy deposition and effect of post- heat treatment. Materials 2021;14:1231.
[81] Hashemi N, Mertens A, Montrieux HM, Tchuindjang JT, Lecomte-Beckers J. Oxidative wear behaviour of laser clad high speed steel thick deposits: influence of sliding speed, carbide type and morphology. Surf Coat Technol 2017;315:519–29.
[82] Shim DS, Baek GY, Lee SB, Yu JH, Park SH. Influence of heat treatment on wear behavior and impact toughness of AISI M4 coated by laser melting deposition. Surf Coat Technol 2017;328:219–30.
[83] Leunda J, Soriano C, Sanz C, Navas VG. Laser cladding of vanadium-carbide tool steels for die repair. Phys Procedia 2011;12:345–52.
[84] Wang SH, Chen JY, Xue L. A study of the abrasive wear behaviour of laser-clad tool steel coatings. Surf Coat Technol 2006;200:3446–58.
[85] Hu YP, Chen CW, Mukherjee K. Development of a new laser cladding process for manufacturing cutting and stamping dies. J Mater Sci 1998;33:1287–92.
[86] Navas C, Conde A, Fernández B, Zubiri F, Damborenea JD. Laser coatings to improve wear resistance of mould steel. Surf Coat Technol 2005;194:136–42.
[87] Park JS, Lee MG, Cho YJ, Sung JH, Jeong MS, Lee SK, et al. Effect of heat treatment on the characteristics of tool steel deposited by the directed energy deposition process. Met Mater Int 2016;22:143–7.
[88] Arias J, Cabeza M, Castro G, Feijoo I, Merino P, Pena G. Microstructure and mechanical behavior of laser surface melted AISI M2 high-speed steel. Surf Interface Anal 2010;42:752–6.
[89] Singer REA. Spray rolling of metals. Prod Eng 1972;51:98.
[90] Yu YP, Huang JF, Cui H, Cai YH, Zhang JS. Microstructures and thermostability of spray formed Nb-containing high speed steel. Adv Mater Res 2012;418–420:3–7.
[91] Bewlay BP, Cantor B. Modeling of spray deposition: measurements of particle size, gas velocity, particle velocity, and spray temperature in gas-atomized sprays. Metall Mater Trans B 1990;21:899–912.
[92] Sheng X, Mackie C, Iii CAH. Heat transfer characterization of the solidification process resulting from a spray forming process. Int Commun Heat Mass 2005;32:872–83.
[93] Cui C, Schulz A, Schimanski K, Zoch HW. Spray forming of hypereutectic Al-Si alloys. J Mater Process Technol 2009;209:5220–8.
[94] Mao J, Chang KM, Yang W, Furrer DU, Ray K, Vaze SP. Cooling precipitation and strengthening study in powder metallurgy superalloy Rene88DT. Mater Sci Eng, A 2002;332:318–29.
[95] Kjeldsteen Peter. Development of high alloyed tool steels using spray forming on an industrial scale. Powder Metall 2003;46:297–8.
[96] Spiegelhauer C. Industrial production of tool steels using the spray forming technology. In: Proceedings of the 6 th international tooling conference; 2002. p. 1101–9.
[97] Ogata K, Lavernia E, Rai G, Grant NJ. Structure and properties of a rapidly solidified superalloy produced by liquid dynamic compaction. Int J Rapid Solidif 1986;2:21–35.
[98] Grant P. Spray forming. Prog Mater Sci 1995;39:497–545.
[99] Grant PS. Solidification in spray forming. Metall Mater Trans 2007;38:1520–9.
[100] Grant PS, Cantor B, Katgerman L. Modelling of droplet dynamic and thermal histories during spray forming-I. individual droplet behaviour. Acta Mater 1993;41:3097–108.
[101] Grant PS, Cantor B. Modelling of droplet dynamic and thermal histories during spray forming-III. analysis of spray solid fraction. Acta Mater 1995;43:913–21.
[102] Wang H, Hou L, Li Y, Ou P, Shen L, Wen X, et al. Effect of niobium on the secondary precipitates and tempering resistance of spray-formed M3:2 high-speed steel. J Mater Eng Perform 2019;28:1–12.
[103] Zhao SL, Fan JF, Zhang JY, Chou KC, Le HR. High speed steel produced by spray forming. Adv Manuf 2016;4:115–22.
[104] Zhang G, Yuan H, Jiao D, Li Z, Zhang Y, Liu Z. Microstructure evolution and mechanical properties of T15 high speed steel prepared by twin-atomiser spray forming and thermo-mechanical processing. Mater Sci Eng, A 2012;558:566–71.
[105] Wang HB, Hou LG, Zhang JX. Microstructures and high temperature properties of spray formed niobium-containing M3 high speed steel. Mater Werkst 2014;45:689–98.
[106] Schulz A, Uhlenwinkel V, Bertrand C, Kohlmann R, Kulmburg A, Oldewurtel A, et al. Nitrogen pick-up during spray forming of high-alloyed steels and its influence on microstructure and properties of the final products. Mater Sci Eng, A 2004;383:58–68.

[107] Sidorchuk OM. Structure and properties of low-alloy high-speed spray-formed steel. Poeder Metall Met C 2012;50:704–7.
[108] Wang H, Hou L, Zhang J, Lu L, Cui H. The secondary precipitates of niobium-alloyed M3:2 high speed steel prepared by spray deposition. Mater Char 2015;106:245–54.
[109] Chengsong Cui, Alwin Schulz, Volker Uhlenwinkel. Co-spray forming of gradient deposits from two sprays of different tool steels using scanning gas atomizers. Steel Res Int 2013;84:1075–84.
[110] Cui C, Schulz A. Modeling and simulation of spray forming of clad deposits with graded interface using two scanning gas atomizers. Metall Mater Trans B 2013;44:1030–40.
[111] Mumtaz KA, Hopkinson N. Selective laser melting of thin wall parts using pulse shaping. J Mater Process Technol 2010;210:279–87.
[112] Zhu HH, Lu L, Fuh J. Development and characterisation of direct laser sintering Cu-based metal powder. J Mater Process Technol 2003;140:314–7.
[113] Mazumder J, Dutta D, Kikuchi N, Ghosh A. Closed loop direct metal deposition: art to part. Opt Laser Eng 2000;34:397–414.
[114] Huang YL, Jian L, Ma NH, Li JG. Three-dimensional analytical model on laser-powder interaction during laser cladding. J Laser Appl 2006;18:42–6.
[115] Peyre P, Aubry P, Fabbro R, Neveu R, Longuet A. Analytical and numerical modelling of the direct metal deposition laser process. J Phys D Appl Phys 2008;41:025403.
[116] He X, Mazumder J. Transport phenomena during direct metal deposition. J Appl Phys 2007;101:053113.
[117] Xie J, Kar A, Rothenflue JA, Latham WP. Temperature-dependent absorptivity and cutting capability of CO2, Nd:YAG and chemical oxygen-iodine lasers. J Laser Appl 1997;9:77–85.
[118] Meiners W. Direktes selektives Laser-Sintern einkomponentiger metallischer Werkstoffe. 1999. p. 125. Dissertation.
[119] Rombouts M, Kruth JP, Froyen L, Mercelis P. Fundamentals of selective laser melting of alloyed steel powders. CIRP Annals 2006;55:187–92.
[120] Debroy T, Wei HL, Zuback J, Mukherjee T, Zhang W. Additive manufacturing of metallic components-process, structure and properties. Prog Mater Sci 2018;92:112–224.
[121] Manvatkar V, De A, Debroy T. Heat transfer and material flow during laser assisted multi-layer additive manufacturing. J Appl Phys 2014;116:133–40.
[122] Vásquez F, Ramos-Grez JA, Walczak M. Multiphysics simulation of laser-material interaction during laser powder depositon. Int J Adv Manuf Technol 2012;59:1037–45.
[123] Yin H, Felicelli SD. Dendrite growth simulation during solidification in the LENS process. Acta Mater 2010;58:1455–65.
[124] Ye R, Smugeresky JE, Zheng B, Zhou Y, Lavernia EJ. Numerical modeling of the thermal behavior during the LENS® process. Mater Sci Eng, A 2006;428:47–53.
[125] Gäumann M, Bezençon C, Canalis P, Kurz W. Single-crystal laser deposition of superalloys: processing-microstructure maps. Acta Mater 2001;49:1051–62.
[126] Han L, Liou FW, Musti S. Thermal behavior and geometry model of melt pool in laser material process. J Heat Tran 2005;127:1005–14.
[127] Yu F, Wei Y, Ji Y, Chen L-Q. Phase field modeling of solidification microstructure evolution during welding. J Mater Process Technol 2018;255:285–93.
[128] Liu D, Wang Y. Mesoscale multi-physics simulation of rapid solidification of Ti-6Al-4V alloy. Addit Manuf 2019;25:551–62.
[129] Smith JE, Jordan ML. Mathematical and graphical interpretation of the log-normal law for particle size distribution analysis. J Colloid Sci 1964;19:549–59.
[130] Lefebvre AH. Fifty years of gas turbine fuel injection. Atomization Sprays 2000;10:251–76.
[131] Clare H. An airblast atomizer for use with viscous fuels. J Inst Fuel 1954;27:510–5.
[132] Lawley A. Atomization: the production of metal powders. Metal Powder Indus Fed 1992;159:1–5.
[133] Mathur P, Annavarapu S, Apelian D, Lawley A. Spray casting: an integral model for process understanding and control. Mater Sci Eng, A 1991;142:261–76.
[134] Wigg LD. Drop-size prediction for twin-fluid atomizers. J Inst Fuel 1964;27:125.
[135] Lubanska H. Correlation of spray ring data for gas atomization of liquid metals. JOM 1970;22:45–9.
[136] Cai W, Lavernia EJ. Modeling of porosity during spray forming: Part I. effects of processing parameters. Metall Mater Trans B 1998;29:1085–96.
[137] Rai G, Lavernia E, Grant NJ. Powder size and distribution in ultrasonic gas atomization. JOM 1985;37:22–6.
[138] Titus P, Damian T. Introduction to fluid mechanics. fourth ed. 1992. Book.
[139] Ünal A. Effect of processing variables on particle size in gas atomization of rapidly solidified aluminium powders. Mater Sci Technol 2014;3:1029–39.
[140] Mathur P, Apelian D, Lawley A. Analysis of the spray deposition process. Acta Mater 1989;37:429–43.
[141] Ünal A. Flow separation and liquid rundown in a gas-atomization process. Metall Mater Trans B 1989;20:613–22.
[142] Ünal A. Influence of gas flow on performance of "Confined" atomization nozzles. Metall Mater Trans B 1989;20:833–43.
[143] Pi Z, Lu X, Wu Y, Wang L, Jia C, Qu X, et al. Simulation of jet-flow solid fraction during spray forming. Int J Miner Metall Mater 2017;24:657–69.
[144] Trapaga G, Szekely J. Mathematical modeling of the isothermal impingement of liquid droplets in spraying processes. Metall Mater Trans B 1991;22:901–14.
[145] Liang X, Earthman JC, Lavernia EJ. On the mechanism of grain formation during spray atomization and deposition. Acta Mater 1992;40:3003–16.
[146] Bewlay BP, Cantor B. The relationship between thermal history and microstructure in spray-deposited tin-lead alloys. J Mater Res 1991;6:1433–54.
[147] Grant PS, Maher PP, Cantor B. Heat flow in spray-formed Al-4Cu. Mater Sci Eng, A 1994;179–180:72–6.
[148] Gutierrez-Miravete EJ Lavernia, Trapaga GM, Szekely J, Grant NJ. A mathematical model of the spray deposition process. Metall Mater Trans 1989;20:71–85.
[149] Turnbull D. Erratum: kinetics of solidification of supercooled liquid mercury droplets. J Chem Phys 1952;20:1824. 1824.
[150] Miyazawa Y, Pound GM. Homogeneous nucleation of crystalline gallium from liquid gallium. J Cryst Growth 1974;23:45–57.
[151] Hirth JP. Nucleation, undercooling and homogeneous structures in rapidly solidified powders. Metall Mater Trans 1978;9:401–4.
[152] Lawrynowicz DE, Li B, Lavernia EJ. Particle penetration during spray forming and co-injection of Ni_3Al+B/Al_2O_3 intermetallic matrix composite. Metall Mater Trans B 1997;28:877–97.
[153] Bolling GF, Cissé J. A theory for the interaction of particles with a solidifying front. J Cryst Growth 1971;10:56–66.
[154] Stefanescu DM, Dhindaw BK, Kacar SA, Moitra A. Behavior of ceramic particles at the solid-liquid metal interface in metal matrix composites. Metall Mater Trans 1988;19:2847–55.

[155] Chernov AA. Growth kinetics and capture of impurities during gas phase crystallization. J Cryst Growth 1977;42:55–76.
[156] Wang Y, Chu S, Mao B, Xing H, Zhang J, Sun B. Microstructure, residual stress, and mechanical property evolution of a spray-formed vanadium-modified high-speed steel processed by post-heat treatment. J Mater Res Technol 2022.
[157] Boccalini M, Goldenstein H. Solidification of high speed steels. Int Mater Rev 2001;46:92–115.
[158] Dae Jin, Ha Hyo, Kyung Sung, Joon Wook, Park Sunghak. Effects of alloying elements on microstructure, hardness, wear resistance, and surface roughness of centrifugally cast high-speed steel rolls. Metall Mater Trans 2009;40A:2568–77.
[159] Ren X, Fu H, Xing J. Formation of eutectic borocarbides in high boron high speed steel during non-equilibrium crystallization. Steel Res Int 2018;90:1800284–91.
[160] Wu HQ, Sasaguri N, Matsubara Y, Hashimoto M. Solidification of multi-alloyed white cast iron: type and morphology of carbides. AFS Trans 1996;104:103–8.
[161] Hwang KC, Lee S, Lee HC. Effects of alloying elements on microstructure and fracture properties of cast high speed steel rolls Part II. fracture behavior. Mater Sci Eng, A 1998;254:282–95.
[162] Chaus AS, Dománková M. Unknown high-speed steel. Mater Lett 2021;292:129653.
[163] Chaus AS, Sahul M. On origin of delta eutectoid carbide in M2 high-speed steel and its behaviour at high temperature. Mater Lett 2019;256:126605.
[164] Fredriksson H, Stjerndahl J. Solidification of iron-base alloys. Met Sci 1982;16:575–86.
[165] Jones TK, Mukherjee T. Identification of carbides in as-cast 18-4-1 high-speed steels. J Iron Steel Inst 1970:208.
[166] Chaus AS, Braèík M, Sahul M, Tittel V. High-temperature transformation of carbides in skeleton eutectic and delta-eutectoid of cast high-speed steel. Met Sci Heat Treat 2020;62:489–97.
[167] Park G-W, Shin S, Kim J-Y, Koo Y-M, Lee W, Lee K-A, et al. Analysis of solidification microstructure and cracking mechanism of a matrix high-speed steel deposited using directed-energy deposition. J Alloys Compd 2022;907:164523.
[168] Chaus AS. Structural and phase changes in carbides of the high-speed steel upon heat treatment. Phys Met Metallogr 2016;117:684–92.
[169] Chaus AS, Beznák M, Boha?Ík M, Porubsky J, úradník P. Effect of austenitising temperature on structural changes in modified high-speed steel of AISI M2 type. Trans Tech Publications; 2012. p. 348–53.
[170] Fredriksson H, Brising S. Formation of carbides during solidification of high-speed steels. Scand J Metall 1976;5:268–75.
[171] Taran YN, Nizhnikovskaya PF, Snagovskii LM, Vukelich SB, Nesterenko AM. Eutectic in tungsten-molybdenum high-speed steel. Met Sci Heat Treat 1979;21:791–5.
[172] Gongqi S, Peidao D, Shouze Z. Effect of vanadium on cast carbide in high speed steels. Mater Sci Technol 1992;8:449–54.
[173] El-Rakayby AM, Mills B. On the microstructure and mechanical properties of high-speed steels. J Mater Sci 1988;23:4340–4.
[174] Barkalow RH, Kraft RW, Goldstein JI. Solidification of M2 high speed steel. Metall Mater Trans B 1972;3:919–26.
[175] Ghomashchi MR. Quantitative microstructural analysis of M2 grade high speed steel during high temperature treatment. Acta Mater 1998;46:5207–20.
[176] Zhou XF, Fang F, Jiang JQ, Zhu WL, Xu HX. Study on decomposition behaviour of M_2C eutectic carbide in high speed steel. Mater Sci Technol 2013;28:1499–504.
[177] Zhu Q, Zhu HT, Tieu AK, Reid M, Zhang LC. In-situ investigation of oxidation behaviour in high-speed steel roll material under dry and humid atmospheres. Corrosion Sci 2010;52:2707–15.
[178] Gulyaev AP, Kupalova IK. Effect of cobalt on the structure and properties of high-speed steels. Met Sci Heat Treat 1970;12:666–71.
[179] Mu S. Microstructure and properties of spray-formed S390 high-speed steel. In: The 6th international seminar on modern cutting and measuring engineering; 2014. p. 32–4.
[180] Xu Y, Ge CC. Study on CPM9V high speed steel ring prepared by spray forming. Adv Mater Res 2011;311–313:624–30.
[181] Liu ZH, Chua CK, Leong KF, Thijs L, Kruth JP. Microstructural investigation of M2 high speed steel produced by selective laser melting: microstructural investigation of M2 high speed steel. In: Photonics & optoelectronics; 2012.
[182] Wang H, Hong D, Hou L, Ou P, Zhao H. Influence of tempering temperatures on the microstructure, secondary carbides and mechanical properties of spray-deposited AISI M3:2 high-speed steel. Mater Chem Phys 2020;255:1–11.
[183] Cui C, Fritsching U, Schulz A, Chun Q. Mathematical modeling of spray forming process of tubular preforms: Part 1. shape evolution. Acta Mater 2005;53:2765–74.
[184] Lavernia EJ, Wu Y. Spray atomization and deposition. 1996. p. 232–3. Chichester.
[185] Wang L, Felicelli S. Process modeling in laser deposition of multilayer SS410 steel. J Manuf Sci Eng 2007;129:1028–34.
[186] Cui C, Fritsching U, Schulz A, Li Q. Mathematical modeling of spray forming process of tubular preforms: Part 2. Heat transfer. Acta Mater 2005;53:2775–84.
[187] Cai W, Lavernia EJ. Modeling of porosity during spray forming: Part II. effects of atomization gas chemistry and alloy compositions. Metall Mater Trans B 1998;29:1097–106.
[188] Liu Y, Yang Y, Mai S, Wang D, Song C. Investigation into spatter behavior during selective laser melting of AISI 316L stainless steel powder. Mater Des 2015;87:797–806.
[189] Zhang B, Dembinski L, Coddet C. The study of the laser parameters and environment variables effect on mechanical properties of high compact parts elaborated by selective laser melting 316L powder. Mater Sci Eng, A 2013;584:21–31.
[190] Song B, Zhao X, Li S, Han C, Wei Q, Wen S, et al. Differences in microstructure and properties between selective laser melting and traditional manufacturing for fabrication of metal parts: a review. Front Mech Eng 2015;10:111–25.
[191] Hjortsberg E, Bergquist B. Filling induced density variations in metal powder. Powder Metall 2002;45:146–53.
[192] Jeong Ye, Shin GY, Shim DS. Effect of P21 buffer layer on interfacial bonding characteristics of high-carbon tool steel hardfaced through directed energy deposition. J Manuf Process 2021;68:1596–614.
[193] Khodabakhshi F, Farshidianfar MH, Bakhshivash S, Gerlich AP, Khajepour A. Dissimilar metals deposition by directed energy based on powder-fed laser additive manufacturing. J Manuf Process 2019;43:83–97.
[194] Zeng OH. Evolution of the residual stress state in a duplex stainless steel during loading. Acta Mater 1999;47:2669–84.
[195] s CGadA, Caballero FG, Capdevila C, Álvarez LF. Application of dilatometric analysis to the study of solid-solid phase transformations in steels. Mater Char 2002;48:101–11.
[196] Huang Q, Volkova O, Biermann H, Mola J. Dilatometry analysis of dissolution of Cr-rich carbides in martensitic stainless steels. Metall Mater Trans 2017;48:5771–7.

[197] Withers JP. Fracture mechanics by three-dimensional crack-tip synchrotron X-ray microscopy. Philos Trans R Soc A 2015:373.
[198] Holzweissig MJ, Taube A, Brenne F, Schaper M, Niendorf T. Microstructural characterization and mechanical performance of hot work tool steel processed by selective laser melting. Metall Mater Trans B 2015;46:545–9.
[199] Sames WJ, List FA, Pannala S, Dehoff RR, Babu SS. The metallurgy and processing science of metal additive manufacturing. Int Mater Rev 2016;61:1–46.
[200] Kahnert M, Lutzmann S, Zaeh MF. Layer formations in electron beam sintering. In: Solid freeform fabrication symposium; 2007.
[201] Mao B, Siddaiah A, Liao Y, Menezes PL. Laser surface texturing and related techniques for enhancing tribological performance of engineering materials: a review. J Manuf Process 2020;53:153–73.
[202] Rangaswamy P, Griffith ML, Prime MB, Holden TM, Rogge RB, Edwards JM, et al. Residual stresses in LENS® components using neutron diffraction and contour method. Mater Sci Eng, A 2005;399:72–83.
[203] Zhang X, Mao B, Liao Y, Zheng Y. Selective laser melting of graphene oxide–reinforced Ti–48Al–2Cr–2Nb: improved manufacturability and mechanical strength. J Mater Res 2020:1–8.
[204] Selcuk C. Laser metal deposition for powder metallurgy parts. Powder Metall 2011;54:94–9.
[205] Zhang S, Lin X, Chen J, Huang W. Influence of heat treatment on residual stress of Ti-6Al-4V alloy by laser solid forming. Rare Met Mater Eng 2009;38:774–8.
[206] Telasang G, Dutta Majumdar J, Padmanabham G, Tak M, Manna I. Effect of laser parameters on microstructure and hardness of laser clad and tempered AISI H13 tool steel. Surf Coat Technol 2014;258:1108–18.
[207] Mcgrann RTR, Greving DJ, Shadley JR, Rybicki EF, Kruecke TL, Bodger BE. The effect of coating residual stress on the fatigue life of thermal spray-coated steel and aluminum. Surf Coat Technol 1998;108–109:59–64.
[208] Lee TL, Mi J, Zhao SL, Fan JF, Zhang SY, Kabra S, et al. Characterization of the residual stresses in spray-formed steels using neutron diffraction. Scripta Mater 2015;100:82–5.
[209] Lee TL, Mi J, Ren S, Zhao S, Fan J, Kabra S, et al. Modelling and neutron diffraction characterization of the interfacial bonding of spray formed dissimilar steels. Acta Mater 2018;155:318–30.
[210] Kim CK, Kim YC, Park JI, Lee S, Kim NJ, Yang JS. Effects of alloying elements on microstructure, hardness, and fracture toughness of centrifugally cast high-speed steel rolls. Metall Mater Trans 2005;36A:87–97.
[211] Igharo M, Wood JV. Investigation of M2 high speed steel produced by osprey process. Powder Metall 1989;32:124–31.
[212] Ernst IC, Duh D. ESP4 and TSP4, a comparison of spray formed with powder metallurgically produced cobalt free high-speed steel of type 6W-5Mo-4V-4Cr. J Mater Sci 2004;39:6831–4.
[213] Rickinson BA, Kirk FA, Davies DRG. CSD: a novel process for particle metallurgy products. Powder Metall 1981;24:1–6.
[214] Wei S, Zhu J, Xu L. Research on wear resistance of high speed steel with high vanadium content. Mater Sci Eng, A 2005;404:138–45.
[215] Xu L, Xing J, Wei S, Zhang Y, Long R. Study on relative wear resistance and wear stability of high-speed steel with high vanadium content. Wear 2007;262:253–61.
[216] Xu LJ, Wei SZ, Ji YP, Zhang GS, Li JW, Long R. Effect of carbon on frictional wear behaviours of high vanadium high speed steel under dry sliding condition. Mater Sci Forum 2010;654–656:370–3.
[217] Xu L, Xing J, Wei S, Zhang Y, Long R. Artificial neural network prediction of retained austenite content and impact toughness of high-vanadium high-speed steel (HVHSS). Mater Sci Eng, A 2006;433:251–6.
[218] Xu L, Xing J, Wei S, Tao P, Zhang Y, Rui L. Artificial neural network prediction of heat-treatment hardness and abrasive wear resistance of high-vanadium high-speed steel (HVHSS). J Mater Sci 2007;42:2565–73.
[219] Tekumalla S, Tosi R, Tan X, Seita M. Directed energy deposition and characterization of high-speed steels with high vanadium content. Addit Manuf Lett 2022;2:100029.
[220] Telasang G, Dutta Majumdar J, Padmanabham G, Manna I. Structure-property correlation in laser surface treated AISI H13 tool steel for improved mechanical properties. Mater Sci Eng, A 2014;599:255–67.
[221] Ma C, Zhao S, Fan J, Li J. Effect of heat treatment on microstructure and hardness of spray-formed M42 high speed steel. Thermal Process Technol 2012;41:156–8.
[222] Zhang Y, Zhang G, Li Z. Analysisof twin-nozzle-scanning spray forming process and spray formed high speed steel (HSS). J Iron Steel Res Int 2007;14:7–10.
[223] Baek GY, Shin GY, Lee KY, Shim DS. Effect of post-heat treatment on the AISI M4 layer deposited by directed energy deposition. Metals 2020;10:703.
[224] Baek GY, Shin GY, Lee KY, Shim DS. Mechanical properties of tool steels with high wear resistance via directed energy deposition. Metals 2019;9:282.
[225] Zhang Y, Zhang G, Li Z, Yuan H. Research on the internal microstructure of spray formed high speed steel. J Aeronautical Mater 2010;30:19–24.
[226] Ren X, Fu H, Xing J, Yi Y. Research on high-temperature dry sliding friction wear behavior of CaTi modified high boron high speed steel. Tribol Int 2019;132:165–76.
[227] Bataille C, Luc E, Bigerelle M, Deltombe R, Dubar M. Rolls wear characterization in hot rolling process. Tribol Int 2016;100:328–37.
[228] Günen A, Kanca E, Karakaş MS, Koç V, Gök MS, Kanca Y, et al. High temperature wear behavior of the surface-modified externally cooled rolls. Surf Coat Technol 2018;348:130–41.
[229] Zhu Q, Zhu HT, Tieu AK, Kong C. Three dimensional microstructure study of oxide scale formed on a high-speed steel by means of SEM, FIB and TEM. Corrosion Sci 2011;53:3603–11.
[230] Lu W, Zhai W, Wang J, Liu X, Zhou L, Ibrahim AMM, et al. Additive manufacturing of isotropic-grained, high-strength and high-ductility copper alloys. Addit Manuf 2021;38:101751.
[231] Song R, Hanaki S, Yamashita M, Uchida H. Reliability evaluation of a laser repaired die-casting die. Mater Sci Eng, A 2008;483–484:343–5.
[232] Hardell J, Hernandez S, Mozgovoy S, Pelcastre L, Courbon C, Prakash B. Effect of oxide layers and near surface transformations on friction and wear during tool steel and boron steel interaction at high temperatures. Wear 2015;330–331:223–9.
[233] Joos O, Boher C, Vergne C, Gaspard C, Nylen T, Rezaï-Aria F. Assessment of oxide scales influence on wear damage of HSM work rolls. Wear 2007;263:198–206.
[234] Nilsson M, Olsson M. An investigation of worn work roll materials used in the finishing stands of the hot strip mill for steel rolling. Proc IME J J Eng Tribol 2013;227:837–44.
[235] Hanlon DN, Rainforth WM. The rolling sliding wear response of conventionally processed and spray formed high speed steel at ambient and elevated temperature. Wear 2003;255:956–66.
[236] Sfg A, Eaf A, Syta B. The effect of counterbody on tribological adaptation of an electron beam deposited HSS

M2 steel coating in a range of sliding speeds and normal loads. Tribol Int 2021;161:107109.
[237] Hanlon DN, Rainforth WM, Sellars CM. The rolling/sliding wear response of conventionally processed and spray formed high chromium content cast iron at ambient and elevated temperature. Wear 1999;225–229:587–99.
[238] Ikawa Y, Itami T, Kumagai K, Ando T. Spray deposition method and its application to production of mill rolls. Tetsu-To-Hagane 2009;75:766–73.
[239] Rodenburg C, Rainforth MW. A quantitative analysis of the influence of carbides size distributions on wear behaviour of high-speed steel in dry rolling/sliding contact. Acta Mater 2007;55:2443–54.
[240] Seifi M, Salem A, Beuth J, Harrysson O, Lewandowski JJ. Overview of materials qualification needs for metal additive manufacturing. JOM 2016;68:747–64.

Yujie Wang received his B.S. degree in Materials Forming and Control Engineering from Qingdao University, China, in 2016 and his M.S. degree in Materials Science and Engineering from Xiangtan University, China, in 2019. Currently, he is pursuing his PhD in Advanced Manufacturing at Shanghai Jiao Tong University, China. His research interests mainly include additive manufacturing of high-speed steel and low-alloy steels.

Professor **Bo Mao** is currently an Associate Professor in the School of Materials Science and Engineering at Shanghai Jiao Tong University. He joined the University in March 2021. He received his B.S. from the Huazhong University of Science and Technology in 2011, M.E. from Shanghai Jiao Tong University in 2014, and his Ph.D. in Mechanical Engineering at the University of Nevada-Reno in United States in 2020. His research area is advanced materials processing and manufacturing. His research specifically focuses on the laser processing, additive manufacturing, and the processing-microstructure-properties relationship. He has authored or co-authored over 30 publications in the scientific journals and served as the editor or reviewer for more than 10 scientific journals. He used to give 13 technical presentations in high-level international conferences, including MS&T 2018, AeroMat2019, and MSEC 2019. He has been awarded the differential fee fellowship in UNR and MSEC2019 student travel award sponsored by the US National Science Foundation. He was among the winners of the 2020 Exceptional Overseas Chinese Student Scholarship. He is the member of American Society of Mechanical Engineers (ASME) and honorable member of Institue of Roller Design (IRD) of the United States.

Professor Shuangjie Chu is currently an engineering scientist at China Baowu and executive director of the China Society for Materials Research. He has rich experience in steel manufacturing and technical management. He has long been engaged in the development and industrialization of new steel products. He was awarded the first and second prizes of China National Science and Technology Progress.

Sai Chen received her master's degree in iron and steel metallurgy from the University of Science and Technology Beijing, China, in 2021. She is currently pursuing her PhD in advanced manufacturing at Shanghai Jiao Tong University, China. Her research interests include additive manufacturing of high-speed steel and iron matrix composites.

Associate Professor Hui Xing received her PhD from Shanghai Jiao Tong University in 2009. Her main research interests are the micromechanics of high-performance steel material toughness and the development of multi-scale high throughput characterization methods. Currently, she has published dozens of high-level papers as first author and corresponding author.

Dr. Haiyan Zhao is a senior manager of Baowu Special Metallurgy Cooperation Co. He has long been engaged in the development and characterization of high-performance special steels.

Dr. Shuyang Wang is a senior expert of Baoshan Iron & Steel Cooperation Co. He has been engaged in the development and rolling research of high-performance special steels for a long time.

Dr. Yuqian Wang received her Ph.D degree from the department of Mechanical Engineering of University of Nevada-Reno and used to serve as an instructor in UNR. She is now working in Apple and her research focus is the mechanical behavior of metallic materials.

Prof. Jiao Zhang insists on combining theoretical and experimental research, and is now mainly engaged in additive manufacturing of high-performance aluminum alloys and steel materials. He has been in charge of more than ten major instrumentation projects of the National Natural Science Foundation of China (NSFC) and the National Natural Science Foundation of China (NSFC), and has granted more than sixty patents.

Prof. Baode Sun is currently engaged in the development of preparation methods for high performance metals, and has presided over more than 50 projects such as 973 projects, 863 projects, major special material projects for large aircraft, supporting projects, key projects of National Natural Foundation of China, and large scientific instrument projects. He has published more than 200 SCI papers and has been awarded more than 100 national invention patents and one international invention patent. His current research activities include the development of additive manufacturing (3D printing), casting molding technology, materials science and engineering.